International Journal of Heat and Mass Transfer 254 (2026) 127602

Contents lists available at ScienceDirect

International Journal of Heat and Mass Transfer

journal homepage: www.elsevier.com/locate/ijhmt

Experimental investigation and analysis of flow condensation heat transfer in microgravity–Experiments onboard the International Space Station

Issam Mudawar [a,1,*], Steven J. Darges [a], Mohammad M. Hasan [b], Henry K. Nahra [b], R. Balasubramaniam [c], Jeffrey R. Mackey [d]

[a] Purdue University Boiling and Two-Phase Flow Laboratory (PU-BTPFL), School of Mechanical Engineering, Purdue University, 585 Purdue Mall, West Lafayette, IN 47907, USA

[b] NASA Glenn Research Center, 21000 Brookpark Road, Cleveland, OH 44135, USA

[c] Case Western Reserve University, 10900 Euclid Ave., Cleveland, OH 44106, USA

[d] HX5, LLC, 3000 Aerospace Parkway, Brookpark, OH 44142, USA

A R T I C L E I N F O

Keywords:
Microgravity
Condensation
Annular flow
Heat transfer coefficient
Saturated inlet
Superheated inlet
International Space Station

A B S T R A C T

This study presents the flow condensation heat transfer results of the Flow Boiling and Condensation Experiment (FBCE). The primary goal of FBCE is to obtain fundamental flow boiling and condensation heat transfer data in microgravity (μg_e) through experiments onboard the International Space Station. Experiments were performed with the Condensation Module for Heat Transfer (CM-HT), which is a tube-in-tube counterflow heat exchanger. Condensing nPFH flows through a stainless steel tube with an inner diameter of 7.24 mm and rejects heat to cooling water flowing in an annular channel (with inner and outer gap diameter of 7.94 and 12.70 mm, respectively) surrounding the tube. Experiments tested a broad range of nPFH mass velocities, $G = 72.8 – 291.5$ kg/m^{2}s, inlet thermodynamic equilibrium qualities, $x_{e,in} = 0.28 – 1.19$, inlet pressures, $p_{in} = 103.9 – 160.2$ kPa, and water mass velocities, $G_w = 129.4 – 324.7$ kg/m^{2}s. A parametric investigation shows local condensation heat transfer coefficient, h, is primarily dependent on G and local x_e, which can be represented by the two-phase mixture Reynolds number, Re_{tp}. Channel averaged heat transfer coefficient in the saturated two-phase region, $\overline{h}_{tp}$, increases with increasing G and $x_{e,in}$. However, increasing inlet superheat does not affect $\overline{h}_{tp}$, but does increase the heat transfer coefficient averaged over the entire channel, $\overline{h}$. In the present experiments, G is sufficient to mitigate the effects of gravity, and $\overline{h}_{tp}$ in μg_e aligns with those for vertical down flow and horizontal flow in Earth gravity. Various correlations for h_{tp} were assessed, and the best performing correlation with a Mean Absolute Error (MAE) of 7.1% was that by Dorao and Fernandino, which is a function of Re_{tp}. Some correlations were shown to be overly dependent on the effect of gravity and were not applicable for the present μg_e database. A Separated Flow Model for annular condensation was employed to predict $\overline{h}_{tp}$. The model's physical basis makes it seamlessly adaptable for μg_e, and it resulted in a MAE of 32.3%.

1. Introduction

1.1. Two-phase systems in aerospace applications

Two-phase thermal management systems harness the working fluid's latent heat through boiling and condensation. During phase change, heat transfer coefficients are orders of magnitude greater than those of single-phase systems, which rely solely on the sensible heat of the working fluid. Improved heat transfer enables for reductions in the size and weight of thermal management system components [1]. Because of this, two-phase thermal management systems have fostered attention for use in various aerospace applications, where minimizing the system footprint is crucial. Future space missions will rely on two-phase flow for thermal control of spacecraft and planetary habitats, Rankine-cycle power systems, and storage and transfer of cryogenic fuels [2].

Thermal engineers tasked with the design of two-phase systems for aerospace applications require a comprehensive understanding of gravity's effect on two-phase flow physics. Fig. 1 depicts the range of gravity levels relevant to the study of two-phase flow for aerospace

* Corresponding author.
E-mail address: mudawar@ecn.purdue.edu (I. Mudawar).
1 Website: https://engineering.purdue.edu/BTPFL

https://doi.org/10.1016/j.ijheatmasstransfer.2025.127602
Received 1 November 2024; Received in revised form 15 December 2024; Accepted 24 July 2025
Available online 9 August 2025

Nomenclature

A_c	cross sectional area [m^2]
Bd	Bond number, $g(\rho_f - \rho_g)D^2/\sigma$
c	constant
c_p	specific heat [J/kg-K]
D	diameter [m]
D_e	equivalent heat transfer diameter, $4A_c/P_h$ [m]
D_h	hydraulic diameter [m]
f	friction factor
Fr_{fo}	liquid only Froude number, $G^2/\rho_f^2 gD$
Fr_g	vapor Froude number, $(xG)^2/\rho_g^2 gD$
G	mass velocity [kg/m^2s]
g	gravitational acceleration [m/s^2]
g_e	gravitational acceleration on Earth [m/s^2]
μg_e	microgravity [m/s^2]
h	enthalpy [J/kg]; heat transfer coefficient [W/m^2K]
$\overline{h}$	average heat transfer coefficient [W/m^2K]
$\overline{h}_{qw}$	pseudo average heat transfer coefficient based on total heat transfer [W/m^2K]
h_{fg}	latent heat of vaporization [J/kg]
J_g	dimensionless velocity, $J_g = xG/\left(gD\rho_g(\rho_f - \rho_g)\right)^{0.5}$
k	thermal conductivity [W/m-K]
L	length [m]
$\dot{m}$	mass flow rate [kg/s]
N	number of data points
n	measurement station
Nu	Nusselt number
$\overline{Nu}$	average Nusselt number
Nu_{tp}	Nusselt number in the two-phase region, $h_{tp}D/k_f$
$\overline{Nu}_{tp}$	average Nusselt number over the two-phase region
P_h	perimeter for heat transfer [m]
p	pressure [Pa]
p_r	reduced pressure
Pr	Prandtl number
Pr_{tp}	two-phase mixture Prandtl number, $x\mathrm{Pr}_g + (1-x)\mathrm{Pr}_f$
q	heat [W]
q''	heat flux [W/m^2]
Δq	incremental heat transfer [W]
R^2	coefficient of determination
Re_f	liquid Reynolds number, $(1-x)GD/\mu_f$
Re_{fo}	liquid only Reynolds number, GD/μ_f
Re_g	vapor Reynolds number, xGD/μ_g
Re_{tp}	two-phase mixture Reynolds number, $\mathrm{Re}_f + \mathrm{Re}_g$
Su_{go}	vapor only Suratman number, $\rho_g \sigma D/\mu_g^2$
T	temperature [°C]
$\overline{T}$	average temperature [°C]
ΔT_{sh}	fluid superheat, $\Delta T_{sh} = T_f - T_{sat}$ [°C]
U	uncertainty
u	velocity, [m/s]
u^*	friction velocity, $\sqrt{\tau_{wall}/\rho}$, [m/s]
We_{go}	vapor only Weber number, $G^2D/\rho_g\sigma$
X	Lockhart-Martinelli parameter
x	flow quality
x_e	thermodynamic equilibrium quality, $x_e = \frac{h - h_f\|_p}{h_{fg}\|_p}$
y	coordinate perpendicular to tube wall, [m]
y^+	dimensionless wall distance, yu^*/ν
z	streamwise coordinate [m]
Δz	incremental distance [m]

Greek symbols

β	aspect ratio ($\beta \le 1$)
δ	condensate film thickness, [m]
θ	orientation angle of channel, [°]
μ	dynamic viscosity, [Pa-s]
ν	kinematic viscosity, [m^2/s]
ξ_{30}	percentage of datapoints predicted within ±30%, [%]
ξ_{50}	percentage of datapoints predicted within ±50%, [%]
ρ	density, [kg/m^3]
σ	surface tension, [N/m]; standard deviation
τ	shear stress, [Pa]
φ	two-phase multiplier

Subscripts

BHM	corresponding to BHM
c	core
f	saturated liquid; bulk fluid
fo	liquid only
g	saturated vapor
go	vapor only
k	either liquid or vapor phase
i	inner
in	inlet
int	interfacial
loss	heat loss between the BHM inlet and the CM-HT inlet
n	measurement station
o	outer
out	outlet of channel's heated section; outlet
power	electric power supplied
ss	stainless steel
sat	saturation
T	turbulent
tp	corresponding to the two-phase length where $0 \le x_e \le 1$
w	water
wall	wall

Acronyms

ANN	artificial neural network
BHM	bulk heater module
CM-HT	condensation module for heat transfer
FBCE	flow boiling and condensation experiment
FBM	flow boiling module
FIR	fluids integrated rack
FSML	fluids system module – lower
FSMU	fluids system module – upper
GRC	NASA's Glenn Research Center
ISS	International Space Station
ITCS	ISS thermal control system
MAE	mean absolute error
nPFH	n-perfluorohexane
RDAQM	remoted data acquisition module
RTD	resistance temperature detector
VES	vacuum exhaust system

applications, along with several examples. Gravity levels range from microgravity (μg_e) in orbiting vehicles to hypergravity in accelerating fighter aircraft. Unfortunately, most correlations and models for two-phase flows have only been validated for terrestrial applications and could be unreliable in other gravitational environments [3]. This can be detrimental during boiling in reduced gravity, where weakened buoyancy fails to remove vapor from the heated surface. However, the severity of this consequence will vary by the cooling scheme implemented, each with advantages and disadvantages. Passive schemes relying on capillary flows [4] have low power requirements and few components but are limited to relatively low heat loads. Pool boiling [5] is simple to implement but suffers from vapor accumulation near the heated surface and low critical heat flux under reduced gravity. Falling films [6] are driven by gravity and become inoperable in μg_e. Spray cooling [7] dissipates high heat fluxes while maintaining uniform surface temperatures by dispersing liquid droplets over the surfaces, which has proven useful in cryogenic fuel delivery and chill down. Jet impingement [8] is capable of dissipating extreme heat fluxes, but requires high pumping power, especially when scaled up with multiple jets. Flow boiling [9,10] is an excellent candidate for aerospace thermal management, requiring moderate pumping power and relying on fluid motion to flush bubbles away from the heated surface. Micro-channel flow boiling [11] can be employed to tackle high power densities, but confinement effects in reduced gravity should be considered. It is also possible to employ hybrid cooling schemes [12,13] to take advantage of multiple configurations.

Condensation is the conjugate process to boiling in any closed two-phase loop and reverts the working fluid back to its liquid state. Due to the relatively low heat fluxes during condensation as compared to boiling, condensers are generally larger than their evaporator counterparts [14]. Optimizing the size of the condenser is crucial to reduce the footprint of the system but requires accurate predictions of condensation heat transfer. Therefore, reliable condensation data in μg_e is required to develop and validate predictive models that can be employed to optimize condensers in space applications.

1.2. Experimental investigations of condensation in microgravity

Brief periods of μg_e are commonly achieved via drop tower, parabolic flight, or sub-orbital rocket [15]. Parabolic flights have been the primary method pursued by previous investigators of μg_e condensation, but difficulty achieving steady state during the ~20 s of μg_e has been reported. Some researchers have drawn conclusions on the influence of gravity by analyzing the transient response as the μg_e period is entered. Reinarts et al. [16] studied a condensing flow of R12 in a copper tube. Heat was rejected to water flowing countercurrent in an annulus around the copper tube. Steady state conditions were approached at the end of the μg_e period but were not completely established. Regardless, heat transfer degraded by 26% in μg_e. This was attributed to a transition to annular flow, where a uniform liquid film prevents condensation at the surface in microgravity. Contrarily, enhanced heat transfer observed in Earth gravity (g_e) and $2g_e$ was attributed to buoyancy induced thinning of the liquid film along the top of the tube.

Lee et al. [17] performed flow condensation experiments onboard a parabolic flight, achieving steady conditions for 1 – 2 s during most of their experiments. Two distinct test sections were employed. One, for detailed heat transfer measurements of FC-72 condensing within a stainless-steel tube, and the other allowed for visual observation of FC-72 condensing on the outer surface of a stainless steel tube. At low flow rates, the liquid film was smooth and laminar, with axially decreasing heat transfer coefficients. The condensate film was circumferentially uniform around the tube in μg_e but thickened along the

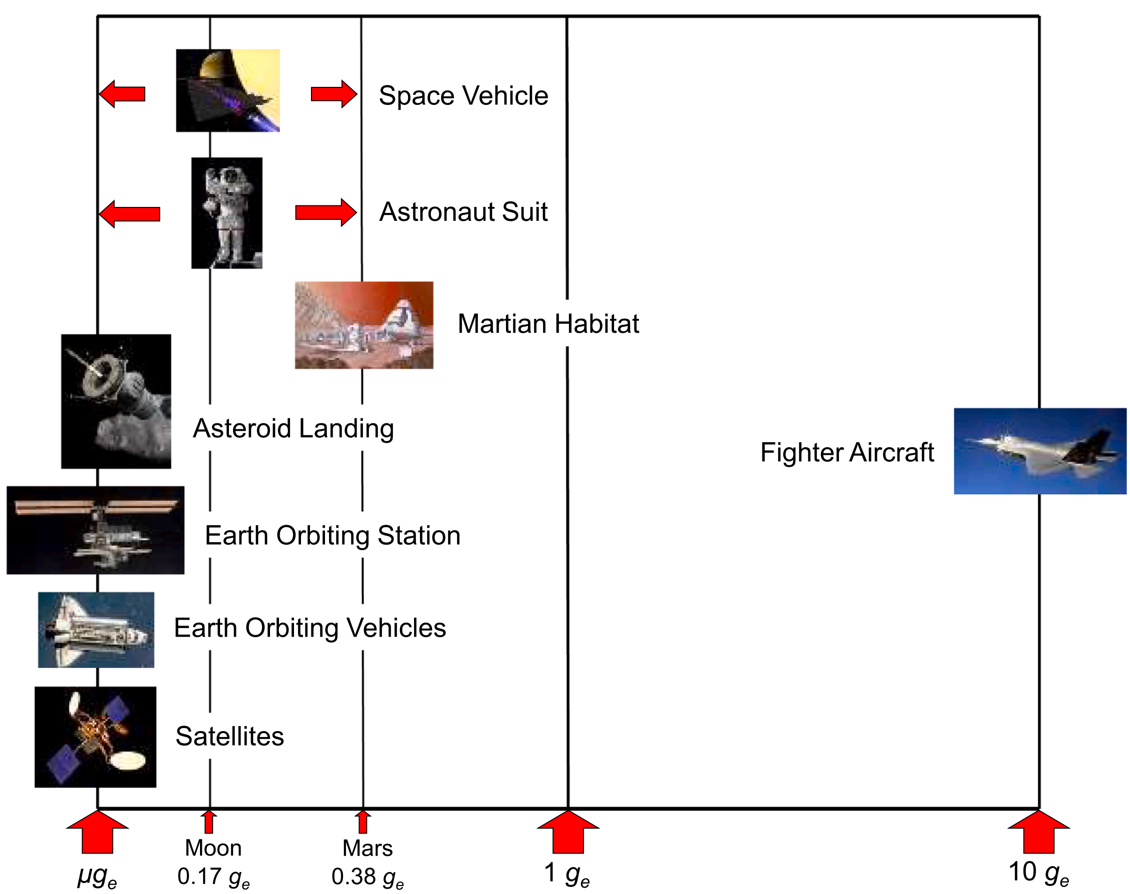

Fig. 1. Aerospace applications suitable for two-phase thermal management and their corresponding gravity levels.

bottom of the tube at higher gravity levels. At higher flow rates, heat transfer coefficients increased slightly in the downstream region as the liquid film transitioned to turbulent and the interface became wavy. The influence of gravity on the liquid film was mitigated by interfacial shear at high flow rates, resulting in an axisymmetric liquid film at all gravity levels.

A condensing flow of HFE-7000 within a copper tube was examined during parabolic flight by Azzolin et al. [18]. The authors developed a thermal model to quantify transient effects in their experiments, and only considered data where the transient component accounted for less than 10% of total heat transfer. Local heat transfer coefficients decreased with quality, while the influence of gravity depended on operating conditions. Comparing results in μg_e and g_e, average heat transfer coefficient decreased by ~20% in μg_e at the lowest mass velocity, $G = 70$ kg/m^{2}s, but was nearly constant at high mass velocity, $G = 170$ kg/m^{2}s. A sight glass in the middle of the condensing length revealed a uniform film thickness in μg_e, but asymmetry in g_e as buoyancy drained liquid towards the bottom of the tube. Berto et al. [19] expanded on this study and investigated lower mass velocities of $G = 30 – 50$ kg/m^{2}s. The discrepancy in heat transfer between μg_e and g_e continued to grow as flow rate decreased. The corresponding thickening of the liquid film along the top side of the tube in μg_e resulted in a 77% reduction in heat transfer coefficient in μg_e compared to g_e at $G = 30$ kg/m^{2}s.

Condensation experiments of HFE-7100 on a single fin were performed during parabolic flight by Glushchuk et al. [20]. The authors reported difficulty achieving steady state and growth of the liquid film during μg_e. Surface tension became dominant, which tends to minimize the surface area of the liquid film, in μg_e and heat transfer coefficients decreased. The influence of surface tension magnified the effect of local convexities or concavities along the fin's surface in μg_e. This was further investigated during condensation experiments of HFE-7100 on a cylindrical pin fin [21]. Stable data approaching steady state were reported and did not show significant variations in measured values. The inverse Bond number, characterizing the ratio between body force and the surface tension force, was influential in areas where the fin's curvature varied, and the film thickness rapidly changed. Variations in inversed Bond number demarcated the pin into 7 different regions, with areas strongly influenced by surface tension pressure gradient contributing to over 10% of total heat transfer.

The scarcity of condensation data acquired in a steady reduced gravity environment has prompted researchers to explore alternative methods to investigate the effects of gravity on condensation. The simplest technique to analyze gravity's influence on condensation is to compare results performed at different flow orientations [22–25] in g_e. This has been adopted by numerous researchers to investigate gravity's influence on liquid film development, and its impact on heat transfer. During horizontal flow, buoyancy results in asymmetry of the liquid film around the channel. The thin liquid film along the top of the channel permits high heat transfer rates, while the thicker liquid film along the bottom impedes heat transfer. In vertical upflow and downflow, the flow regime is predominantly annular and symmetrical. However, the heat transfer during vertical downflow is more efficient as the co-current body force thins the liquid film. Some researchers have extrapolated upon this idea to investigate condensation at intermediate channel orientations [26,27]. Heat transfer and void fraction were most sensitive to the channel orientation at low mass velocities and low vapor quality. A slight decline from the horizontal, between 10° and 30°, resulted in optimal heat transfer performance. In this range, condensation heat transfer is aided by the stratification of horizontal flows and gravity assisting liquid removal from the channel. However, the orientation became less influential at high mass velocities and vapor qualities. Under these conditions, the condensate liquid film is expected to be thinner, and the velocity of the vapor is relatively high, resulting in shear dominant flows. This concept has been expanded upon to develop criteria to ensure the flow remains shear dominated and independent of gravity [28].

In the absence of experimental opportunities, numerical simulations have been employed to investigate condensation in μg_e. Numerical simulations can be a powerful tool to predict heat transfer performance in μg_e [29] and make comparisons between the development of the liquid film in μg_e and g_e [30,31]. However, reliable μg_e data are still required to validate the results [32].

1.3. Flow Boiling and Condensation Experiment (FBCE)

The *Flow Boiling and Condensation Experiment* (FBCE) is a collaborative endeavor between researchers at the Purdue University Boiling and Two-Phase Flow Laboratory (PU-BTPFL) and the NASA Glenn Research Center (GRC). The overarching goal is to acquire steady μg_e flow boiling and condensation data onboard the International Space Station. The FBCE system is unique in its capability to investigate both flow boiling and condensation with a single flow loop by replacing only the test section.

Thus far, results from the flow boiling component of the experiment, employing the Flow Boiling Module (FBM), have been reported in detail. The simultaneous acquisition of flow visualization and wall temperature measurements provided insights into observed parametric trends regarding μg_e flow boiling heat transfer with subcooled [33,34] and saturated [35] inlet conditions. The critical heat flux results for subcooled inlet [36] and saturated inlet [37] were parametrically investigated and utilized to assess available correlations and models. During experiments with highly subcooled inlet conditions, liquid backflow into the channel was observed. This was further investigated in dedicated experiments performed in μg_e and g_e with an elevated data acquisition rate of 30 Hz [38]. Various heat transfer correlations available in the literature were assessed for their applicability for μg_e flow boiling, and new highly accurate artificial neural networks (ANNs) for predicting flow boiling heat transfer and critical heat flux were developed [39]. Similarly, a consolidated pressure drop database was utilized to conduct a thorough assessment of experimental trends, correlations, and flow models [40]. A new ANN has been developed to provide superior predictions, regardless of heating configuration or inlet conditions.

1.4. Objectives of study

This study reports the heat transfer results of μg_e flow condensation experiments performed onboard the ISS, as part of FBCE. Experiments were performed with a tube-in-tube counterflow heat exchanger, called the Condensation Module for Heat Transfer (CM-HT), and investigated the condensation of nPFH within a stainless-steel tube with a 7.24 mm inner diameter. Heat is rejected through the stainless-steel tube to a counter current stream of cooling water. Experiments were performed for broad ranges of nPFH mass velocities, G, inlet thermodynamic equilibrium qualities, $x_{e,in}$, inlet pressures, p_{in}, and water mass velocities, $\underline{Gw}$, enabling a detailed parametric assessment of key variables affecting local and average heat transfer coefficients. The μg_e database is used to assess various correlations and an analytical model for predicting condensation heat transfer coefficient in μg_e.

2. Experimental methods

2.1. Condensation Module for Heat Transfer (CM-HT)

The test section, called the Condensation Module for Heat Transfer (CM-HT), is a tube-in-tube, counterflow heat exchanger and is illustrated schematically in Fig. 2. n-Perfluorohexane (nPFH), which is selected for its potential in aerospace applications [41], flows through a stainless steel tube with an inner diameter 7.24 mm, as shown in Fig. 2(a). A honeycomb flow straightener is placed within CM-HT near the nPFH inlet, before the condensing length, to straighten streamlines, break down large eddies, and mitigate any influence of the 90° bend at the

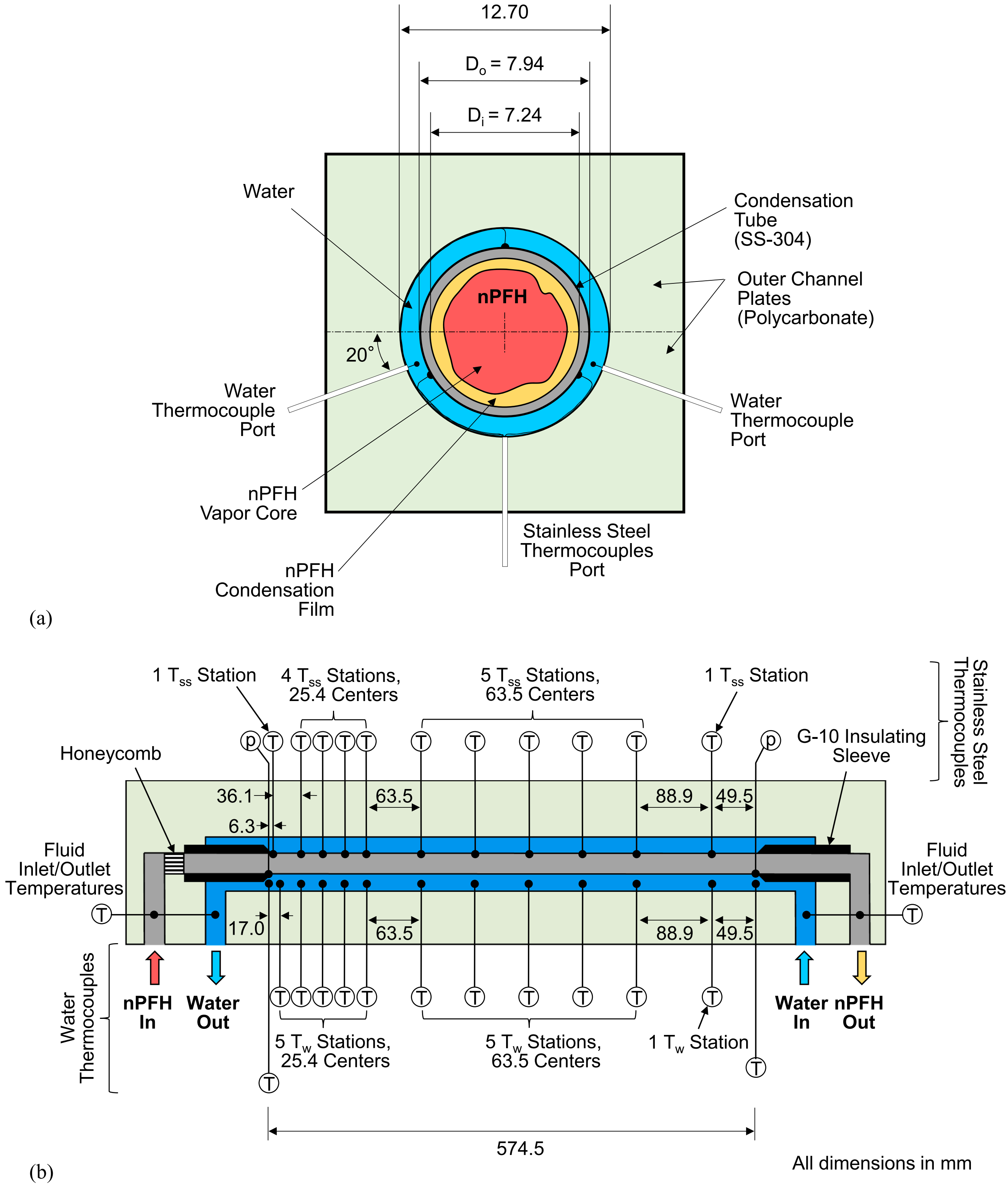

Fig. 2. Schematic representations of Condensation Module for Heat Transfer (CM-HT) depicting the (a) circumferential and (b) axial locations of thermocouples.

inlet to CM-HT. nPFH condenses along the 574.5 mm length, *L*, permitting heat rejection to cooling water supplied by the ISS Thermal Control System (ITCS). Water flows countercurrent to the nPFH through an annulus formed by the 7.94 mm outer diameter of the stainless steel tube and a 12.70 mm diameter circular channel machined into the insulating polycarbonate surrounding the stainless steel tube. Insulating G10 sleeves cover the stainless steel tube to prevent heat transfer from the nPFH to the water upstream and downstream of the 574.5 mm condensing length. The polycarbonate block is constructed by clamping together two pieces of polycarbonate between aluminum support plates and is instrumented with numerous thermocouples and pressure transducers for detailed heat transfer measurements.

The temperatures of the nPFH and water are measured at their respective inlets and outlets to CM-HT by type-E thermocouples inserted directly into the flow. At the upstream and downstream edge of the heat transfer length, the nPFH pressure is measured by absolute pressure transducers, and the water temperature is measured in the annulus. Water pressure measurements are made upstream and downstream of CM-HT. The temperatures of the outer wall of the stainless steel tube and the water within the annulus are each measured at 11 stations along the length of the channel, as shown in Fig. 2(b). Circumferential placements of thermocouples are shown in Fig. 2(a). At each stainless steel temperature measurement station, 3 type-E thermocouples are tack-welded to the outer-wall of tube, 120° apart. Each water temperature measurement station contains 2 type-E thermocouples inserted into the flow, located 20° below the midline of the channel. Fig. 2(b) shows that the temperature measurement stations are concentrated towards the nPFH inlet, where axial variations in temperature are expected to be rapid in response to the development of the condensate film. Towards the nPFH outlet, stations are spaced further apart, where axial variations are expected to be less dynamic.

2.2. Two-phase flow loop and integration onboard the ISS

A schematic of the flow loop is presented in Fig. 3 and is identical to that used for the flow boiling component of FBCE [33], except for the test section. Flow is driven by a positive displacement internal gear pump. Two relief valves are attached in parallel paths across the pump and are set to open if the pressure difference across the pump exceeds 199.95 kPa and 206.84 kPa, respectively, with the latter serving as a backup. A Coriolis flow meter measures the flow rate immediately downstream of the pump and provides feedback to the pump's flow controller. The fluid passes through a filter prior to entering the preheater, called the Bulk Heater Module (BHM). The BHM heats the subcooled liquid to achieve the desired conditions at the inlet of CM-HT, either superheated vapor or saturated two-phase mixture. The fluid passes through CM-HT, where detailed heat transfer data are collected as the fluid rejects heat to the cooling water supplied by the ISS Thermal Control System (ITCS). The nPFH exits CM-HT as a saturated two-phase mixture or subcooled liquid. Any residual heat gained by the nPFH in the BHM is lost in another fluid to water heat exchanger, labeled condenser, downstream of CM-HT. Water is supplied by the ITCS to the FBCE system at a mass flow rate of 35 g/s and is divided between CM-HT and the condenser. Along the flow path to either component, water passes through a flow meter that provides feedback to a valve that regulates the water flow rate to the respective component. A static mixer positioned downstream of the condenser ensures the fluid is thermodynamically uniform before reaching the pump inlet.

An accumulator, which serves as a reference point for system pressure and helps mitigate two-phase instabilities [42], is connected at a T-junction between the static mixer and pump inlet. The accumulator holds additional nPFH on one side of stainless steel bellows and air on the other. The airside pressure is controlled by an air pump and vent valve.

Two parallel paths exist between the T-junction connecting the accumulator and the pump inlet. One path is used during degassing and contains a degassing contactor connected to the ISS's Vacuum Exhaust System (VES). The fluid was routinely degassed before data collection to ensure the partial pressure of noncondensable gases remained below 2 kPa. The other path, used during normal operation, routes the fluid directly from the T-junction to the pump inlet.

Pressure and temperature of the fluid are measured at various locations around the loop by pressure transducers and thermocouples and RTDs, respectively. Most valves are solenoid actuated to enable remote operation onboard the ISS.

The FBCE system is packaged into discrete components that are connected to the Fluids Integrated Rack (FIR) onboard the ISS. The FIR provides access to various onboard resources including Space Acceleration Measurement System (SAMS), Environmental Control System (ECS), Electrical Power Control Unit (EPCU), VES, ITCS, as well as the

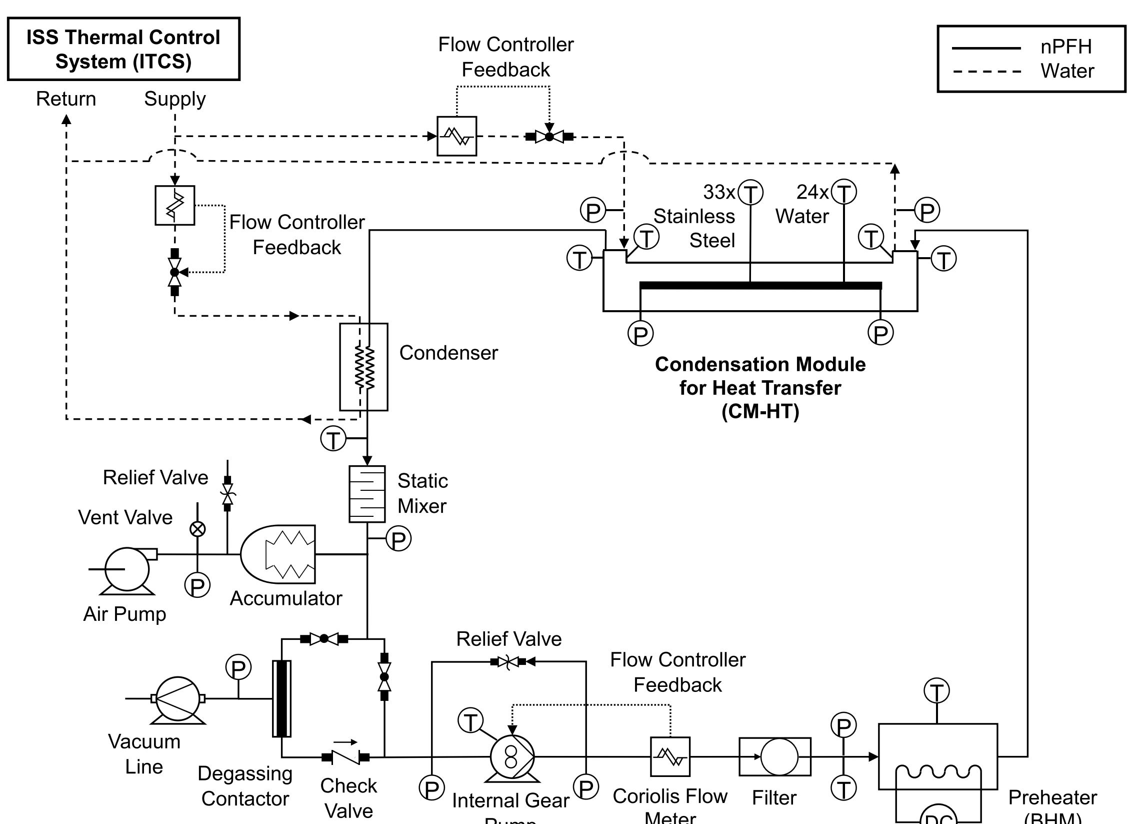

Fig. 3. Schematic diagram of two-phase flow loop used for flow condensation experiments.

Confocal Control Unit (CCU) and Imaging Processing Storage Unit – Camera Link (IPSU-CL) for image capture and storage during FBM testing. The flow loop components are contained in 6 modules for easy integration onboard ISS. The majority of the flow loop is housed in the Fluids System Module Upper (FSMU) and Fluids System Module Lower (FSML), shown in Fig. 4 through photographs and CAD renderings. The FSMU is connected to the VES and contains the degassing contactor, gear pump, flow meter, mass flow controller, and filter. The FSML receives water from the ITCS via the FIR's Water Interface Panel (WIP) and houses the condenser, static mixer, and the accumulator. CM-HT, pictured in Fig. 5, is deployed as the Test Module Assembly (TMA) in the present study but can be interchanged with FBM. The BHM is stored in its own module, as shown in Fig. 6. Heat is supplied to the fluid by three 120 V and three 28 V DC powered heaters, with a duplicate set of each that serve as back up. The BHM is equipped with thermocouples and RTDs that provide feedback to a safety circuit that shuts down the heaters if the surface temperature or the BHM outlet temperature exceeds 130°C and 100°C, respectively. The last two components, shown at the bottom of Fig. 6, are the Remote Data Acquisition Modules (RDAQM1 and RDAQM2). RDAQM1 is dedicated to thermocouple measurements, and RDAQM2 records the remainder of signals around the flow loop. Fig. 7 depicts the layout of the modules in the FIR and a schematic of the connections between different modules, the ITCS, and the VES.

2.3. *Experimental procedure and operating conditions*

The experiment was controlled remotely from the Telescience Center at GRC with an in-house software, and astronaut interaction is not required after installation. Sensor data was collected at a sampling rate

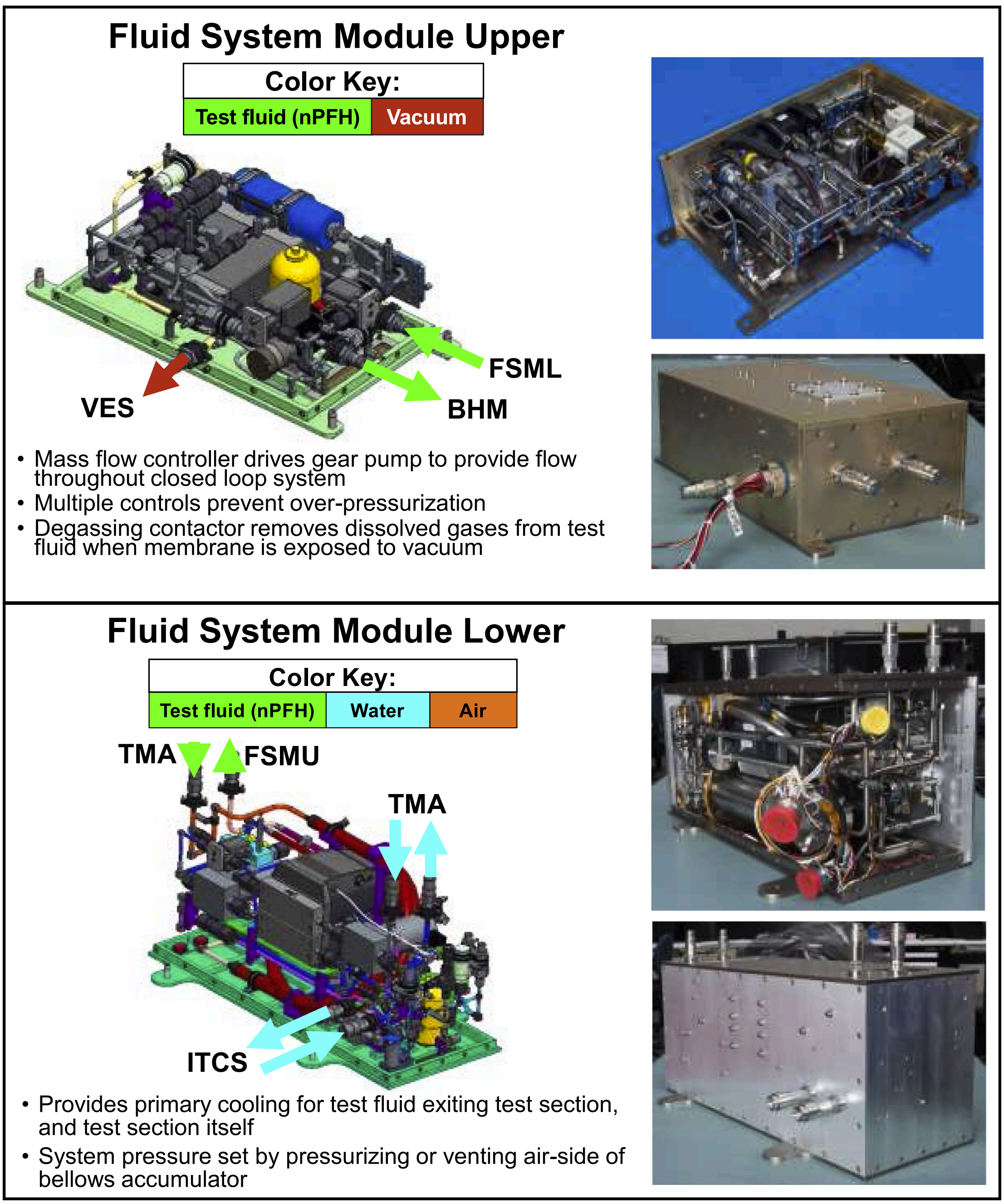

Fig. 4. Images and CAD renderings of Fluid System Module Upper (FSMU) and Fluid System Module Lower (FSML).

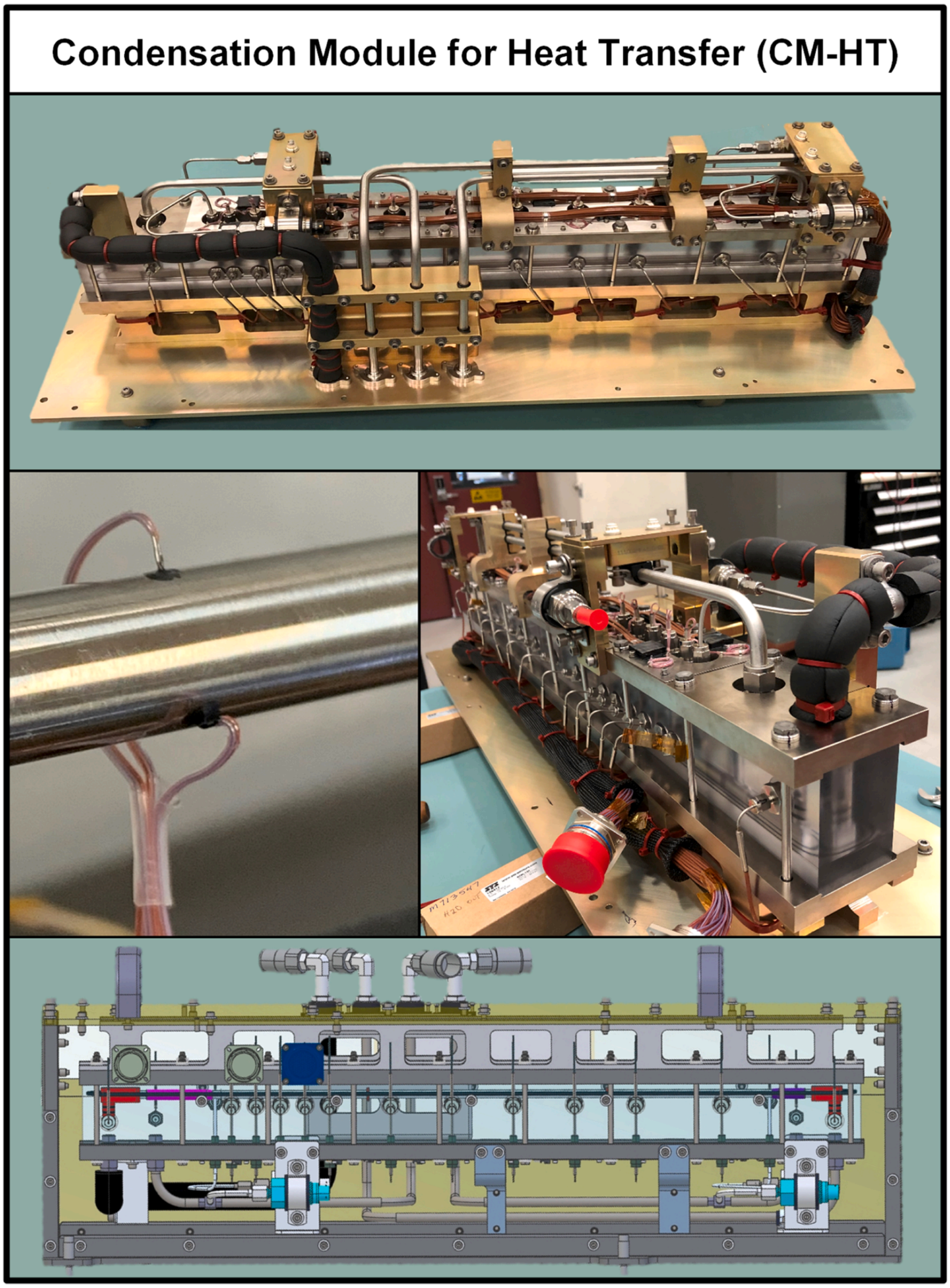

Fig. 5. Images and CAD rendering of the Condensation Module for Heat Transfer (CM-HT).

of 5 Hz during steady state data collection and 1 Hz during other periods. Collected data is routinely transmitted back to GRC.

Prior to testing, the nPFH was degassed for several hours each day to reduce the quantity of noncondensable gas in the fluid. This is necessary to mitigate the effects of any air leaks exposed when the system rests in a sub-atmospheric state, a safety requirement onboard the ISS. To initialize each run, the desired inlet conditions, including nPFH mass velocity, G, pressure, p_{in}, temperature, T_{in}, thermodynamic equilibrium quality, $x_{e,in}$, and water mass velocity, G_w, based on the annular cross section, are set within the software, and the pump speed, accumulator air-side pressure, BHM power, and valves connected to the ITCS are adjusted to achieve these conditions. A sufficient amount of time is allowed for the system to become steady after which, data is recorded for a 5-minute period at 5 Hz. The final 2 min of collected data are averaged to obtain the steady values reported in this study. After completing the test point, new operating conditions are uploaded, and the process is repeated.

The operating conditions investigated in this study are detailed in Table 1. The nPFH inlet conditions varied within the capabilities of the system. However, the flow loop is incapable of further conditioning the water-side of CM-HT beyond the mass velocity, G_w, and the water inlet temperature, $T_{w,in}$, and pressure, $p_{w,in}$, are relatively constant as shown in Table 1.

The inlet enthalpy, h_{in}, is determined as

$$h_{in} = \begin{cases} h|_{T_{in},p_{in}} & T_{in} > T_{sat} \\ h_{BHM,in} + \dfrac{q_{BHM}}{\dot{m}} & T_{in} = T_{sat}. \end{cases} \tag{1}$$

During superheated inlet conditions, h_{in} is evaluated at the measured T_{in} and p_{in} of superheated vapor. All thermophysical properties in the present study are determined using REFPROP [43]. During saturated inlet, h_{in} is calculated from an energy balance over BHM as shown in Eq.

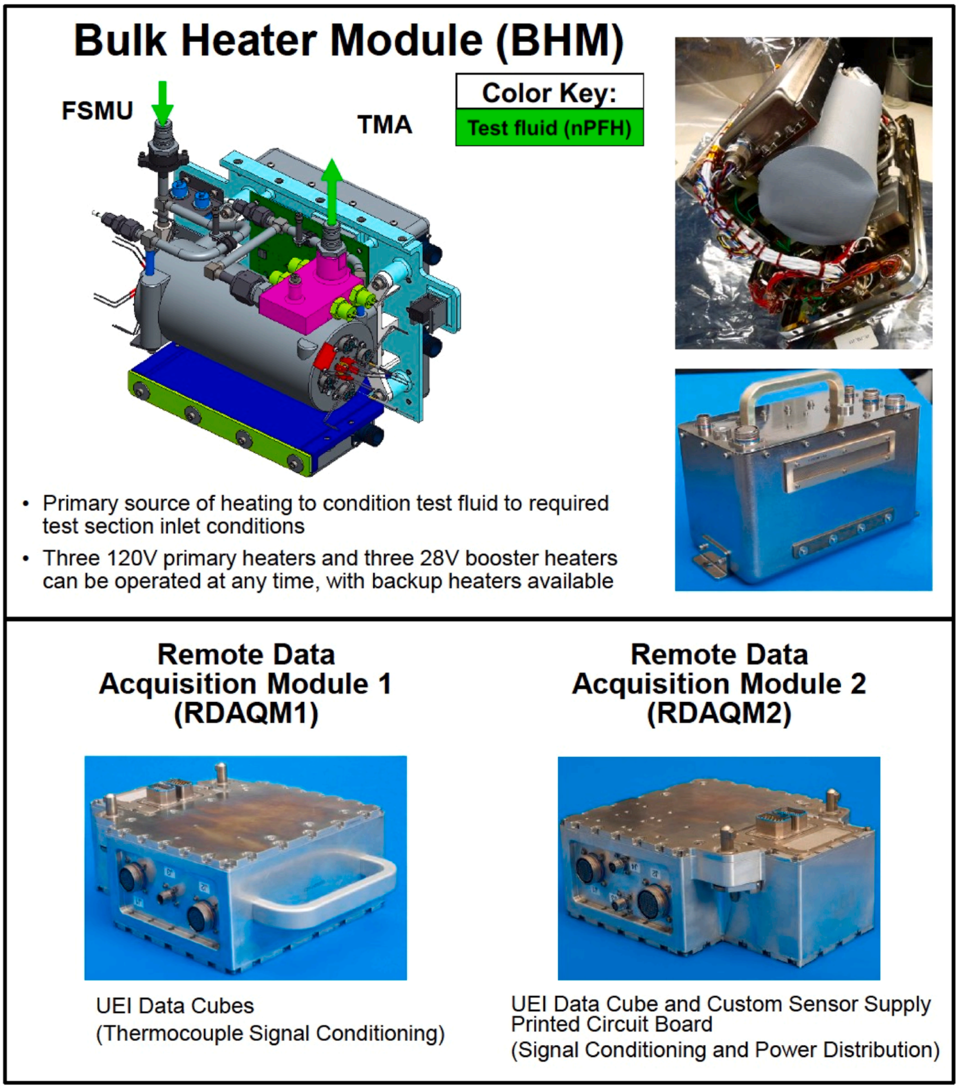

Fig. 6. Bulk Heater Module (BHM) and Remote Data Acquisition Modules 1 and 2 (RDAQM1 and RDAQM2).

(1), where $h_{BHM,in}$ is the enthalpy of the subcooled liquid at the BHM inlet and is directly evaluated at the measured BHM inlet temperature, $T_{BHM,in}$, and pressure, $p_{BHM,in}$. The net heat gained by the fluid from the BHM, q_{BHM}, is determined by correcting the measured electric power supplied to the BHM heaters, q_{power}, for heat loss between the inlets of BHM and CM-HT. Heat loss during saturated inlet conditions is estimated from cases with superheated inlet conditions, where the fluid is at a single-phase state at both the BHM and CM-HT inlets, and q_{BHM} can be determined by comparing the q_{power} to the change in enthalpy of the fluid. A simple curve fit is developed to estimate the percentage of heat loss as

$$\%q_{loss} = 1 - \frac{q_{BHM}}{q_{power}} = 0.108\dot{m}^{-0.803}\left(\frac{T_{in} + 273.15}{331.15}\right)^{5.423}. \tag{2}$$

The state of the fluid is determined via the thermodynamic equilibrium quality, calculated as

$$x_e = \frac{h - h_f|_p}{h_{fg}|_p}, \tag{3}$$

where h is local enthalpy and both h_f, saturated liquid enthalpy, and h_{fg}, latent heat of vaporization, are evaluated at local pressure, e.g., $x_{e,in}$ is determined by evaluating Eq. (3) at h_{in} and p_{in}. The fluid is superheated when $x_e > 1$, saturated when $0 \le x_e \le 1$, and subcooled when $x_e < 0$.

2.4. Heat transfer coefficient determination and uncertainty

Extraction of heat transfer data requires additional processing of the experimental measurements. As detailed in Section 2.1, stainless steel and water-side temperatures are each recorded at 11 measurement stations within CM-HT. The measured stainless steel and water temperatures at each station are averaged to obtain a single value for their respective temperatures. This implies heat transfer is axisymmetric allowing for the determination of heat transfer coefficients via a one-dimensional radial energy balance. In μg_e, the lack of buoyancy precludes stratification associated with horizontal flow in g_e, and the flow regime is expected to be symmetric, similar to vertical flow in g_e [44].

Water temperatures, T_w, including the inlet, outlet, and 11 stations within CM-HT are curve-fitted to obtain a continuous and differentiable water temperature profile. A third-order polynomial fit, which has previously been used to good effect [17,24] and is applied in this study. The third-order polynomial accurately captures variations in water temperature without over constraining the data and results in an average R^2 of 0.96 and minimum R^2 of 0.92.

The gradient of the water temperature profile is used to calculate the local heat transfer from the condensing nPFH. For an incremental length

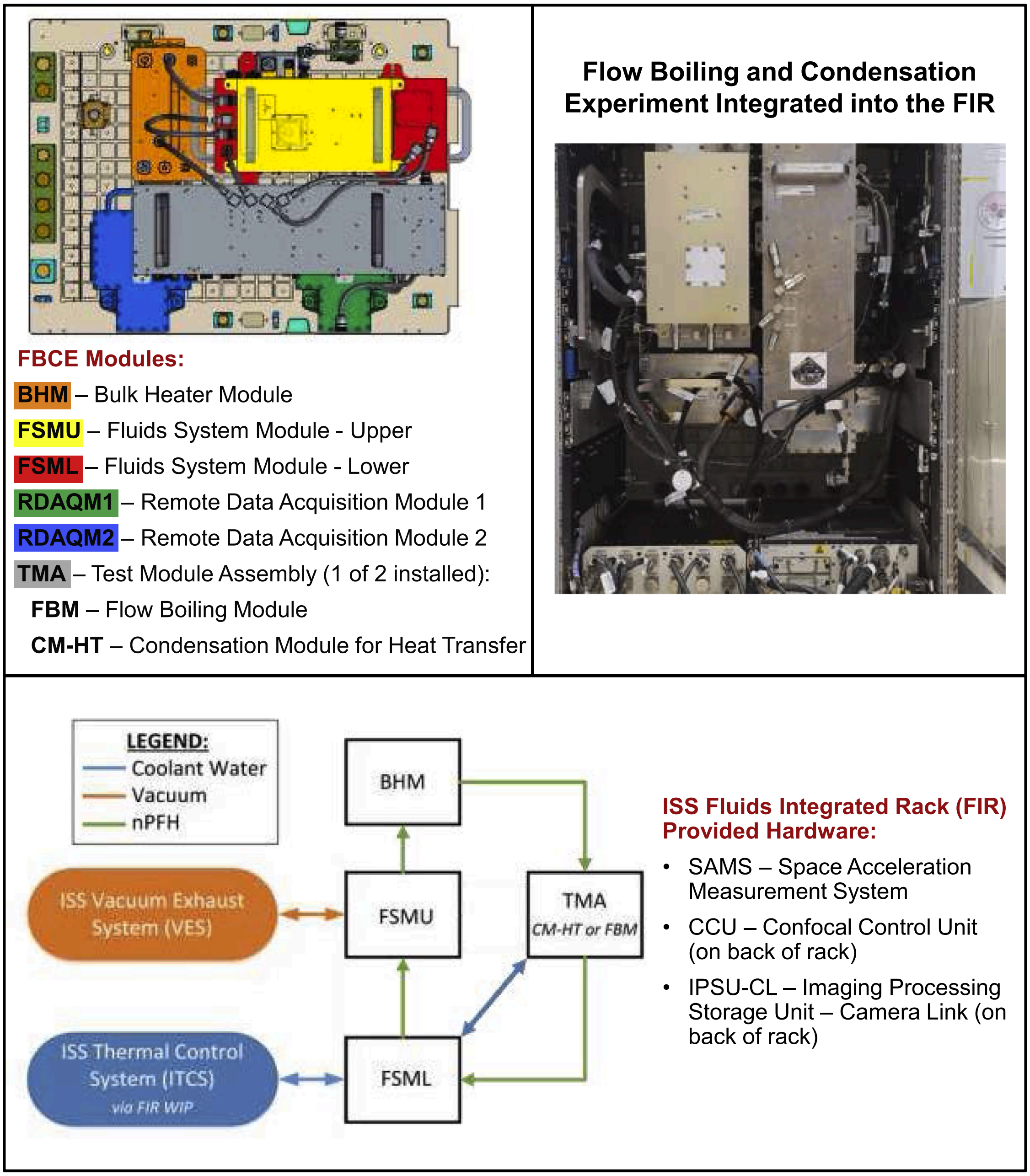

Fig. 7. Layout of the Flow Boiling and Condensation Experiment (FBCE) modules on the Optics Bench of the Fluids Integrated Rack (FIR), the integration of FBCE into the FIR, and connections to the ISS provided hardware.

Table 1
Summary of steady state parameters obtained during microgravity flow condensation experiments onboard the ISS. The corresponding experiments are listed in Appendix A.

Mass flowrate, $\dot{m}$	3.0 – 12.0 g/s
Mass velocity, G	72.8 – 291.5 kg/m^{2}s
Inlet pressure, p_{in}	103.9 – 160.2 kPa
Inlet temperature, T_{in}	58.5 – 82.1°C
Inlet superheat, $\Delta T_{sh,in}$	0.0 – 17.7°C
Inlet thermodynamic equilibrium quality, $x_{e,in}$	0.28 – 1.19
Mass flowrate, $\dot{m}_w$	10.0 – 25.0 g/s
Water-side mass velocity, G_w	129.4 – 324.7 kg/m^{2}s
Water-side inlet pressure, $p_{w,in}$	263.5 – 293.5 kPa
Water-side inlet temperature $T_{w,in}$	17.7 – 18.9°C

of Δz at measurement station n, the corresponding incremental heat transfer, Δq_{cond}, is

$$\Delta q_{cond,n} = \dot{m}_w c_{p,w} \left[\frac{dT_w}{dz}\right]_n \Delta z. \tag{4}$$

As mentioned previously, heat transfer is assumed to be axisymmetric, as depicted schematically in Fig. 8. The stainless steel tube's inner temperature, $T_{ss,i}$ is obtained via radial conduction from the measured outer surface temperature, $T_{ss,o}$, as

$$T_{ss,i,n} = T_{ss,o,n} + \Delta q_{cond,n} R_{cond,n} = T_{ss,o,n} + \dot{m}_w c_{p,f,w} \left[\frac{dT_w}{dz}\right]_n \left[\frac{\ln(D_o/D_i)}{2\pi k_{ss}}\right]. \tag{5}$$

Local heat transfer coefficient, h, at station n is defined as

$$h_n = \frac{\Delta q_{cond,n}}{\pi D_i \Delta z \left(T_{f,n} - T_{ss,i,n}\right)}, \tag{6}$$

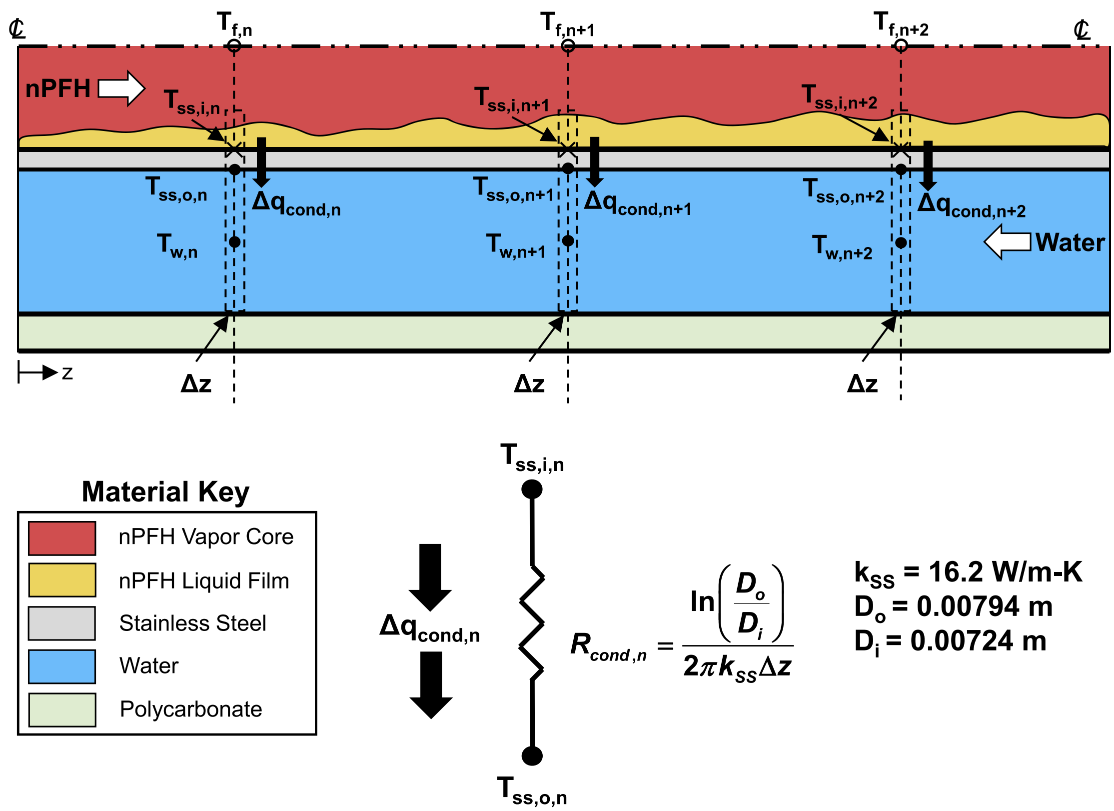

Fig. 8. Schematics of axisymmetric heat transfer from the nPFH vapor core to cooling water supplied.

While the nPFH temperature is not measured along the tube, local fluid temperature, $T_{f,n}$ is equal to the local saturation temperature, T_{sat}, in the saturated region, $0 \leq x_{e,n} \leq 1$, or is dependent on the local pressure and enthalpy in the upstream superheated region, $x_{e,n} > 1$, and downstream subcooled region, $x_{e,n} < 0$. The x_e of nPFH along the tube is tracked by an energy balance between stations n and n+1, resulting in

$$x_{e,n+1} = x_{e,n} - \frac{\dot{m}_w c_{p,w}\left(T_{w,n} - T_{w,n+1}\right)}{\dot{m} h_{fg}}. \tag{7}$$

The average two-phase heat transfer coefficient, $\overline{h}_{tp}$ is obtained by averaging h over the two-phase length of the tube, L_{tp}, where $0 < x_{e,n} < 1$. This is performed numerically as

$$\overline{h}_{tp} = \frac{1}{L_{tp}} \int_0^{L_{tp}} h(z)dz = \frac{\sum_{j=1}^{n_{tp}} h_j \Delta z_j}{\sum_{j=1}^{n_{tp}} \Delta z_j}, \tag{8}$$

where Δz_j is the distance centered between consecutive measurement stations and n_{tp} is the number of locations with $0 \leq x_{e,n} \leq 1$.

The methodology proposed by O'Neill et al. [24] is employed to calculate heat transfer coefficient uncertainty in the present study. Eqs. (4) and (6) are combined to obtain a comprehensive equation for h_n, and the uncertainty of the water temperature derivative is approximated as the measured temperature difference between consecutive thermocouples. Assuming the measured dimensions of the tube are exact, h_n uncertainty, U_h, is calculated as

$$\left[\frac{U_h}{h_n}\right]^2 = \left[\frac{U_{\dot{m}}}{\dot{m}_w}\right]^2 + 2\left[\frac{U_{T_w}}{T_{w,n+1} - T_{w,n}}\right]^2 + \left[\frac{U_{T_f}}{T_{f,n} - T_{ss,i,n}}\right]^2 + \left[\frac{U_{T_{ss}}}{T_{sat,n} - T_{ss,i,n}}\right]^2. \tag{9}$$

Uncertainties of the other parameters are based on instrumentation and given as $U_{\dot{m}} = 0.002\dot{m}_w$, $U_{Tw} = 0.2$°C, $U_{Tf} = 0.1$°C, and $U_{Tss} = 0.2$°C. While Type-E thermocouples typically have an uncertainty of 0.5°C, extensive calibration of each thermocouple in CM-HT at GRC provides a maximum uncertainty of 0.2°C. The primary contributor to U_h is the change in T_w between consecutive stations, which is relative to U_{Tw}. This results in high U_h, approaching 100% in some cases, which should be considered when interpreting local results. Regardless of the high local U_h, the uncertainty of $\overline{h}_{tp}$, $\overline{U_h}$, remains below 34% and is calculated as

$$\overline{U_h} = \frac{1}{L_{tp}} \sqrt{\sum_{j=1}^{n_{tp}} U_{h,j}^2 \Delta z_j^2}. \tag{10}$$

3. Experimental results and discussion

3.1. Axial temperature profiles

Prior to analysis of experimental trends of h, it is worth discussing the transformation of the measured temperatures along the channel to the corresponding processed heat flux, q'', and h. The first step is to average the stainless steel and water temperatures measured at each station to obtain a single value for each temperature, respectively. Fig. 9 depicts plots of the measured outer T_{ss} and T_w along the tube for various operating conditions, and a profile obtained by averaging at each station. The variations in T_w at each station are relatively low and typically within 1°C of each other. An exception to this is observed at a lower G_w in Fig. 9(b), where the water thermocouple station near the nPFH inlet has a relatively large spread. This is attributed to slight asymmetries in the upstream region as the liquid film develops, resulting in an asymmetric q''. At low G_w, the sensible heat gain of the water results in larger temperature difference than at higher G_w, magnifying any circumferential variations in q''. This same T_w profile is observed consistently at low G_w for all G.

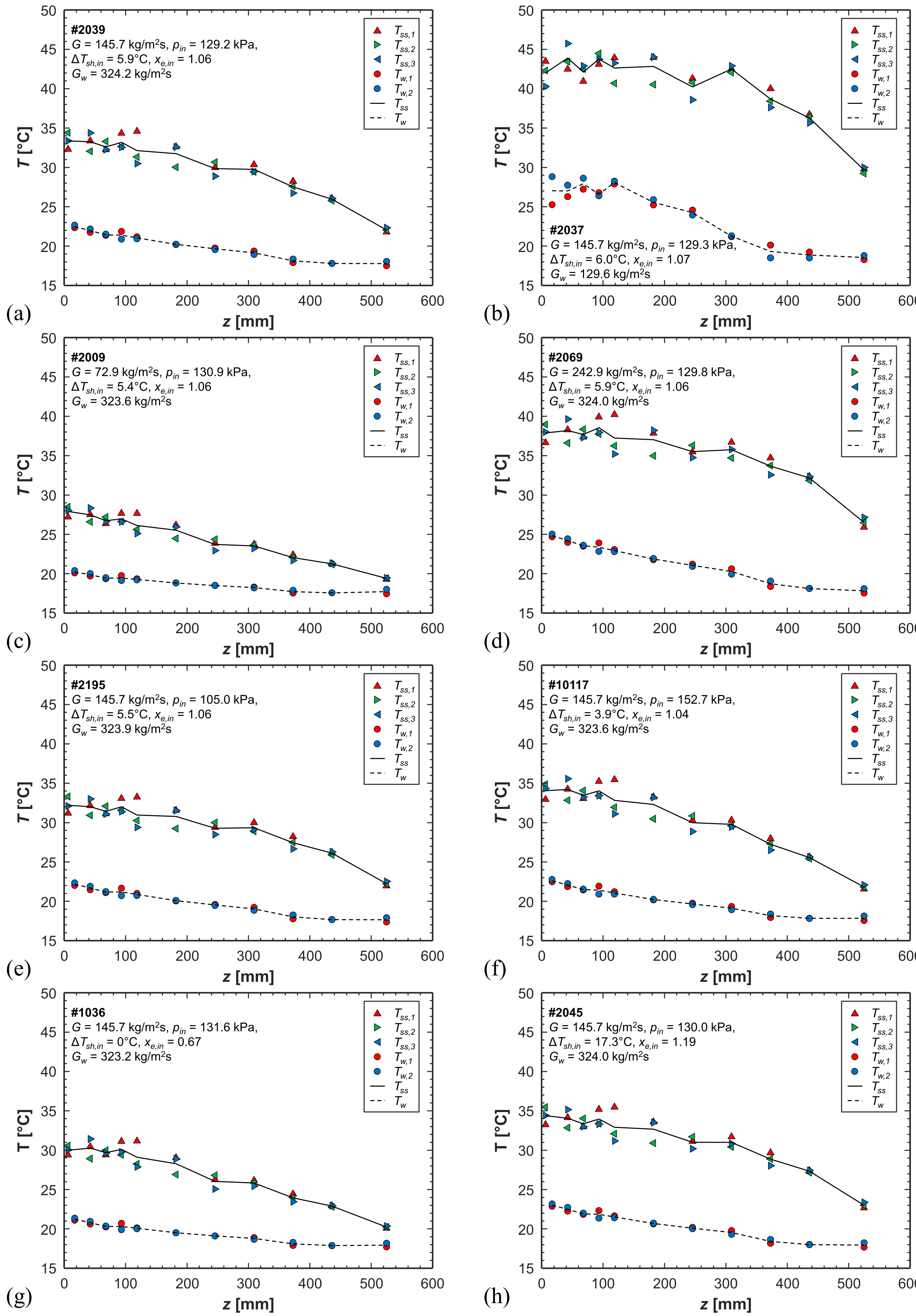

Fig. 9. Plots depicting temperatures measured along the channel for (a) intermediate conditions with mass velocity, $G = 145.7$ kg/m^{2}s, inlet pressure, $p_{in} = 129.2$ kPa, inlet superheat, $\Delta T_{sh,in} = 5.9$°C, and water mass velocity $G_w = 324.2$ kg/m^{2}s, (b) lower G_w of $G_w = 129.6$ kg/m^{2}s, (c) lower G of $G = 72.9$ kg/m^{2}s, (d) higher G of $G = 242.9$ kg/m^{2}s, (e) lower p_{in} of $p_{in} = 105.0$ kPa, (f) higher p_{in} of $p_{in} = 152.7$ kPa, (g) lower $\Delta T_{sh,in}$ of $\Delta T_{sh,in} = 0.0$°C, and (h) higher $\Delta T_{sh,in}$ of $\Delta T_{sh,in} = 17.3$°C.

Generally, a $2 - 3°C$ spread is observed circumferentially at each T_{ss} measurement station in the upstream portion of the channel. This results in some nonmonotonic behavior in the upstream temperatures, indicating a nearly constant surface temperature in the upstream region. Overall, T_{ss} decreases along the channel, and the circumferential spread in the thermocouples decreases. This could be due to greater sensitivity to asymmetries in q'' upstream where the liquid film is thinner. The spread in T_{ss} appears greater in Fig. 9(b) and 9(d), where the measured temperatures are greater, otherwise trends are consistent across all operating conditions.

The spread in the temperatures and the influence of the mean temperature is measured by the by the standard deviation, σ, of temperatures along the channel. At each measurement station the standard deviation for the T_w and T_{ss} is calculated as,

$$\sigma = \sqrt{\frac{1}{N-1}\sum_{j=1}^{N}\left(T_j - \overline{T}\right)^2} \tag{11}$$

where N is the number or thermocouples at the station and T is either the T_w or T_{ss}. The σ of measured temperatures shown in Fig. 9 are presented in Fig. 10. As observed in Fig. 9, the T_{ss} exhibits larger spread than T_w, and σ of T_w is generally below 1. The one outlier of T_w occurs at the first measurement station in Fig. 10(b) with $G_w = 129.6$ kg/m^{2}s. However, the σ of all T_{ss} in Fig. 10 remain below 3. A previous study employing CM-HT in conjunction with the Condensation Module for Flow Visualization, where the latter was used for flow visualization, confirmed that symmetric flow occurred when σ of T_{ss} remained below 3°C [44], validating the axisymmetric assumption used in extracting heat transfer coefficients. The highest σ for T_{ss} is observed at 118.6 mm, which does reach 3 for some cases, otherwise the highest σ observed in the entire database is 2.6°C.

As observed in Fig. 9, the trends of temperature measurements are relatively consistent across a broad range of operating conditions, and the influence of various parameters on heat transfer coefficients will be further examined in the following sections. However, one exception was the temperature profile at lower G_w in Fig. 9(b), where a larger spread of T_w was present. Fig. 11 continues the data processing procedure and presents the averages of measured $T_{ss,o}$, T_w, the curve fit of T_w, and the calculated T_f, T_{sat}, $T_{ss,i}$ along the channel. The cases shown include the intermediate operating conditions presented in Fig. 9(a) and 9(b), with slightly superheated inlet conditions, $\Delta T_{sh,in} = 5.9 - 6.0°C$, and an intermediate nPFH mass velocity, $G = 145.7$ kg/m^{2}s. The influence of G_w on the processed heat transfer data is examined by assessing the processed heat transfer data at three G_w, including $G_w = 324.2$ kg/m^{2}s, 226.8 kg/m^{2}s, and 129.6 kg/m^{2}s in Fig. 11(a–c), respectively. Examining the highest G_w in Fig. 11(a), the fluid is slightly superheated at the upstream thermocouple, $x_e > 1$, saturated throughout most of the channel, $0 \le x_e \le 1$, and subcooled at the last two measurement stations, $x_e < 0$. The stainless steel temperatures are relatively constant in the upstream region of the channel, and the radial temperature difference across the tube is the greatest within the channel. This is attributed to high h and q'' upstream, where the condensate liquid film is the thinnest. Stainless steel temperatures and the radial temperature difference across the tube decrease along the channel as the liquid content in the channel increases and x_e decreases. This results in monotonically decreasing q'' along the length of the channel, which is significantly degraded near the nPFH outlet, evidenced by the asymptotic behavior of T_w downstream. Similarly, h decreases along the length of the channel, with some deviation upstream where the fluid is superheated and the T_f is higher than T_{sat}. However, q'' is greatest and h is relatively high upstream due to nonequilibrium effects causing condensation regardless of the $T_f > T_{sat}$ and $x_e > 1$.

Fig. 11(b) depicts a case with intermediate G_w exhibiting similar trends to those in Fig. 11(a). The stainless steel temperatures are slightly higher than those at higher G_w due to a corresponding decrease in water-side heat transfer coefficient. This causes a slight degradation of local q'' and h, which is exasperated at the lowest G_w in Fig. 11(c). Higher T_w upstream and reduced water-side heat transfer coefficient limit q'' and impede condensation upstream compared to higher G_w in Fig. 11(a) and 11(b). Consequently, a nonmonotonic trend in q'' is observed in Fig. 11 (c). Abnormal variations in q'' are similarly reflected in measured T_w, slightly reducing the quality of the curve fit, $R^2 = 0.95$, compared to Fig. 11(a) and (b), $R^2 = 0.98$ and 0.97, respectively. This trend is possibly caused by the larger spread in measured T_w at low G_w, as shown in Fig. 9(b).

The influence of G_w is further investigated in Fig. 12(a), which shows the variations of sensible heat gain of the water, q_w as a function of G_w with inlet conditions of $p_{in} \approx 130$ kPa, $\Delta T_{sh,in} \approx 5°C$, and various G. It is worth noting that the heat rejected from the nPFH, calculated via enthalpy difference between the nPFH inlet and outlet, agrees within 3.1% of q_w on average across all cases, verifying conservation of energy across CM-HT. At low G, q_w is nearly independent of G_w. However, q_w becomes increasingly sensitive to G_w as G increases, suggesting that q_w is limited by the water-side heat at low G_w, leading to a reduced condensation rate, specifically near the nPFH inlet where the film is expected to be thin. The consequence of this is observed in Fig. 11, where consistent trends are observed in q'' and h at $G_w = 324.2$ kg/m^{2}s and 226.8 kg/m^{2}s, corresponding to $q_w = 570.6$ and 542.7 W, respectively. At $G_w = 129.6$ kg/m^{2}s, an abnormal q'' profile is observed resulting in a decrease of q_w to 470.8 W. Generally, the variations of q_w with G_w are less than 5% for $G \le 150$ kg/m^{2}s with $G_w \ge 226$ kg/m^{2}s, and for $G > 150$ kg/m^{2}s q_w is assumed to be independent of G_w only for $G_w \ge 323$ kg/m^{2}s. This is evidenced in Fig. 12(b–f), which show the variation in h with G_w at $G =$ 72.9 kg/m^{2}s, 97.2 kg/m^{2}s, 145.7 kg/m^{2}s, 194.3 kg/m^{2}s and 242.9 kg/m^{2}s, respectively. At $G = 72.9$ kg/m^{2}s and 97.2 kg/m^{2}s, Fig. 12(b) and 12(c), respectively, h at $G_w \approx 227$ kg/m^{2}s and 324 kg/m^{2}s are equal while noticeably lower at $G_w \approx 130$ kg/m^{2}s. In Fig. 12(d), $G = 145.7$ kg/m^{2}s, slight deviations in h are observed in the upstream region between $G_w \approx 227$ kg/m^{2}s and 324 kg/m^{2}s. However, the trend of h with respect to x_e is preserved, unlike at $G_w \approx 130$ kg/m^{2}s where heat transfer is limited by the water side. The deviations between h at $G_w \approx 227$ and 324 kg/m^{2}s become larger, in Fig. 12(e) and 12(f) with $G = 194.3$ and 242.9 kg/m^{2}s, respectively. At $G_w \approx 227$ kg/m^{2}s, h is limited and levels off at high x_e due to limitations on the water-side heat transfer. Hence, for $G >$ 150 kg/m^{2}s, h is considered independent of G_w only for $G_w \approx 324$ kg/m^{2}s.

The remainder of the study will focus on the subset of the database independent of G_w. Measured T_{ss} in the G_w independent portion of the database had a maximum σ of 2.8°C at the fifth station and otherwise remains below 2.0°C, suggesting the flow is axisymmetric. However, the experimental results for the entire database, including the G_w dependent section, and an abbreviated analysis is provided in appendix B.

3.2. Parametric trends of local heat transfer coefficients

The effect of p_{in} on h is explored in Fig. 13, which presents results at three different p_{in} for various G. At each G, the different p_{in} results in nearly identical h. However, at high x_e, h is consistently slightly higher at lower p_{in}. This trend could be attributed to lower h_{fg} at higher p resulting in a greater rate of condensation, thickening of the liquid film, and decreasing heat transfer coefficient. Conversely, higher p_{in} yields slightly higher h at low x_e, which could be a result of lower saturated liquid viscosity, μ_f, at higher p due to the increase in T_{sat}, enhancing liquid convection. Overall, the variations of h with respect to p_{in} are minor, and further results will be presented for intermediate p_{in} and focus on more pertinent trends.

Thus far, only data with slightly superheated inlet conditions has been presented. Fig. 14(a–c) presents plots of h as a function of x_e for different G with superheated inlet conditions, $\Delta T_{sh,in} = 14.1 - 17.3°C$, $8.9 - 9.8°C$, and $5.3 - 6.3°C$, respectively. Fig. 14(d) features saturated inlet conditions with $\Delta T_{sh,in} = 0°C$ and $x_{e,in} = 0.59 - 0.84$. For each range

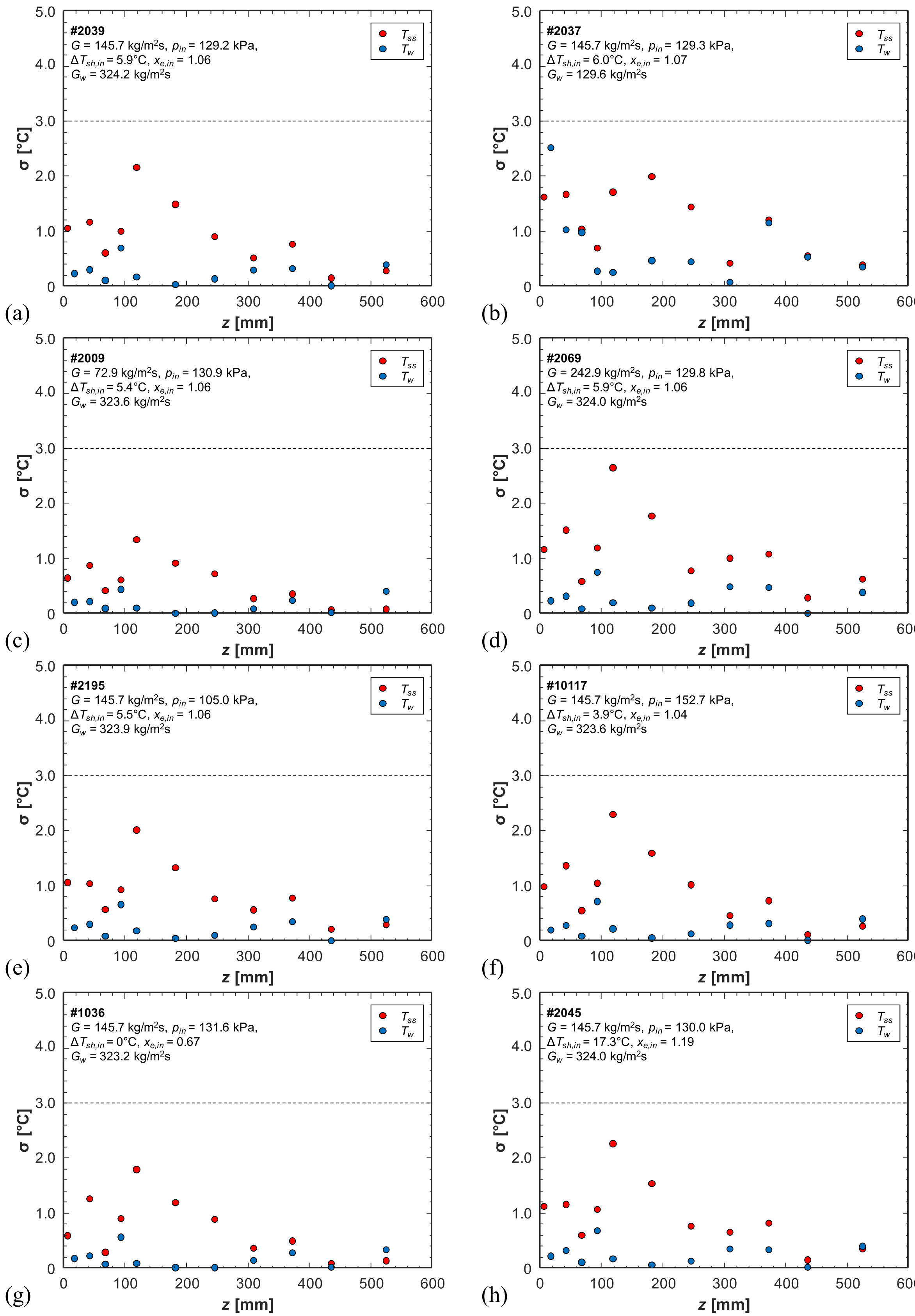

Fig. 10. Plots of the standard deviation, σ, of temperatures measured along the channel for (a) intermediate conditions with mass velocity, $G = 145.7$ kg/m^{2}s, inlet pressure, $p_{in} = 129.2$ kPa, inlet superheat, $\Delta T_{sh,in} = 5.9$°C, and water mass velocity $G_w = 324.2$ kg/m^{2}s, (b) lower G_w of $G_w = 129.6$ kg/m^{2}s, (c) lower G of $G = 72.9$ kg/m^{2}s, (d) higher G of $G = 242.9$ kg/m^{2}s, (e) lower p_{in} of $p_{in} = 105.0$ kPa, (f) higher p_{in} of $p_{in} = 152.7$ kPa, (g) lower $\Delta T_{sh,in}$ of $\Delta T_{sh,in} = 0.0$°C, and (h) higher $\Delta T_{sh,in}$ of $\Delta T_{sh,in} = 17.3$°C.

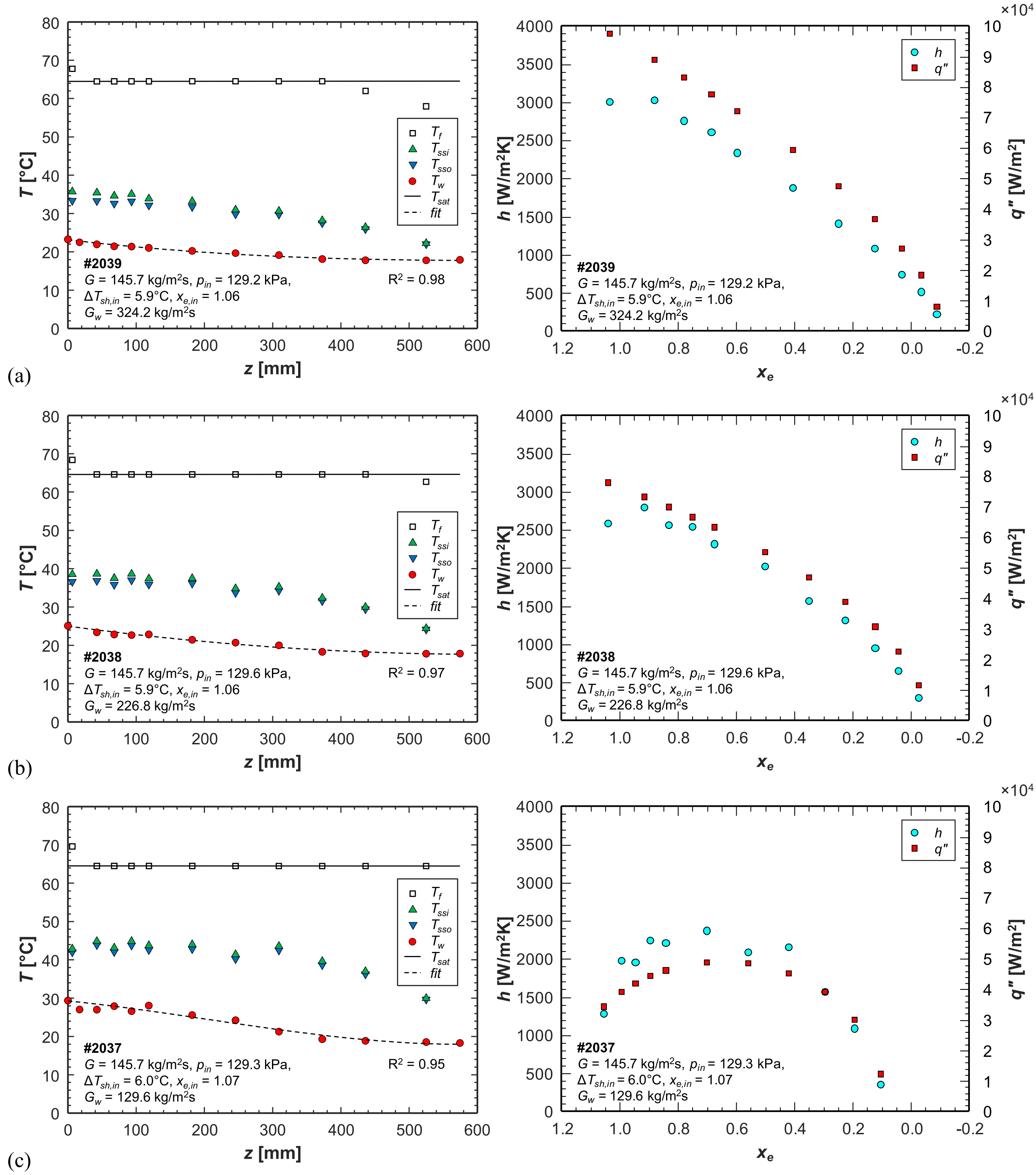

Fig. 11. Comparison of temperatures along the channel to the corresponding processed heat transfer results with inlet superheat of $\Delta T_{sh,in}$ = 5.9 – 6.0°C, and an intermediate nPFH mass velocity, G = 145.7 kg/m^{2}s, at three water mass velocities (a) G_w = 324.2 kg/m^{2}s, (b) 226.8 kg/m^{2}s, and (c) 129.6 kg/m^{2}s.

of $\Delta T_{sh,in}$, G has a definitive influence on h. At high $x_{e,in}$, h increases with G due to the enhancement of interfacial shear stress thinning the liquid film and promoting heat transfer. As x_e decreases, h decreases and converges for all G. This is primarily due to reduced heat transfer in the downstream portion of the channel where the liquid film is the thickest, resulting in low h. However, no noticeable difference is apparent between the different $x_{e,in}$ in Fig. 14(a–d). This trend is more apparent in plots of h as a function of x_e at different $x_{e,in}$, shown in Fig. 15(a–f) for G ≈ 73 kg/m^{2}s, 97 kg/m^{2}s, 146 kg/m^{2}s, 194 kg/m^{2}s, 243 kg/m^{2}s, and 292 kg/m^{2}s, respectively. At each G, h is independent $x_{e,in}$ and is primarily a function of G and local x_e. There are slight variations for the saturated inlet cases in Fig. 15(c–f), likely caused by inherent minor inaccuracies in calculating the $x_{e,in}$ during two-phase inlet.

The entire subset of the database independent of G_w, (i.e., all p_{in} with $G_w \approx$ 324 kg/m^{2}s and $G_w \approx$ 227 kg/m^{2}s with G ≤ 150 kg/m^{2}s), is presented in Fig. 16(a). As previously discussed, h is enhanced by increasing G at high x_e, but, as x_e decreases, h decreases and converges for different G. The maximum h observed for each G occurs near the location of

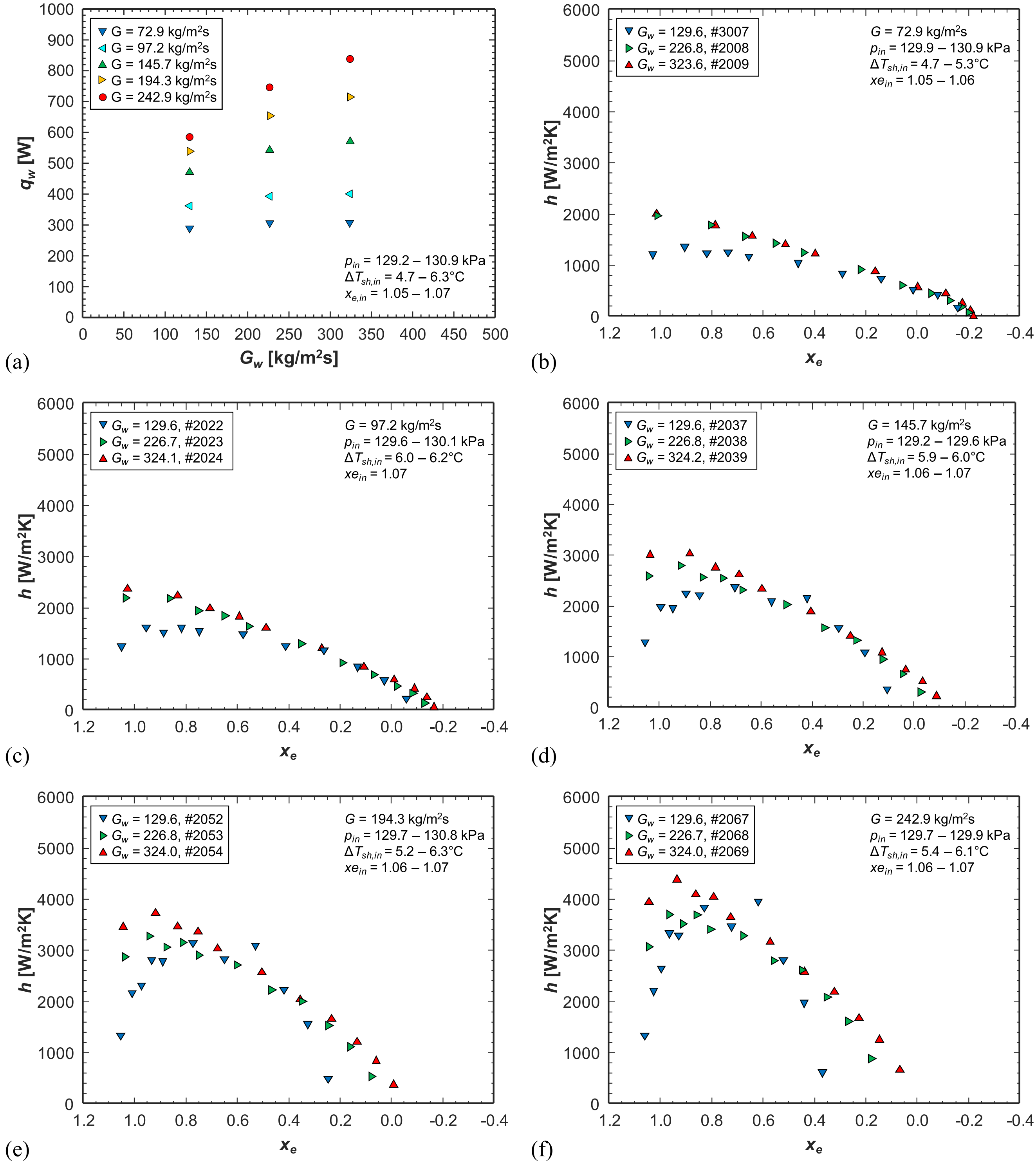

Fig. 12. Plots depicting variations in (a) water sensible heat gain, q_w, with respect to water mass velocity, G_w, and local heat transfer coefficient, h, with respect to thermodynamic equilibrium quality, x_e, at different G_w for nPFH mass velocities of (b) $G \approx 73$ kg/m^{2}s, (c) $G \approx 97$ kg/m^{2}s, (d) $G \approx 146$ kg/m^{2}s, (e) $G \approx 194$ kg/m^{2}s, and (f) $G \approx 243$ kg/m^{2}s. Cases are shown for an inlet pressure of $p_{in} \approx 130$ kPa and inlet superheat of $\Delta T_{sh,in} \approx 5°$C.

saturated vapor, $x_e = 1$. Further upstream, the superheated T_f results in slightly reduced h, and, further downstream, h decreases monotonically with x_e as the liquid film thickens. This is highlighted in Fig. 16(b), which isolates the heat transfer coefficient over the saturated two-phase length of the channel, h_{tp}, where $0 \leq x_e \leq 1$. This subset of the data is used to track variations with quality, x, assuming equilibrium, where $x = x_e$ in the saturated region.

Variations of h_{tp} are commonly correlated to liquid Reynold's number, Re_f, which is dependent on x and G in the saturated region and shown in Fig. 16(c). The y-axis is nondimensionalized as the Nusselt number along the two-phase region, Nu_{tp}. While the plots in Fig. 16(b) and 16(c) appear different, similar trends are revealed. Nu_{tp} increases with G and decreases as Re_f increases at a fixed G, corresponding to x decreasing. A more revealing trend is observed in Fig. 16(d), depicting

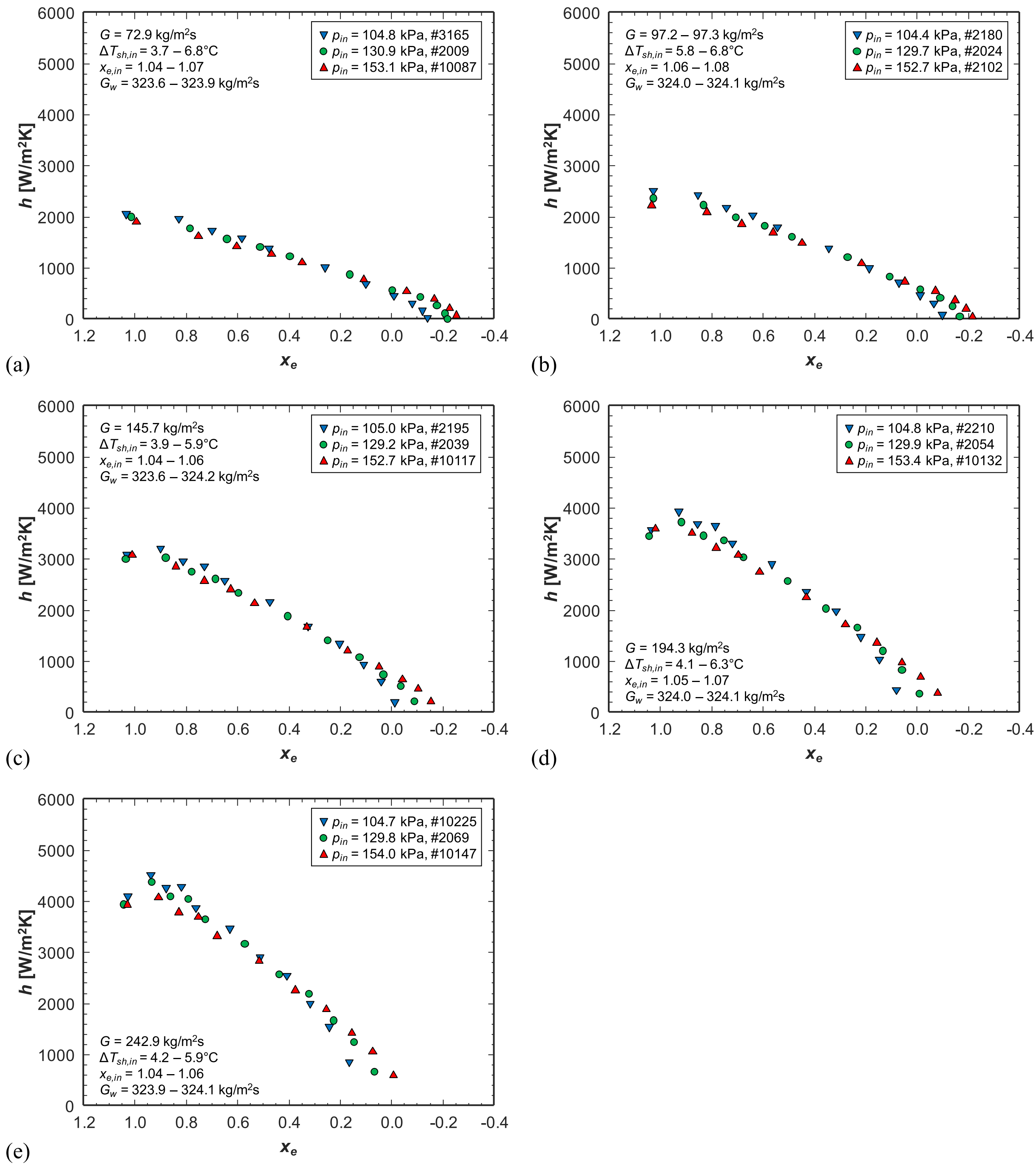

Fig. 13. Plots depicting variations in heat transfer coefficient, h, with respect to thermodynamic equilibrium quality, x_e, at different inlet pressures, p_{in}, for nPFH mass velocities of (a) $G \approx 73$ kg/m^{2}s, (b) $G \approx 97$ kg/m^{2}s, (c) $G \approx 146$ kg/m^{2}s, (d) $G \approx 194$ kg/m^{2}s, and (e) $G \approx 243$ kg/m^{2}s. Cases are shown for an inlet superheat of $\Delta T_{sh,in} \approx 5°$C and water mass velocity of $G_w \approx 324$ kg/m^{2}s.

Nu_{tp} plotted against two-phase mixture Reynold's number, Re_{tp}, which is defined as

$$\mathrm{Re}_{tp} = \mathrm{Re}_f + \mathrm{Re}_g = GD\left[\frac{x}{\mu_g} + \frac{(1-x)}{\mu_f}\right]. \tag{12}$$

Re_{tp} captures the total inertia of the flow relative to the two-phase mixture viscosity, as defined by McAdams et al. [45]. Nu_{tp} at different operating conditions now collapses to a single trend and increases with Re_{tp}. Regardless of G, Re_{tp} is relatively low at low x due to the higher viscosity of the liquid phase, resulting in low Nu_{tp}. This corresponds to reduced variation in h_{tp} for all G at low x in Fig. 16(b). Nu_{tp} increases with Re_{tp}, corresponding to the enhancement of h_{tp} observed in Fig. 16

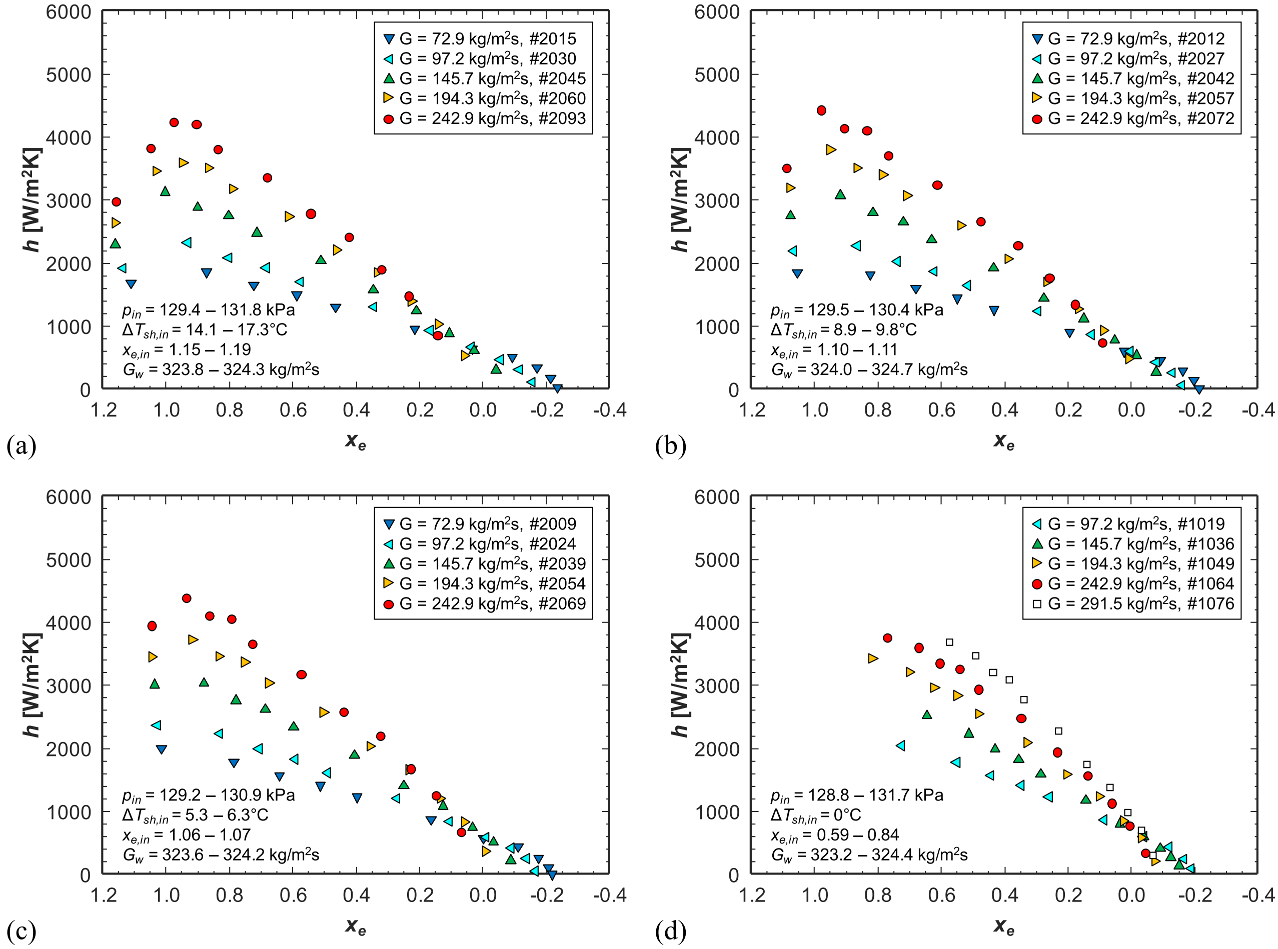

Fig. 14. Plots depicting variations in heat transfer coefficient, h, with respect to thermodynamic equilibrium quality, x_e, at different nPFH mass velocities, G, for inlet superheats of (a) $\Delta T_{sh,in} \approx 15°C$ (b) $\Delta\ T_{sh,in} \approx 10°C$, (c) $\Delta\ T_{sh,in} \approx 5°C$, and (d) $G\ \Delta\ T_{sh,in} \approx 0°C$. Cases are shown for an inlet pressure of $p_{in} \approx 130$ kPa and water mass velocity of $G_w \approx 324$ kg/m^{2}s.

(b) as x and G increase. This further substantiates that h_{tp}, or Nu_{tp}, is primarily dependent on G and local x_e, as discussed with respect to Fig. 14. Fig. 16 reveals that influence of x on Nu_{tp} in the saturated region is relative to viscosity of the two phases, which describes the shear force within the flow. The culmination of these parameters are captured in Re_{tp}, which solely characterizes Nu_{tp} in the present database.

3.3. Channel averaged heat transfer results

As discussed in Section 2.4, h inherently has relatively high uncertainty due to the reliance on T_w measurements to discern q''. However, channel averaged results can be discussed with greater certainty. Fig. 17 presents various averaged results with respect to $x_{e,in}$ for different G. As expected from the observed local results in Fig. 16, heat transfer coefficient averaged over the two-phase length, $\overline{h}_{tp}$, increases with G in Fig. 17(a). Increasing flow inertia enhances interfacial shear stress, thins the liquid film and promotes heat transfer across the liquid film. Increasing $x_{e,in}$ towards a saturated vapor inlet, $x_{e,in} = 1$, increases L_{tp} and enhances $\overline{h}_{tp}$. This is more prominent at high G, where the combination of higher velocities and lesser liquid combine to thin the liquid layer and increase $\overline{h}_{tp}$. Increasing $x_{e,in}$ above 1 and superheating the vapor inlet negligibly affects $\overline{h}_{tp}$. This is due to $\overline{h}_{tp}$ only considering the saturated region of the channel, $0 \le x_{e,in} \le 1$.

However, from a practical standpoint, a superheated inlet slightly enhances average heat transfer coefficient along the channel. Fig. 17(b) shows variations in the heat transfer coefficient averaged over the entire channel, $\overline{h}$, which includes the upstream superheated length, $x_e > 1$, and downstream subcooled length, $x_e < 0$, of the channel. Increasing $x_{e,in}$ decreases the subcooled length downstream, where heat transfer is the lowest, and elongates the superheated region upstream, where superheated condensation enables high q'' and h, as shown in Fig. 16(a). This results in a slight increase $\overline{h}$ over the entire channel as $x_{e,in}$ increases.

Fig. 17(c) and 17(d) show the Nusselt numbers corresponding to the average heat transfer coefficients in Fig. 17(a) and 17(b), respectively. Results mimic the dimensional results and reveal no new information but are included for easy reference if compared to different fluids or geometries.

While the uncertainty of $\overline{h}$ remains below 34%, the dependence on the incremental change in T_w along the channel can be eliminated by considering a pseudo average heat transfer coefficient, $\overline{h}_{qw}$, determined as

$$\overline{h}_{qw} = \frac{q_w}{\pi D_i L\left(T_{sat,in} - \overline{T}_{ss,o}\right)} = \frac{\dot{m}_w c_{p,w}\left(T_{w,out} - T_{w,in}\right)}{\pi D_i L\left(T_{sat,in} - \overline{T}_{ss,o}\right)}. \tag{13}$$

$\overline{h}_{qw}$ is based on q_w, $T_{sat,in}$, and the average $T_{ss,o}$, $\overline{T}_{ss,o}$, which is used in place of the inner wall temperature to eliminate the reliance on local dT_w/dz for conduction through the tube. Each of these values are easily accessible from the experimental measurements. Furthermore, as shown in Fig. 11, the differences between $T_{ss,o}$ and $T_{ss,i}$ are small, specifically near the nPFH outlet. $\overline{T}_{ss,o}$ is determined as

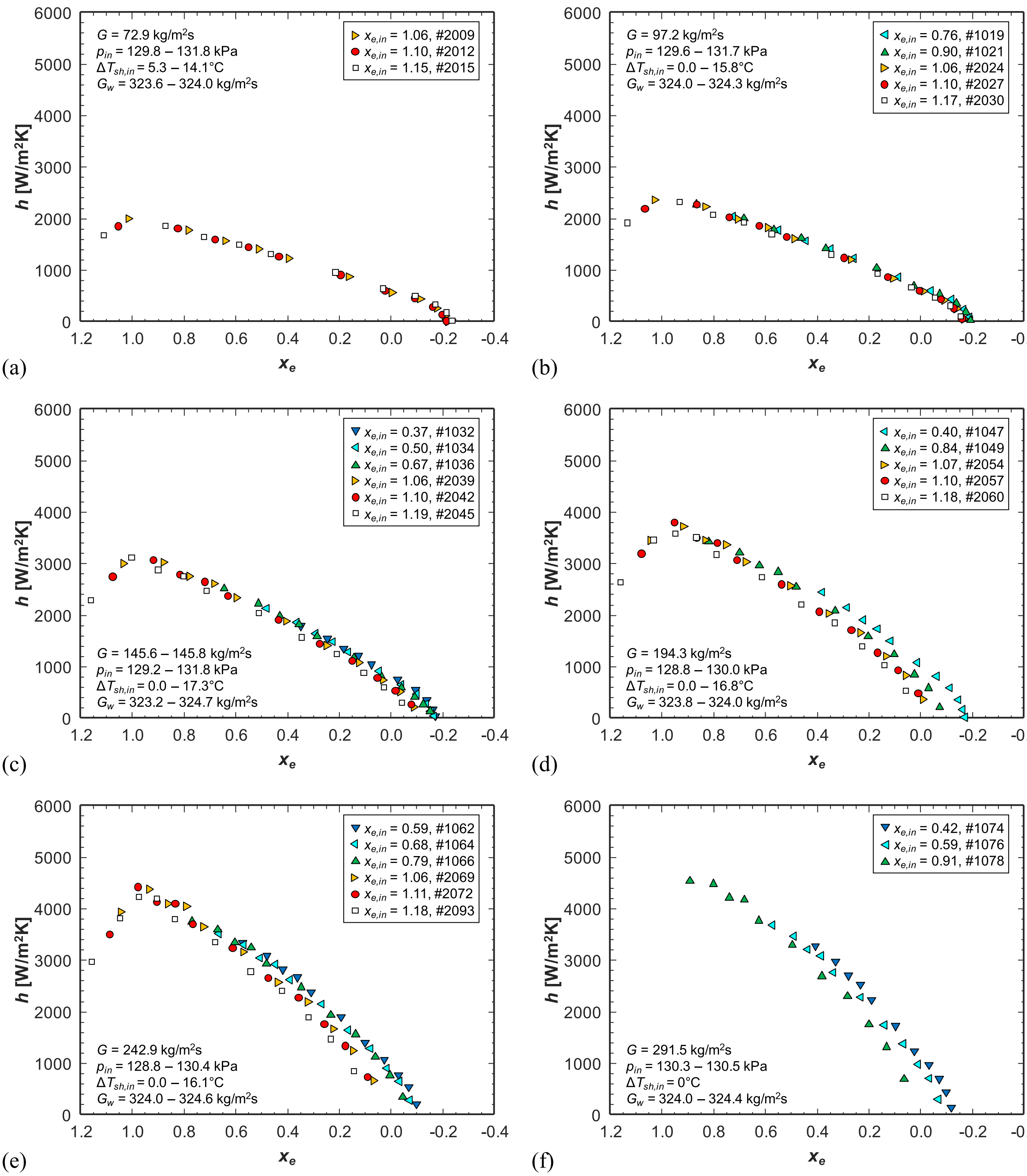

Fig. 15. Plots depicting variations in heat transfer coefficient, h, with respect to thermodynamic equilibrium quality, x_e, at different inlet thermodynamic equilibrium quality, $x_{e,in}$, for nPFH mass velocities of (a) $G \approx 73$ kg/m^{2}s, (b) $G \approx 97$ kg/m^{2}s, (c) $G \approx 146$ kg/m^{2}s, (d) $G \approx 194$ kg/m^{2}s, (e) $G \approx 243$ kg/m^{2}s, and (f) $G \approx 292$ kg/m^{2}s. Cases are shown for an inlet pressure of $p_{in} \approx 130$ kPa and water mass velocity of $G_w \approx 324$ kg/m^{2}s.

$$\overline{T}_{ss,o} = \frac{1}{L}\int_0^L T_{ss,o}(z)dz = \frac{\sum_{j=1}^{n} T_{ss,o,j}\Delta z_j}{\sum_{j=1}^{n}\Delta z_j}. \tag{14}$$

The relatively large temperature difference between $T_{w,in}$ and $T_{w,out}$ results in a lower maximum uncertainty of 12.4%. Fig. 18 presents a comparison between $\overline{h}$, calculated using finite differences and presented in Fig. 17, and $\overline{h}_{qw}$, calculated using q_w and $\overline{T}_{ss,o}$. Overall, $\overline{h}_{qw}$ is consistently less than $\overline{h}$, due to the slightly lower temperature of the outer wall of the tube. The Mean Absolute Error (MAE), between the two average heat transfer coefficients, calculated as

$$MAE(\%) = \frac{1}{N}\sum\left|\frac{\overline{h}_{qw} - \overline{h}}{\overline{h}}\right| \times 100\%, \tag{15}$$

is 12.0%. The purpose of this comparison is two-fold. (1) It reinforces the certainty that $\overline{h}$ can be discussed with, and (2) it confirms $\overline{h}$ can relate

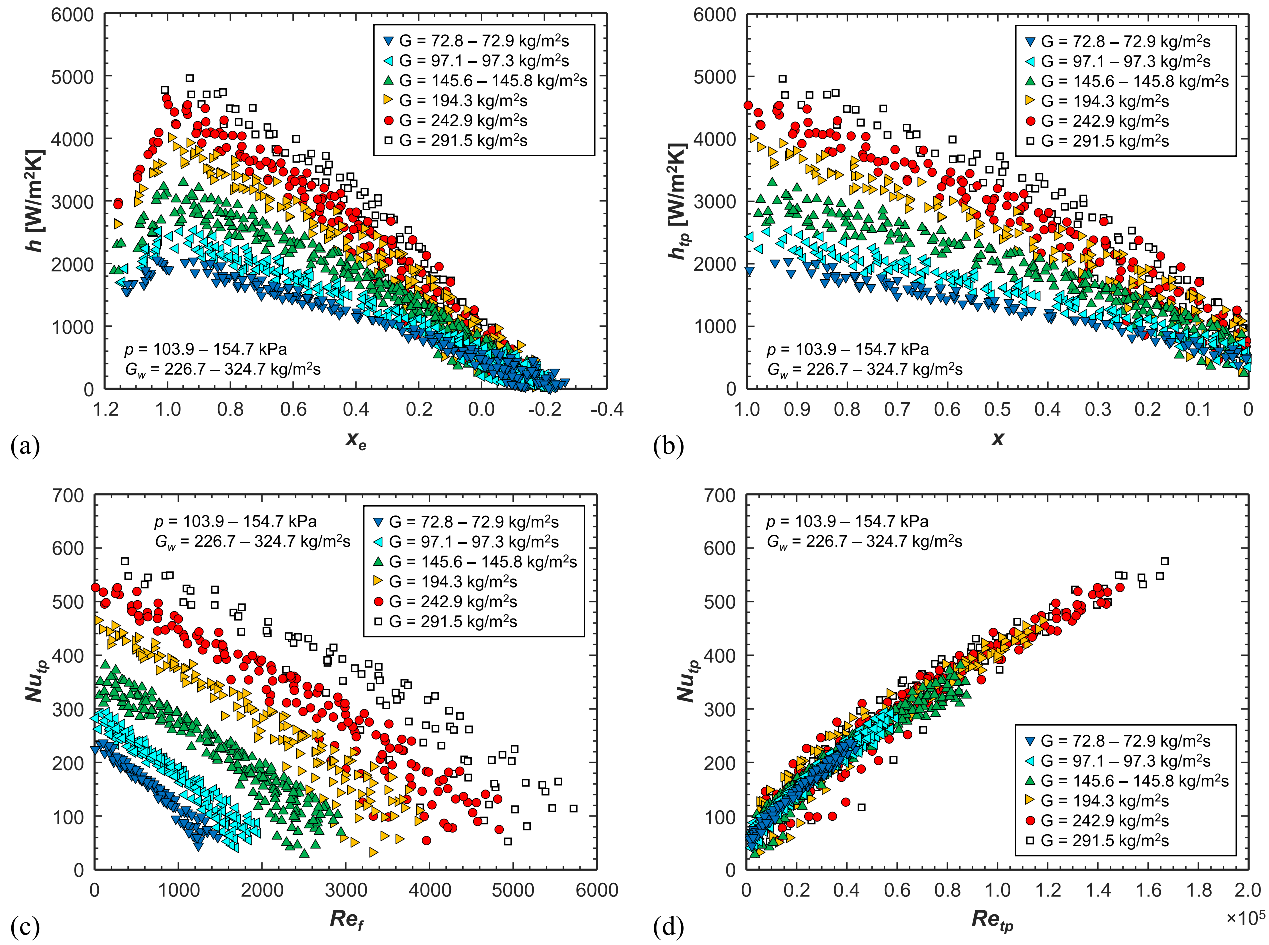

Fig. 16. Plots depicting variations of (a) heat transfer coefficient, h, with respect to thermodynamic equilibrium quality, x_e, for the entire water mass velocity, G_w, independent subset of the database, and, for the saturated portion of the subset, $0 \leq x_e \leq 1$, (b) h_{tp} with respect to quality, x, (c) Nusselt number in the saturated region, Nu_{tp}, with respect to liquid Reynold's number, Re_f, and (d) Nu_{tp} with respect to two-phase mixture Reynold's number, Re_{tp}.

average wall temperature to total heat transfer, which could be useful in a system level analysis.

Fig. 19 presents an overlay of $\overline{h}_{tp}$ in μg_e from the present study with that obtained by O'Neill et al. [24] in g_e at different orientations. At the intermediate flow rates between ~150 kg/m^{2}s and ~200 kg/m^{2}s, the μg_e data aligns with that obtained during horizontal flow and vertical downflow in g_e. The inertia of the flow and interfacial shear acting on the liquid film is sufficient to prevent significant deviations between μg_e and g_e during vertical downflow and horizontal flow. At lower flow rates, the μg_e data agrees well with the vertical downflow data, where symmetric flow patterns are expected in both cases, resulting in similar $\overline{h}_{tp}$. However, $\overline{h}_{tp}$ is noticeably greater during horizontal flow than vertical down flow and μg_e at $x_{e,in}$ of ~0.8. During saturated inlet conditions, the greater quantity of liquid within the channel and the influence of g_e produces an asymmetric liquid film during horizontal flow as liquid drains to the bottom of the tube. The thin liquid film along the top of the channel promotes highly efficient heat transfer and enhances $\overline{h}_{tp}$. The effect of gravity is less pronounced with superheated inlet conditions where the condensate film is thinner and more susceptible to shear from the high speed vapor core, resulting in similar $\overline{h}_{tp}$ in g_e and μg_e. At high G, $\overline{h}_{tp}$ in μg_e is generally lower than that in g_e, but this is assumed to be caused by the lower G_w available on the ISS compared to ground tests and not the influence of body force. The agreement between μg_e and g_e at intermediate G and horizontal and vertical downflow at high G, demonstrate the ability of interfacial shear and inertia to mitigate the influence of body force. Gravity is expected to become more influential as G is further decreased, as observed at low G with saturated inlet conditions.

The agreement between $\overline{h}_{tp}$ in μg_e and g_e during vertical downflow suggest that the conventional understanding of heat transfer mechanisms for annular condensation in g_e is applicable in μg_e. For thin liquid films, expected at high G and x, conduction across the condensate film is the dominant mechanism of heat transfer. As the liquid film thickens, conduction becomes less efficient, and convection becomes more influential, resulting in reduced heat transfer downstream, as observed in Fig. 16. However, condensation heat transfer is strongly correlated with the flow pattern, and flow visualization is required to define the primary mechanism of heat transfer during condensation in μg_e.

4. Assessment of heat transfer coefficient predictions

4.1. Correlation assessment

The agreement between $\overline{h}_{tp}$ in μg_e and in g_e suggests correlations developed with g_e data should be capable of predicting $\overline{h}_{tp}$ in μg_e. Table 2 presents h_{tp} correlations developed and validated from consolidated flow condensation databases. These correlations are selected for their applicability to a large number of fluids, operating conditions, and channel geometries. Accompanying each correlation are remarks regarding the database used to develop or validate the correlation, and the corresponding MAE of the present database, which is calculated as

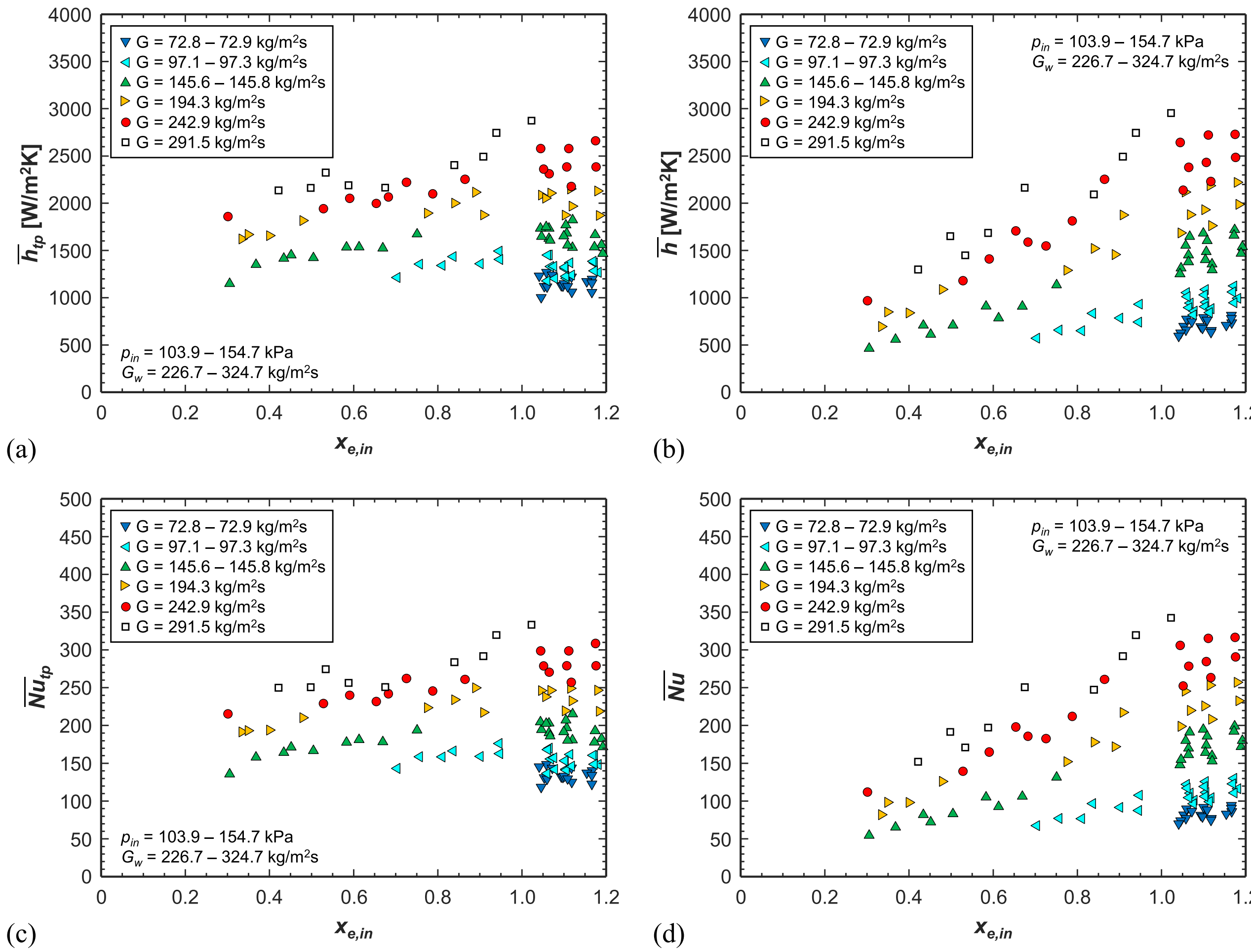

Fig. 17. Plots depicting variations of average heat transfer coefficient over (a) the saturated two-phase length, $\bar{h}_{tp}$, and (b) the entire channel, $\bar{h}$, and the corresponding Nusselt number averaged over the (c) the saturated two-phase length, $\overline{Nu}_{tp}$, and (d) the entire channel, $\overline{Nu}$, with respect to inlet thermodynamic equilibrium quality, $x_{e,in}$.

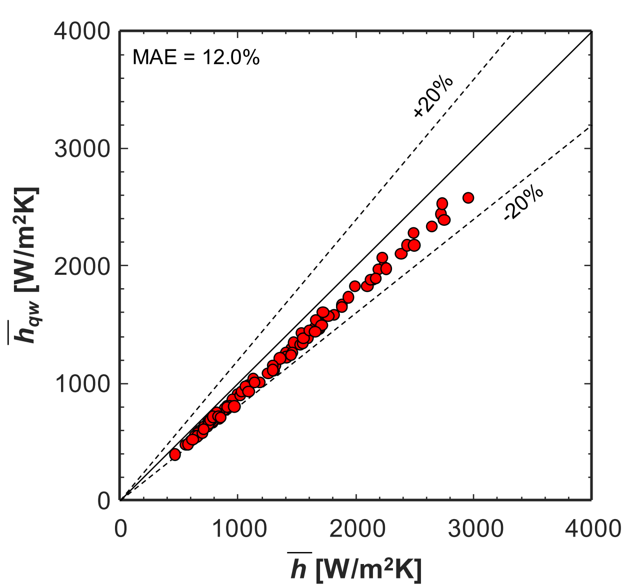

Fig. 18. Plots comparing channel averaged heat transfer coefficient, $\bar{h}$, calculated using finite differences and a pseudo average heat transfer coefficient calculated with net heat transfer across CM-HT, $\bar{h}_{qw}$.

$$MAE(\%) = \frac{1}{N}\sum\left|\frac{\bar{h}_{tp,pred} - \bar{h}_{tp,exp}}{\bar{h}_{tp,exp}}\right| \times 100\%. \tag{16}$$

Kim and Mudawar [46] consolidated a h_{tp} database for condensation in mini- and micro-channels. Criteria based on a modified Weber number, We^*, and Lockhart-Martinelli parameter, X, was proposed to divide the database into annular and slug flow regimes, with a correlation developed for each. Their correlation excludes the effects body force due to the dominating role of surface tension and viscosity in mini- and micro-channels. However, D_i of the present test section is greater than that used to validate their correlation, and the flow physics captured by their mini-/micro-channel database may not resemble that of the present database, resulting in a MAE of 27.2%.

A simple correlation was proposed by Dorao and Fernandino [47] that resembles that used for single-phase h but relies on Re_{tp} and Pr_{tp}. Their model was developed from a consolidated database including a wide range of diameters $D = 0.067 - 20.0$ mm. The authors identified two trends, one for $G \geq 200$ kg/m^{2}s and the other for $G < 200$ kg/m^{2}s. Their correlation was developed to capture and provide a sharp transition between the two regimes. The present μg_e database is predicted with exceptional accuracy of MAE = 7.1%. This is due to its dependence on Re_{tp}, which is strongly correlated to h_{tp} as shown in Fig. 14.

Hosseini et al. [48] utilized Genetic Programming to develop non-linear functions for h_{tp} that capture trends in their consolidated database. Following the observations of Dorao and Fernandino [47], two correlations were developed, one for $G \geq 200$ kg/m^{2}s and the other for G

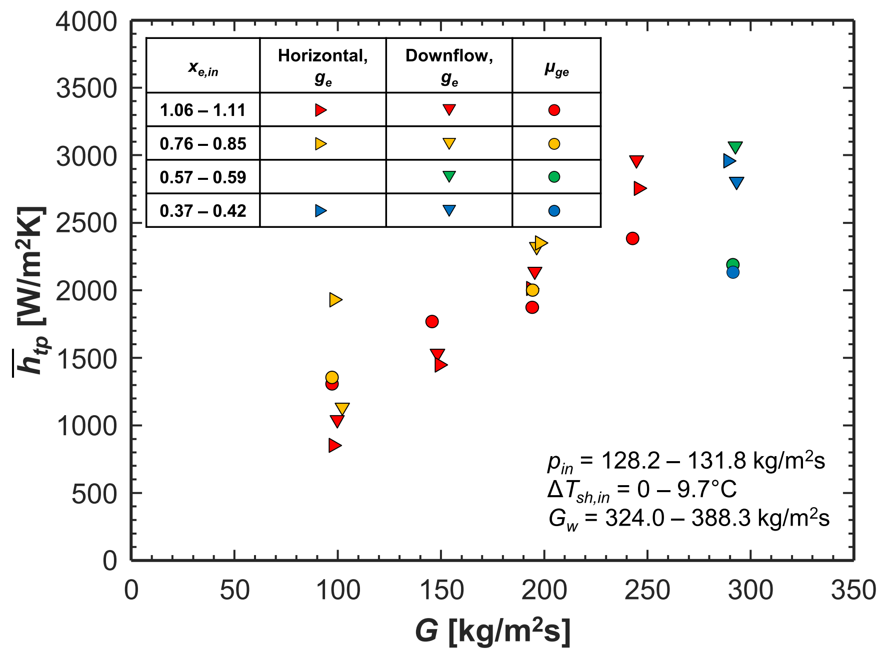

Fig. 19. Plot comparing variations of heat transfer coefficient averaged of the saturated two-phase length, $\bar{h}_{tp}$ with respect to mass velocity, G, in microgravity, μg_e, and Earth gravity, g_e, at different orientations [24].

< 200 kg/m^{2}s. The authors determined h_{tp} could be characterized by 6 dimensionless groups, Re_{tp}, Pr_{tp}, p_r, We_{go}, Fr_{fo}, and $(\rho_f - \rho_g)/\rho_f$, which were used to build their correlations. Their correlations predict the present database with a MAE of 45.0%.

Shah [49] updated a previous correlation by the same author [50] to enhance predictions at high x. The correlation considers 3 regimes. Regime I describes annular, mist, and intermittent flow, regime II captures wavy-stratified flow, and regime III includes stratified flow. Numerical criteria based on various dimensionless groups is provided to determine the appropriate regime. However, the present μg_e database exclusively falls in regime I. The correlation provides reasonable predictions and results in a MAE of 26.1%.

Similar to previous authors, Nie et al. [51] observed distinct differences between annular and non-annular flows. The authors proposed a simple correlation, demarcated by a dimensionless velocity, accounting for the convection effects in annular flows and body force induced spatial effects of non-annular flows. The present μg_e database is predicted with a MAE of 30.3 % by the annular, gravity independent, portion of the correlation.

The authors have also included the correlations by Moradkhani et al. [52] and Marinheiro et al. [53], which were developed from even larger consolidated databases than the aforementioned correlations, 11128 and 12017 data points, respectively. However, these correlations are not applicable for the μg_e database and result in an undefined MAE and a MAE of 100%, respectively. This is caused by the functional forms' dependence on g. While it is clear that the correlations were not intended to predict h_{tp} in μg_e, it does highlight the special consideration required before relying on g_e derived correlations for μg_e predictions. However, some correlations developed from g_e data, such as that by Dorao and Fernandino [47], either separate or neglect the effect of g and are capable of predicting $\bar{h}_{tp}$ for the μg_e database.

4.2. Separated flow model for annular flow condensation

Kim and Mudawar [54] developed a theoretical control volume based Separated Flow Model (SFM) to predict h_{tp} for a condensing annular flow in a parallel micro-channel heat sink with three cooling walls. The SFM was adapted for a single uniformly cooled circular channel at different orientations [24] and is employed to predict h_{tp} in μg_e by setting $g = 0$. The model describes the mass transfer from a vapor core to an annular liquid film that grows along the length of the channel. Key equations derived from conservations of mass, momentum, and energy are solved numerically using a finite difference scheme. The suppression of turbulent eddies at the interface of the liquid film is accounted for by an eddy momentum diffusivity model developed for shear-driven films [55]. h_{tp} is extracted by utilizing the eddy momentum diffusivity profile with the turbulent Prandtl number to determine the temperature gradient within the liquid film. A summary of the equations used in the SFM are provided in Table 3, and details regarding its derivation and procedure are available in [54].

Results of the SFM are presented in Fig. 20. An example of the variations in predicted h_{tp} along the channel compared to the experimental h_{tp} are shown in Fig. 20(a). The annular flow model consistently underpredicts h_{tp} at all x, but accurately captures the trend of h_{tp} decreasing at a near linear rate with x. The only exception is close to $x = 1$, where the model predicts a sharp decline in h_{tp} as the liquid film initially develops. However, as condensation proceeds, the predicted trend aligns with the experimental results. Fig. 20(b) and 20(c) present parametric trends of predicted and experimental $\bar{h}_{tp}$ with respect to G and $x_{e,in}$, respectively. The SFM accurately captures the trends of $\bar{h}_{tp}$ increasing with G and $x_{e,in}$, but underpredicts experimental results, as observed for the h_{tp} in Fig. 20(a). The predictions for $x_{e,in} > 1$ yield nearly constant $\bar{h}_{tp}$. However, the model is only valid in the saturated two-phase region, and increasing the upstream superheated length only shifts the starting point further downstream. The predicted h_{tp} for corresponding x_e and G remains constant, as observed in experimental data in Fig. 15. Fig. 20(d) presents a parity plot of the predicted and experimental $\bar{h}_{tp}$. As expected from the Fig. 20(a–c), the SFM underpredicts the database. Overall, the annular flow model predicts the database well with a MAE of 32.3%, performing comparably to most of the correlations presented in Section 4.1.

5. Conclusions

This study investigated flow condensation heat transfer in μg_e through experiments conducted onboard the International Space

Table 2
Evaluated condensation heat transfer correlations developed from consolidated databases.

Authors	Correlation	Remarks	MAE
Kim and Mudawar (2013) [46]	$We^{*} = \begin{cases} \dfrac{2.45\mathrm{Re}_g^{0.64}}{Su_{go}^{0.3}\left(1+1.09X_{tt}^{0.039}\right)^{0.4}} & \mathrm{Re}_f \le 1250 \\ \dfrac{0.85\mathrm{Re}_g^{0.79}X_{tt}^{0.157}}{Su_{go}^{0.3}\left(1+1.09X_{tt}^{0.039}\right)^{0.4}}\left[\left(\dfrac{\mu_g}{\mu_f}\right)^2\left(\dfrac{\nu_g}{\nu_f}\right)\right]^{0.084} & \mathrm{Re}_f > 1250 \end{cases}$ (17) $h_{tp} = \begin{cases} \dfrac{k_f}{D_h}\left[0.048\mathrm{Re}_f^{0.69}\mathrm{Pr}_f^{0.34}\dfrac{\phi_g}{X_{tt}}\right] & We^{*} > 7X_{tt}^{0.2} \\ \dfrac{k_f}{D_h}\left[\left(0.048\mathrm{Re}_f^{0.69}\mathrm{Pr}_f^{0.34}\dfrac{\phi_g}{X_{tt}}\right)^2 + \left(3.2\times10^{-7}\mathrm{Re}_f^{-0.38}Su_{go}^{1.39}\right)^2\right]^{0.5} & We^{*} < 7X_{tt}^{0.2} \end{cases}$ (18) where $X_{tt} = \left(\dfrac{\mu_f}{\mu_g}\right)^{0.1}\left(\dfrac{1-x}{x}\right)^{0.9}\left(\dfrac{\rho_g}{\rho_f}\right)^{1/2}$ (19) $\phi_g^2 = 1 + CX + X^2$ (20) $X^2 = \dfrac{(dp/dz)_f}{(dp/dz)_g}$ (21) $-\left(\dfrac{dp}{dz}\right)_f = \dfrac{2f_f G^2(1-x)^2}{\rho_f D_h}$ (22) $-\left(\dfrac{dp}{dz}\right)_g = \dfrac{2f_g G^2 x^2}{\rho_g D_h}$ (23) $f_k = \begin{cases} 16/\mathrm{Re}_k & \mathrm{Re}_k < 2000 \\ 0.079\mathrm{Re}_k^{-0.25} & 2000 \le \mathrm{Re}_k < 20000 \\ 0.046\mathrm{Re}_k^{-0.2} & \mathrm{Re}_k \ge 20000 \end{cases}$ (24) For Laminar flow in a rectangular channel ($\beta < 1$) $f_k\mathrm{Re}_k = 24\left(1 - 1.3553\beta + 1.9467\beta^2 - 1.7012\beta^3 + 0.9564\beta^4 - 0.2537\beta^5\right)$ (25) $C = \begin{cases} 0.39\mathrm{Re}_{fo}^{0.03}Su_{go}^{0.10}\left(\dfrac{\rho_f}{\rho_g}\right)^{0.35} & \mathrm{Re}_f \ge 2000, \mathrm{Re}_g \ge 2000 \\ 8.7\times10^{-4}\mathrm{Re}_{fo}^{0.17}Su_{go}^{0.50}\left(\dfrac{\rho_f}{\rho_g}\right)^{0.14} & \mathrm{Re}_f \ge 2000, \mathrm{Re}_g < 2000 \\ 0.0015\mathrm{Re}_{fo}^{0.59}Su_{go}^{0.19}\left(\dfrac{\rho_f}{\rho_g}\right)^{0.36} & \mathrm{Re}_f < 2000, \mathrm{Re}_g \ge 2000 \\ 3.5\times10^{-5}\mathrm{Re}_{fo}^{0.44}Su_{go}^{0.50}\left(\dfrac{\rho_f}{\rho_g}\right)^{0.48} & \mathrm{Re}_f < 2000, \mathrm{Re}_g < 2000 \end{cases}$ (26)	• Developed from consolidated database of 4045 datapoints • 17 fluids (CO_2, FC-72, hydro-carbons, and refrigerants) • Single- and multi-channels • Circular or rectangular channels • $D_h = 0.424 – 6.22$ mm • $G = 53 – 1403$ kg/m^{2}s • $x = 0 – 1$ • $p_r = 0.04 – 0.91$	27.2%
Dorao and Fernandino (2018) [47]	$h_{tp} = \dfrac{k_f}{D}\left[\left(0.023\mathrm{Re}_{tp}^{0.8}\mathrm{Pr}_{tp}^{0.3}\right)^9 + \left(41.5D^{0.6}\mathrm{Re}_{tp}^{0.4}\mathrm{Pr}_{tp}^{0.3}\right)^9\right]^{1/9}$ (27)	• Developed from consolidated database of 3937 data points • 19 fluids (CO_2, hydrocarbons, refrigerants, and water) • Single- and multi-channel • Circular, rectangular, triangular, semi-circular, Bar-rel, W-shape, and N-shaped channels • $D_h = 0.67 – 20.00$ mm • $G = 45.5 – 1360.0$ kg/m^{2}s • $x = 0 – 1$ • $T_{sat} =$ -132.3 – 115°C	7.1%
Hosseini *et al.* (2020) [48]	If $G \le 200$ kg/m^{2}s $h_{tp} = \dfrac{k_f}{D_h}\left[0.0022\mathrm{Re}_{tp}\left(\dfrac{\rho_f-\rho_g}{\rho_f}\right) + 0.0342We_{go}\left(\dfrac{\rho_f-\rho_g}{\rho_f}\right)^2 + \dfrac{\sin(39.8963p_r) - \ln(We_{go})}{-0.0298 - 0.2203Fr_{fo}} - \mathrm{Pr}_{tp}\right]$ (28) Elseif $G >$200 kg/m^{2}s $h_{tp} = \dfrac{k_f}{D_h}\left[\begin{array}{l} \vert 0.0169\mathrm{Re}_{tp}^{0.862} - 0.00146\dfrac{\mathrm{Re}_{tp}M}{\mathrm{Pr}_{tp}\left(\dfrac{\rho_f-\rho_g}{\rho_f}\right)} + 17.9480\sin(M) + \tan\left(27.637\left(\dfrac{\rho_f-\rho_g}{\rho_f}\right)\right)\vert\ldots \\ -\tan(369.8572 + \sin(M)) \end{array}\right]$ (29) $M = \dfrac{0.0036 + 0.0171 * We_{go}}{Fr_{fo}}$ (30)	• Validated for consolidated database of 6521 data points • 32 fluids (CO2, refrigerants, water) • Single channels • Circular and square channels • D = 0.133 – 20.8 mm • G = 13.1 – 1200 kg/m2s • x = 0.001 – 0.99 • pr = 0.0005 – 0.952	44.0%
Moradkhani *et al.* (2022) [52]	$h_{tp} = \dfrac{k_f}{D}\left[c_1 x^{c_2} Bd^{c_3} p_r^{c_4}\mathrm{Pr}_{tp}^{c_5}\mathrm{Re}_{tp}^{c_6}\left(\dfrac{\rho_f-\rho_g}{\rho_f}\right)^{c_7} We_{go}^{c_8} Fr_{fo}^{c_9}\right]$ (31) If $Bd < 0.5$ $c_1 = 1.9\times10^{-6}$, $c_2 =$ -0.169, $c_3 =$ -5.29, $c_4 = 5.735$, $c_5 = 0.069$, $c_6 = 1.07$, $c_7 =$ -2.776, $c_8 = 4.788$, $c_9 =$ -4.91 If $0.5 \le Bd < 3.0$ $c_1 = 9.88$, $c_2 = 0.205$, $c_3 = 0.97$, $c_4 =$ -1.04, $c_5 =$ -0.182, $c_6 = 0.283$, $c_7 = 5.169$, $c_8 =$ -0.671, $c_9 = 0.781$ If $Bd \ge 3.0$ $c_1 = 2.453$, $c_2 = 0.151$, $c_3 = 0.63$, $c_4 =$ -0.50, $c_5 =$ -0.10, $c_6 = 0.283$, $c_7 = 1.753$, $c_8 =$ -0.215, $c_9 = 0.379$	• Consolidated database of 11128 data points • 37 different fluids (refrigerants) • Single- and multi-channels • Circular, rectangular, triangular, barrel, N-shape channels • $D = 0.0667 – 20.8$ mm • $G = 13.1 –1580$ kg/m^{2}s • $p_r = 0 – 1$	–%

(*continued on next page*)

Table 2 (*continued*)

Authors	Correlation	Remarks	MAE
Shah (2022) [49]	$J_g = \frac{xG}{(gD\rho_g(\rho_f-\rho_g))^{0.5}}$ (32) $Z_{Shah} = \left(\frac{1}{x}-1\right)^{0.8} p_r^{0.4}$ (33) $h_{Nu} = 1.32 * \mathrm{Re}_f^{-1/3}\left[\frac{\rho_f(\rho_f-\rho_g)gk_f^3}{\mu_f^2}\right]^{1/3}$ (34) For vertical downflow, or horizontal flow with $D_h > 6$mm $h_1 = 0.023\mathrm{Re}_f^{0.8}\mathrm{Pr}_f^{0.4}\frac{k_f}{D_i}\left(1+\frac{3.8}{Z_{Shah}^{0.95}}\right)\left(\frac{\mu_f}{14\mu_g}\right)^{0.0058+0.557p_r}$ (35) For horizontal flow with $D_h \le 6$mm $h_1 = 0.023\mathrm{Re}_{fo}^{0.8}\mathrm{Pr}_f^{0.4}\frac{k_f}{D_i}\left[1+1.128x^{0.817}\left(\frac{\rho_f}{\rho_g}\right)^{0.3685}\left(\frac{\mu_f}{\mu_g}\right)^{0.2363}\left(1-\frac{\mu_g}{\mu_f}\right)^{2.144}\mathrm{Pr}_f^{-0.1}\right]$ (36) Vertical downflow If $J_g \ge \frac{1}{2.4Z_{Shah}+0.73}$ or $x \ge 0.99$ $h_{tp} = h_1$ Elseif $J_g \le 0.89 - 0.93\exp(-0.87Z_{Shah}^{-1.17})$, or $Re_{fo} < 600$ and $We_{go} < 100$ $h_{tp} = h_{Nu}$ Else $h_{tp} = h_1 + h_{Nu}$ Horizontal flow For hydrocarbons or any other fluid with $Re_{fo} < 100$ If $J_g \ge 0.98(Z_{Shah}+0.263)^{-0.62}$ or $x \ge 0.99$ $h_{tp} = h_1$ Elseif $J_g \le 0.95(1.254+2.27Z_{Shah}^{1.249})^{-1}$ $h_{tp} = h_{Nu}$ Else $h_{tp} = h_1 + h_{Nu}$ For any fluid other than hydrocarbons with $Re_{fo} \ge 100$ If $We_{go} > 100$ and $Fr_{fo} > 0.026$ and $J_g \ge 0.98(Z_{Shah}+0.263)^{-0.62}$, or x ≥ 0.99 $h_{tp} = h_1$ Elseif $Fr_{fo} > 0.026$ and $J_g \le 0.95(1.254+2.27Z_{Shah}^{1.249})^{-1}$ $h_{tp} = h_{Nu}$ Else $h_{tp} = h_1 + h_{Nu}$ Where Re_{fo} and Re_f are calculated with $D = D_e$, and J_g, We_{go}, and Fr_{fo} are calculated with $D = D_h$	• Developed from consolidated database of 8492 data points • 51 fluids (chemicals, cryogens, hydrocarbons, refrigerants, and water) • Single- and multi-channels • Circular, rectangular, triangular, and annular channels • $D = 0.08 – 49.0$ mm • $G = 1.1 – 1400$ kg/m^{2}s • $p_r = 0.0006 – 0.949$	26.1%
Nie *et al.* (2023) [51]	$J_g = \frac{xG}{[gD\rho_g(\rho_f-\rho_g)]^{0.5}}$ (37) $\phi_g = X_{tt}^{0.2} + 0.83X_{tt}^{1.2}\left(\frac{x}{J_g}\right)^{0.84}$ (38) $G_{tran} = \rho_f(gD)^{0.5}\left(0.54 - 0.96/Bd^2 - 4.2/Bd\right)$ (39) $h_A = 0.038\mathrm{Re}_f^{0.72}\mathrm{Pr}_f^{0.27}\left(\frac{\mu_f}{\mu_g}\right)^{0.84}\left(\frac{\rho_g}{\rho_f}\right)^{0.37}\frac{\phi_g}{X_{tt}}\frac{k_f}{D}$ (40) $h_{tp} = \begin{cases} h_A & J_g \ge 2.5 \text{and} G > G_{tran} \\ h_A + 0.012\mathrm{Re}_f^{0.85}\left(\frac{x}{1-x}\right)^{1.1}\left(\frac{\rho_f}{\rho_g}\right)^{0.55}\left(\frac{\rho_f-\rho_g}{Fr_g\rho_g}\right)\frac{k_f}{D} & J_g < 2.5 \text{or} G \le G_{tran} \end{cases}$ (41)	• Developed from consolidated database of 6064 data points • 28 fluids (ammonia, CO2, hydrocarbons, nitrogen, refrigerants) • Single channels • Circular channels • $D = 0.49 – 8.92$ mm • $G = 13 – 1200$ kg/m^{2}s • $x = 0 – 1$, • $p_r = 0.03 – 0.95$	30.3%
Marinheiro *et al.* (2024) [53]	$h_{tp} = 0.055\mathrm{Re}_{tp}^{0.732}\mathrm{Pr}_{tp}^{0.269}Fr_{fo}^{-0.091}\frac{k_f}{D}$ (42)	• Developed from consolidated database of 12017 data points • 69 fluids (Ammonia, hydrocarbons, nitrogen, refrigerants, and water) • Single- and multi-channels • Circular, rectangular, triangular, semi-circular, and flattened channels • $D = 0.0667 – 20.8$ mm • $G = 13.1 – 1400$ kg/m^{2}s • $x = 0.00024 – 0.999$ • $p_r = 0.0313 – 0.998$	100%

Station, as part of the Flow Boiling and Condensation Experiment. The working fluid, nPFH, condensed within a stainless steel tube and rejected heat to a countercurrent flow of water surrounding the tube. A wide range of operating conditions were tested, and the subset of the database exhibiting heat transfer independent of the water mass velocity was used to assess experimental trends, various correlations, and a Separated Flow Model. Key conclusions are as follows:

(i) Condensation of nPFH was independent of G_w for $G \le 150$ kg/m^{2}s with $G_w \ge 226$ kg/m^{2}s, and for $G > 150$ kg/m^{2}s only $G_w \ge 323$ kg/m^{2}s. Results in this regime resulted in negligible deviations in h and q_w with respect to G_w.

(ii) h is strongly dependent on G and local x_e, but weakly dependent on p_{in}. h is greatest upstream, where the liquid film is the thin, and peaks near $x_e = 1$. h decreases along the channel as condensation persists, the liquid film grows, and x_e decreases. h increased with

Table 3
Summary of equations used in the Separated Flow Model for annular condensation.

Geometric definitions

$$P_i = \pi D_i \quad (43)$$

$$P_{f,y} = \pi(D_i - 2y) \quad (44)$$

$$P_{\text{int}} = \pi(D_i - 2\delta) \quad (45)$$

$$A_{f,*} = \frac{\pi}{4}(D_i - 2y)^2 - \frac{\pi}{4}(D_i - 2\delta)^2 \quad (46)$$

Mass conservation

$$\frac{d\dot{m}_f}{dz} - \Gamma_{fg} = 0 \quad (47)$$

$$\frac{d\dot{m}_g}{dz} + \Gamma_{fg} = 0 \quad (48)$$

$$\dot{m}_f = \rho_f \int_0^\delta u_f \pi(D_i - 2y) dy \quad (49)$$

$$\dot{m}_g = \rho_g \bar{u}_g \pi(D_i - 2\delta)^2/4 \quad (50)$$

Energy conservation

$$\Gamma_{fg} = q'' P_i / h_{fg} \quad (51)$$

Momentum conservation for liquid film

$$\tau = \mu_f\left(1 + \frac{\varepsilon_m}{\upsilon_f}\right)\frac{du_f}{dy} = \left(-\frac{dp}{dz} - \rho_f g \sin\theta\right)\frac{A_{f,*}}{P_{f,y}} + \frac{\tau_{\text{int}} P_{\text{int}} + \Gamma_{fg} u_{\text{int}}}{P_{f,y}} \quad (52)$$

Velocity profile across film

$$u_f(y) = \frac{1}{\mu_f}\left(-\frac{dp}{dz} - \rho_f g \sin\theta\right)\int_0^\delta \frac{A_{f,*}}{P_{f,y}}\left(1 + \frac{\varepsilon_m}{\nu_f}\right)^{-1} dy + \frac{(\tau_{\text{int}} P_{\text{int}} + \Gamma_{fg} u_{\text{int}})}{\mu_f}\int_0^\delta \frac{1}{P_{f,y}}\left(1 + \frac{\varepsilon_m}{\nu_f}\right)^{-1} dy \quad (53)$$

$$u_{\text{int}} = u_f(\delta) = \frac{\left(-\frac{dp}{dz} - \rho_f g \sin\theta\right)\int_0^\delta \frac{A_{f,*}}{P_{f,y}}\left(1 + \frac{\varepsilon_m}{\nu_f}\right)^{-1} dy + \tau_{\text{int}} P_{\text{int}}\int_0^\delta \frac{1}{P_{f,y}}\left(1 + \frac{\varepsilon_m}{\nu_f}\right)^{-1} dy}{\mu_f - \Gamma_{fg}\int_0^\delta \frac{1}{P_{f,y}}\left(1 + \frac{\varepsilon_m}{\nu_f}\right)^{-1} dy} \quad (54)$$

Pressure gradient

$$-\frac{dp}{dz} = \rho_f g \sin\theta + \frac{\frac{\mu_f \dot{m}_f}{\rho_f} - (\tau_{\text{int}} P_{\text{int}} + \Gamma_{fg} u_{\text{int}})\int_0^\delta \left[P_{f,y}\int_0^y \frac{1}{P_{f,y}}\left(1 + \frac{\varepsilon_m}{\nu_f}\right)^{-1} dy\right] dy}{\int_0^\delta \left[P_{f,y}\int_0^y \frac{A_{f,*}}{P_{f,y}}\left(1 + \frac{\varepsilon_m}{\nu_f}\right)^{-1} dy\right] dy} \quad (55)$$

Momentum conservation for vapor core

$$\tau_{\text{int}} = \frac{1}{P_{f,\text{int}}}\left[A_g\left(-\frac{dp}{dz} + \rho_g g \sin\theta\right) - \frac{d\left(\rho_g \bar{u}_g^2 A_g\right)}{dz} - \Gamma_{fg} u_{\text{int}}\right] \quad (56)$$

Interfacial shear stress relations [56,57]

$$\tau_{\text{int}} = \frac{1}{2} f_{\text{int}} \rho_g (\bar{u}_g - u_i)^2 + \frac{(\bar{u}_g - u_{\text{int}})\Gamma_{fg}}{2P_{\text{int}}} \quad (57)$$

$$f_{\text{int}} = \begin{cases} 16/\text{Re}_c & \text{Re}_c < 2000 \\ 0.079\text{Re}_c^{-0.25} & 2000 \le \text{Re}_c < 20000 \\ 0.046\text{Re}_c^{-0.2} & \text{Re}_c \ge 20000 \end{cases} \quad (58)$$

$$\text{Re}_c = \frac{\rho_g (\bar{u}_g - u_{\text{int}})(D_i - 2\delta)}{\mu_g} \quad (59)$$

Turbulent Parameters [54,55]

$$\frac{\varepsilon_m}{\nu_f} = -0.5 + 0.5\sqrt{1 + 4K^2 y^{+2}\left[1 - \exp\left(-\sqrt{1 - \frac{y^+}{\delta^+}}\frac{y^+}{A^+}\right)\right]^2\left(1 - \frac{y^+}{\delta^+}\right)^{0.1}\frac{\tau}{\tau_{wall}}} \quad (60)$$

$$A^+ = 26\left(1 + 30.18\mu_f \rho_f^{-0.5} \tau_{wall}^{-1.5} \frac{dp}{dz}\right)^{-1} \quad (61)$$

$$K = 0.4 \quad (62)$$

$$\delta^+ = y^+(\delta) = \frac{\delta u^*}{\nu_f} \quad (63)$$

Heat transfer coefficient

$$h_{tp} = \frac{q''_w}{T_{sat} - T_{wall}} = \frac{\rho_f c_{p,f} u^*}{T_\delta^+} = \frac{\rho_f c_{p,f} u^*}{\int_0^{\delta^+} \frac{q''}{q''_{wall}}\left(\frac{1}{\text{Pr}_f} + \frac{1}{\text{Pr}_T}\frac{\varepsilon_m}{\nu_f}\right)^{-1} dy^+} = \frac{\rho_f c_{p,f} u^*}{\int_0^{\delta^+} \frac{D_i}{D_i - 2\delta}\left(\frac{1}{\text{Pr}_f} + \frac{1}{\text{Pr}_T}\frac{\varepsilon_m}{\nu_f}\right)^{-1} dy^+} \quad (64)$$

$$\text{Pr}_T = 1.4\exp\left(-15\frac{y^+}{\delta^+}\right) + 0.66 \quad (65)$$

G due to greater flow inertia and interfacial shear stress, which is assumed to thin the liquid film and enhance heat transfer. The effects of G and x_e are solely captured by Re_{tp}, which collapses the data along a single trend of Nu_{tp} increasing with Re_{tp}.

(iii) $\bar{h}_{tp}$ increases with G and $x_{e,in}$ until saturation, $x_e = 1$. Further increasing $x_{e,in}$ does not enhance $\bar{h}_{tp}$. However, $\bar{h}$ increases as inlet superheat is enhanced due to the inclusion of superheated condensation in the upstream region and the reduction of the subcooled length in the downstream region of the channel.

(iv) $\bar{h}_{tp}$ in μg_e agreed with ground data obtained in g_e during horizontal flow and vertical down flow, indicating that flow inertia was sufficient to provide gravity independent heat transfer.

(v) Various correlations developed from consolidated databases were assessed for their applicability to the μg_e database. The best performing correlation was that by Dorao and Fernandino [47] and predicted $\bar{h}_{tp}$ with a MAE of 7.1%. Their correlation neglected the effect of gravity and was dependent on Re_{tp}. However, some correlations were overly dependent on g and were unusable for the μg_e database.

(vi) A Separated Flow Model for annular flow was used to predict $\bar{h}_{tp}$ of the μg_e database. The model accurately captures h_{tp} decreasing with x_e and trends of $\bar{h}_{tp}$ increasing with G and $x_{e,in}$ until $x_{e,in} = 1$. However, the model underpredicts the database, and results in a MAE of 32.3%.

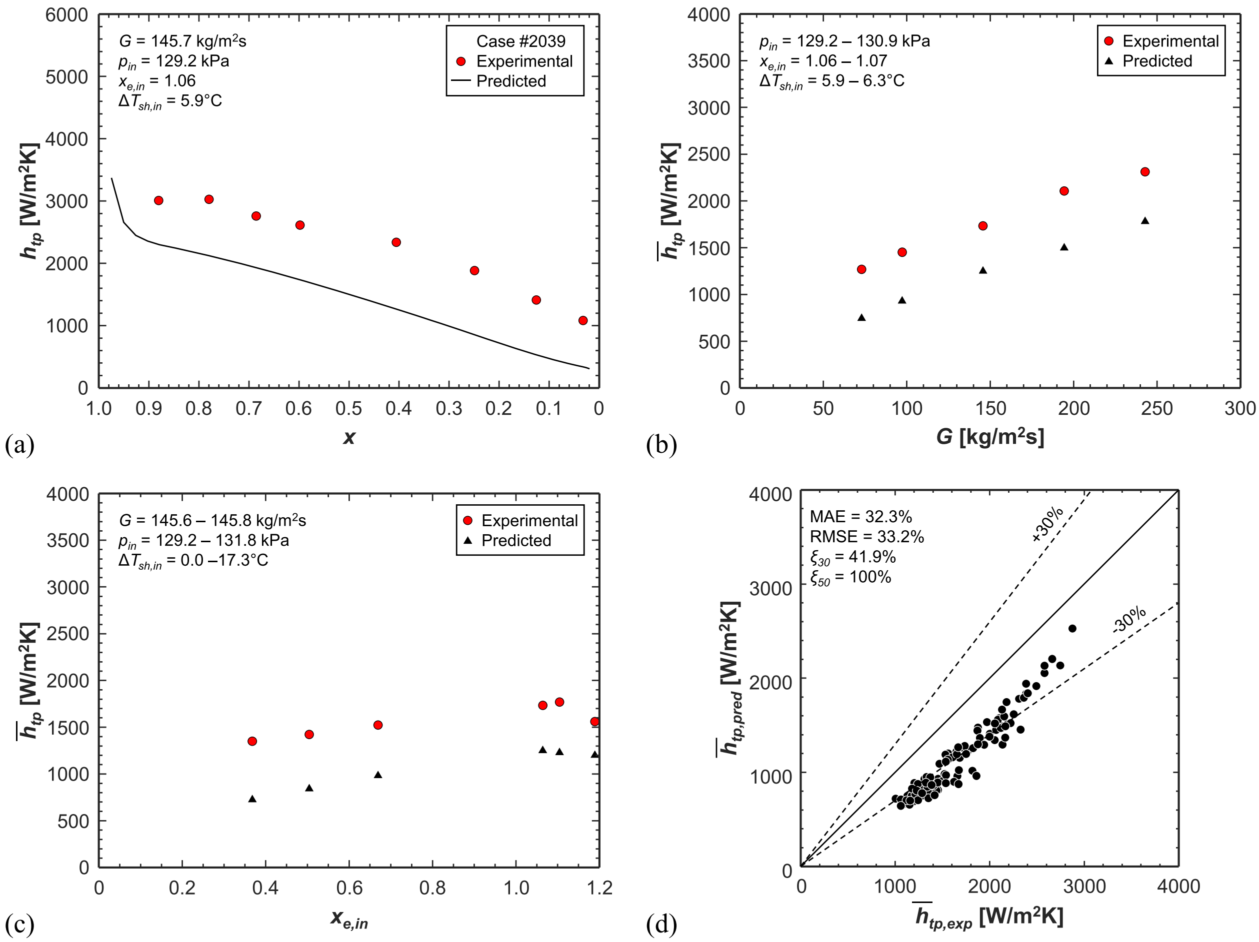

Fig. 20. Plots displaying various predictions of the Separated Flow Model compared to experimental results including (a) heat transfer coefficient along the the saturated two-phase length, h_{tp},with respect to quality, x, parametric trends of h_{tp} averaged over the two-phase length, $\overline{h}_{tp}$, with respect to (b) mass velocity, G, and (c) inlet thermodynamic equilibrium, $x_{e,in}$, and (d) a parity plot of predicted and experimental $\overline{h}_{tp}$.

Author declaration

We wish to confirm that there are no known conflicts of interest associated with this publication and there has been no significant financial support for this work that could have influenced its outcome.

We confirm that the manuscript has been read and approved by all named authors and that there are no other persons who satisfied the criteria for authorship but are not listed. We further confirm that the order of authors listed in the manuscript has been approved by all of us. We confirm that we have given due consideration to the protection of intellectual property associated with this work and that there are no impediments to publication, including the timing of publication, with respect to intellectual property. In so doing we confirm that we have followed the regulations of our institutions concerning intellectual property.

We understand that the Corresponding Author is the sole contact for the Editorial process (including Editorial Manager and direct communications with the office). He/she is responsible for communicating with the other authors about progress, submissions of revisions and final approval of proofs. We confirm that we have provided a current, correct email address which is accessible by the Corresponding Author and which has been configured to accept email from mudawar@ecn.purdue.edu

Signed by all authors as follows:
Issam Mudawar, 12/15/2024
Steven Darges, 12/15/2024
Mohammad Hasan, 12/15/2024
Henry Nahra, 12/15/2024
R. Balasubramaniam, 12/15/2024
Jeffrey Mackey, 12/15/2024

CRediT authorship contribution statement

Issam Mudawar: Writing – review & editing, Methodology, Supervision, Conceptualization, Funding acquisition, Formal analysis, Validation, Investigation, Data curation, Writing – original draft, Project administration. **Steven J. Darges:** Writing – original draft, Validation, Formal analysis, Data curation, Writing – review & editing, Investigation, Software, Conceptualization, Methodology. **Mohammad M. Hasan:** Funding acquisition, Data curation, Project administration, Methodology, Investigation, Conceptualization, Writing – review & editing, Supervision. **Henry K. Nahra:** Writing – review & editing, Supervision, Project administration, Methodology, Investigation, Funding acquisition, Data curation, Conceptualization. **R. Balasubramaniam:** Writing – review & editing, Validation, Investigation, Data curation, Conceptualization. **Jeffrey R. Mackey:** Writing – review & editing, Validation, Investigation, Data curation, Conceptualization.

Declaration of competing interest

The authors declare the following financial interests/personal relationships which may be considered as potential competing interests:

Issam Mudawar reports financial support was provided by NASA. Henry Nahra reports a relationship with NASA Glenn Research Center that includes: employment and funding grants. If there are other authors, they declare that they have no known competing financial interests or personal relationships that could have appeared to influence the work reported in this paper.

Acknowledgement

The authors are appreciative of the support of the National Aeronautics and Space Administration (NASA) under grant no. 80NSSC22K0328. The authors are also thankful to the FBCE personnel at NASA Glenn Research Center, Cleveland, Ohio, especially Nancy Hall (FBCE Project Manager), Rochelle May, Phillip Gonia, Jose Lombay-Gonzalez (Software Engineering), Mark Sorrells (Assembly, Integration and Test Lead), Jesse deFiebre (Fluids Lead), Monica Guzik (FBCE Chief Engineer), and ZIN FCF Mission Operations Team, for their dedicated technical assistance and successful completion of ISS testing.

Appendix A. ISS experiment summary

A summary of flow condensation experiments performed onboard the ISS is provided in Table A.1. To cross-reference the data reported in this study to the original database (which will be made available to the community via a NASA repository later), experiment reference numbers (Expt.#) are provided for each set of operating conditions, including mass velocity, G, inlet pressure, p_{in}, inlet thermodynamic equilibrium quality, $x_{e,in}$, and water mass velocity G_w. The naming convention for Expt.# is the final three digits of the number represents unique case numbers while the first digit represents the trial number. For example, Expt.# 3007 denotes the third trial of case 7. Select cases were performed with atypical setpoints to achieve the desired inlet conditions and are demarcated by a five digit reference number.

Table A.1
Summary of operating conditions obtained during microgravity flow condensation experiments performed onboard the ISS and their corresponding experiment reference number.

Experiment Reference Number (Expt.#)	G [kg/m^{2}s]	p_{in} [kPa]	$x_{e,in}$	G_w [kg/m^{2}s]
3007	72.9	129.9	1.05	129.6
2008	72.9	130.8	1.05	226.8
2009	72.9	130.9	1.06	323.6
2010	72.9	129.6	1.10	129.6
2011	72.9	131.7	1.09	226.8
2012	72.9	129.8	1.10	324.0
2013	72.9	131.0	1.18	129.6
2014	72.9	131.2	1.17	226.8
2015	72.9	131.8	1.15	324.0
1018	97.2	130.0	0.76	129.6
1019	97.2	131.7	0.76	324.0
1020	97.2	129.8	0.90	129.6
1021	97.2	129.7	0.90	324.0
2022	97.2	130.1	1.07	129.6
2023	97.2	129.6	1.07	226.7
2024	97.2	129.7	1.07	324.1

(continued on next page)

Table A.1 (*continued*)

Experiment Reference Number (Expt.#)	G [kg/m^{2}s]	p_{in} [kPa]	$x_{e,in}$	G_w [kg/m^{2}s]
2025	97.2	129.9	1.11	129.6
2026	97.2	129.7	1.11	226.8
2027	97.2	129.6	1.10	324.0
2028	97.2	129.9	1.18	129.6
2029	97.2	129.8	1.18	226.7
2030	97.2	129.9	1.17	324.3
1031	145.8	129.7	0.36	129.6
1032	145.6	129.6	0.37	324.0
1033	145.8	130.0	0.50	129.5
1034	145.8	131.8	0.50	324.1
1035	145.7	130.0	0.67	129.6
1036	145.7	131.6	0.67	323.2
2037	145.7	129.3	1.07	129.6
2038	145.7	129.6	1.06	226.8
2039	145.7	129.2	1.06	324.2
2040	145.7	130.1	1.10	129.6
2041	145.7	129.9	1.11	226.7
2042	145.7	130.0	1.10	324.7
2043	145.7	128.7	1.19	129.5
2044	145.7	129.7	1.19	226.8
2045	145.7	130.0	1.19	324.0
1046	194.3	129.8	0.39	129.6
1047	194.3	130.0	0.40	324.0
1048	194.3	130.0	0.84	129.6
1049	194.3	128.8	0.84	324.0
2052	194.3	130.8	1.06	129.6
2053	194.3	129.7	1.06	226.8
2054	194.3	129.9	1.07	324.0
2055	194.3	128.9	1.10	129.6
2056	194.3	129.6	1.10	226.8
2057	194.3	129.5	1.10	324.0
2058	194.3	128.9	1.19	129.6
2059	194.3	125.3	1.19	226.8
2060	194.3	129.4	1.18	323.8
1061	242.9	131.4	0.58	129.6
1062	242.9	128.8	0.59	324.6
1063	242.9	130.2	0.68	129.6
1064	242.9	129.8	0.68	324.0
1065	242.9	130.0	0.78	129.6
1066	242.9	130.0	0.79	324.0
2067	242.9	129.7	1.07	129.6
2068	242.9	129.9	1.06	226.7
2069	242.9	129.8	1.06	324.0
2070	242.9	129.8	1.12	129.6
2071	242.9	130.3	1.10	226.8
2072	242.9	130.4	1.11	324.0
1073	291.5	129.9	0.41	129.4
1074	291.5	130.4	0.42	323.9
1075	291.5	130.4	0.58	129.6
1076	291.5	130.5	0.59	324.4
1077	291.5	130.2	0.87	129.6
1078	291.5	130.3	0.91	324.0
2085	72.8	152.8	1.07	129.6
10086	72.9	153.0	1.05	226.8
10087	72.9	153.1	1.04	323.9
2088	72.8	153.2	1.12	129.6
2089	72.8	152.8	1.12	226.8
2090	72.9	153.3	1.12	324.0
2091	242.9	130.4	1.18	129.5
2092	243.0	129.8	1.17	226.7
2093	242.9	130.3	1.18	324.1
1094	97.2	152.2	0.70	129.6
1095	97.2	151.9	0.70	324.0
1096	97.2	153.0	0.81	129.6
1097	97.2	152.7	0.81	324.0
1098	97.2	153.2	0.94	129.6
1099	97.2	152.7	0.95	324.1
2100	97.2	152.8	1.08	129.6
2101	97.2	152.5	1.08	226.8
2102	97.2	152.7	1.08	324.0
2103	97.2	153.1	1.12	129.6
2104	97.2	152.8	1.12	226.8
2105	97.1	152.6	1.11	324.2
1109	145.8	152.5	0.30	129.6
1110	145.8	152.4	0.31	323.8

(continued on next page)

Table A.1 (*continued*)

Experiment Reference Number (Expt.#)	G [kg/m^{2}s]	p_{in} [kPa]	$x_{e,in}$	G_w [kg/m^{2}s]
1111	145.8	152.2	0.45	129.6
1112	145.8	152.0	0.45	324.1
1113	145.8	152.8	0.61	129.6
1114	145.8	152.3	0.61	324.0
10115	145.7	153.5	1.05	129.8
10116	145.7	153.1	1.05	226.9
10117	145.7	152.7	1.04	323.6
2118	145.7	154.8	1.12	129.6
2119	145.7	153.6	1.12	226.7
2120	145.7	153.2	1.12	323.8
1124	194.3	151.7	0.33	129.5
1125	194.3	153.0	0.33	324.0
1126	194.3	153.8	0.76	129.6
1127	194.3	152.5	0.78	324.0
1128	194.3	154.6	0.88	129.6
1129	194.3	153.6	0.89	324.1
10130	194.3	156.9	1.04	129.6
10131	194.3	153.6	1.05	226.8
10132	194.3	153.4	1.05	324.1
2133	194.3	157.9	1.11	129.6
2134	194.3	154.4	1.12	226.8
2135	194.3	153.7	1.12	324.3
1139	242.9	153.3	0.52	129.6
1140	242.9	153.0	0.53	324.1
1141	242.9	155.0	0.72	129.6
1142	242.9	153.1	0.73	324.0
2145	242.9	160.2	1.06	129.6
2146	242.9	156.4	1.06	226.6
10147	242.9	154.0	1.05	323.9
2148	242.9	159.1	1.11	129.6
2149	242.9	157.3	1.11	226.8
2150	242.9	154.7	1.12	324.1
1151	291.5	154.0	0.52	129.6
1152	291.5	153.5	0.53	324.0
1153	291.5	159.9	0.81	129.6
1154	291.5	154.3	0.84	324.1
3163	72.9	105.0	1.06	129.6
4164	72.9	104.7	1.06	226.8
3165	72.9	104.8	1.07	323.9
2166	72.9	105.1	1.11	129.6
2167	72.9	104.8	1.10	226.8
1168	72.8	104.8	1.11	324.2
2169	72.9	105.0	1.17	129.6
2170	72.9	104.9	1.17	226.8
2171	72.9	104.7	1.17	323.9
1174	97.2	104.6	0.82	129.7
1175	97.3	104.9	0.84	323.9
1176	97.3	105.0	0.94	129.6
1177	97.3	104.7	0.95	323.9
2178	97.3	104.6	1.05	129.6
2179	97.3	105.0	1.06	226.9
2180	97.3	104.4	1.06	324.1
1181	97.3	104.6	1.11	129.6
2182	97.3	104.3	1.10	226.8
2183	97.2	104.9	1.10	323.9
2184	97.2	104.8	1.17	129.6
2185	97.2	104.6	1.17	226.8
2186	97.2	104.9	1.17	324.1
1187	145.8	105.0	0.43	129.6
1188	145.8	104.7	0.43	324.0
1189	145.7	104.8	0.57	129.4
1190	145.7	104.9	0.58	324.0
1191	145.7	104.8	0.74	129.6
1192	145.7	104.9	0.75	323.9
2193	145.7	105.0	1.06	129.6
2194	145.7	104.6	1.07	226.8
2195	145.7	105.0	1.06	323.9
2196	145.7	105.1	1.11	129.6
1197	145.7	105.2	1.10	226.7
2198	145.7	104.8	1.11	324.1
2199	145.7	105.2	1.17	129.6
2200	145.7	104.9	1.17	226.8

(*continued on next page*)

Table A.1 (*continued*)

Experiment Reference Number (Expt.#)	G [kg/m^{2}s]	p_{in} [kPa]	$x_{e,in}$	G_w [kg/m^{2}s]
2201	145.7	104.9	1.17	324.1
1202	194.3	105.1	0.33	129.6
1203	194.3	104.8	0.35	324.1
1204	194.3	104.8	0.46	129.6
1205	194.3	103.9	0.48	324.6
1206	194.3	105.0	0.90	129.6
2207	194.3	104.8	0.91	324.1
2208	194.3	106.7	1.05	129.6
2209	194.3	105.8	1.06	226.7
2210	194.3	104.8	1.06	324.0
2211	194.3	108.0	1.10	129.6
3212	194.3	105.0	1.11	226.8
2213	194.3	104.8	1.12	324.1
2214	194.3	110.0	1.16	129.6
2215	194.3	104.8	1.18	226.8
2216	194.3	105.2	1.18	324.2
1217	242.9	105.5	0.28	129.6
1218	242.9	104.0	0.30	324.2
1219	242.9	105.0	0.65	129.6
1220	242.9	106.7	0.65	323.9
1221	242.9	107.4	0.83	129.4
1222	242.9	105.3	0.86	324.1
5223	242.9	116.5	1.05	129.6
2224	242.9	108.4	1.05	226.8
10225	242.9	104.7	1.04	324.1
3226	242.9	117.8	1.08	129.6
1227	242.9	109.2	1.09	226.8
1228	242.9	105.0	1.11	323.9
3229	242.9	120.3	1.14	129.6
2230	242.9	112.6	1.15	226.8
2231	242.9	107.3	1.17	324.2
1232	291.5	104.9	0.49	129.6
1233	291.5	106.2	0.50	323.9
1234	291.5	106.6	0.64	129.6
1235	291.5	105.2	0.67	323.9
1236	291.5	119.6	0.90	129.6
2237	291.5	117.6	0.94	324.0
10238	291.4	124.1	0.97	129.6
10239	291.5	114.8	1.01	226.8
10240	291.5	107.1	1.02	323.9

Appendix B. Comprehensive database results

In Section 3.1, the influence of G_w was examined, and a subset of the database displaying heat transfer independent of G_w was identified, $G \leq 150$ kg/m^{2}s with $G_w \geq 226$ kg/m^{2}s, and for $G > 150$ kg/m^{2}s only $G_w \geq 323$ kg/m^2. The subset independent of G_w, analyzed in Section 3, exhibited smooth monotonic q'' profiles and was used to assess various correlations and an analytical model for heat transfer coefficient in Section 4. The remaining subset showed degraded heat transfer at high x_e as G_w decreased, as observed in Fig. 11. This appendix presents results for the entire database, including both G_w independent and dependent data, for the reader's interest in comparing the subsets of the database. Discussion of experimental results will be brief and focus on unique observations attributed to lower G_w, as previously discussed trends are still valid.

Figs. B1–B4 present plots of h with respect to x_e along the channel for cases with $\Delta T_{sh,in} \approx 15°$C, $\Delta T_{sh,in} \approx 10°$C, $\Delta T_{sh,in} \approx 5°$C, and $\Delta T_{sh,in} \approx 0°$C, respectively. As discussed in Section 3, h is dependent on local conditions, and increasing $\Delta T_{sh,in}$ has a negligible effect on h. Figs. B1–B4 exhibit trends consistent with those discussed in Section 3, including h increasing with G, and p weakly affecting h.

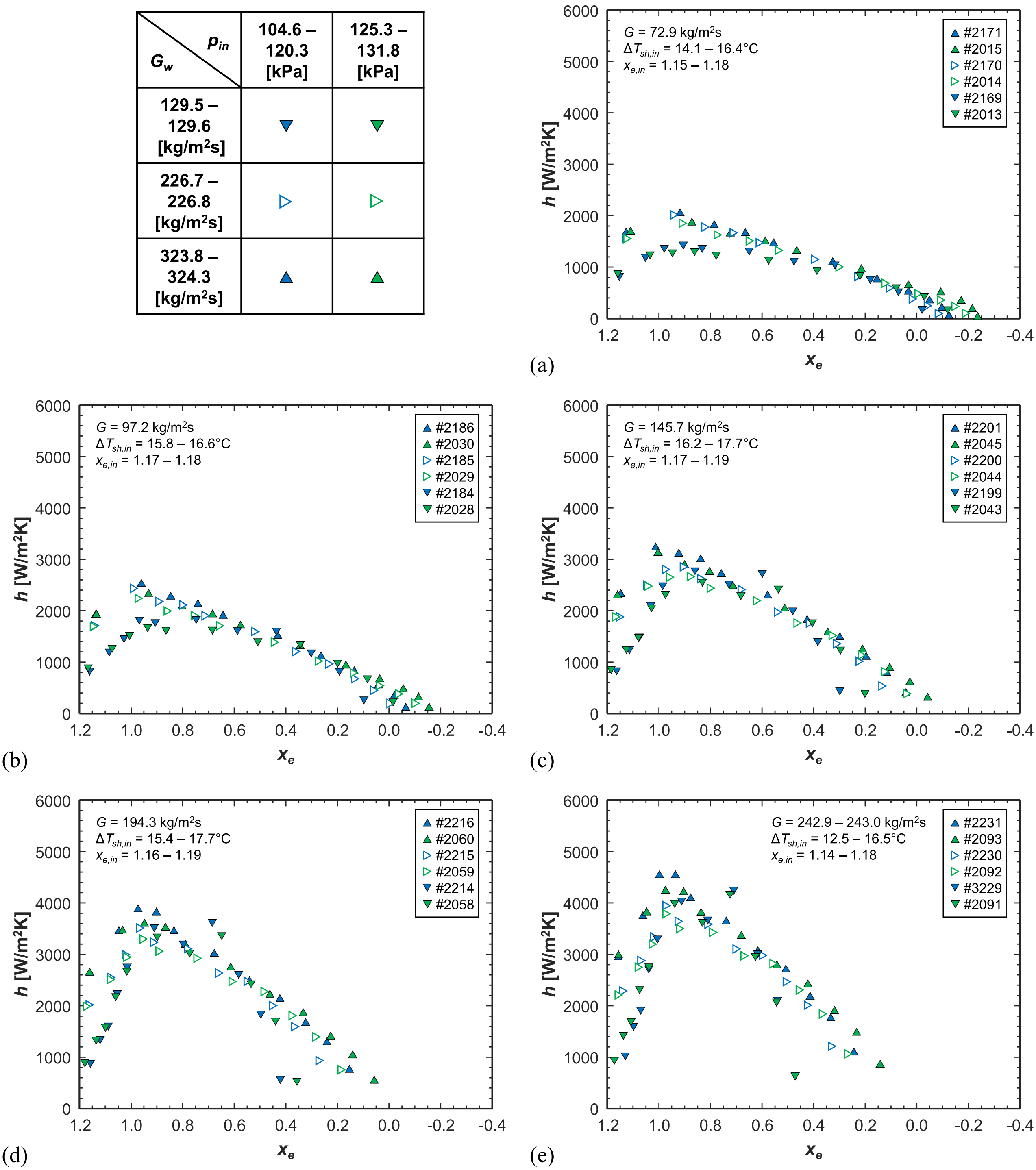

Fig. B1. Plots depicting variations in heat transfer coefficient, h, with respect to thermodynamic equilibrium quality, x_e, at different water mass velocities, G_w, and inlet pressures, p_{in}, for nPFH mass velocities of (a) $G \approx 73$ kg/m^{2}s, (b) $G \approx 97$ kg/m^{2}s, (c) $G \approx 146$ kg/m^{2}s, (d) $G \approx 194$ kg/m^{2}s, and (e) $G \approx 243$ kg/m^{2}s. Cases are shown for an inlet superheat of $\Delta T_{sh,in} \approx 15^{\circ}$C.

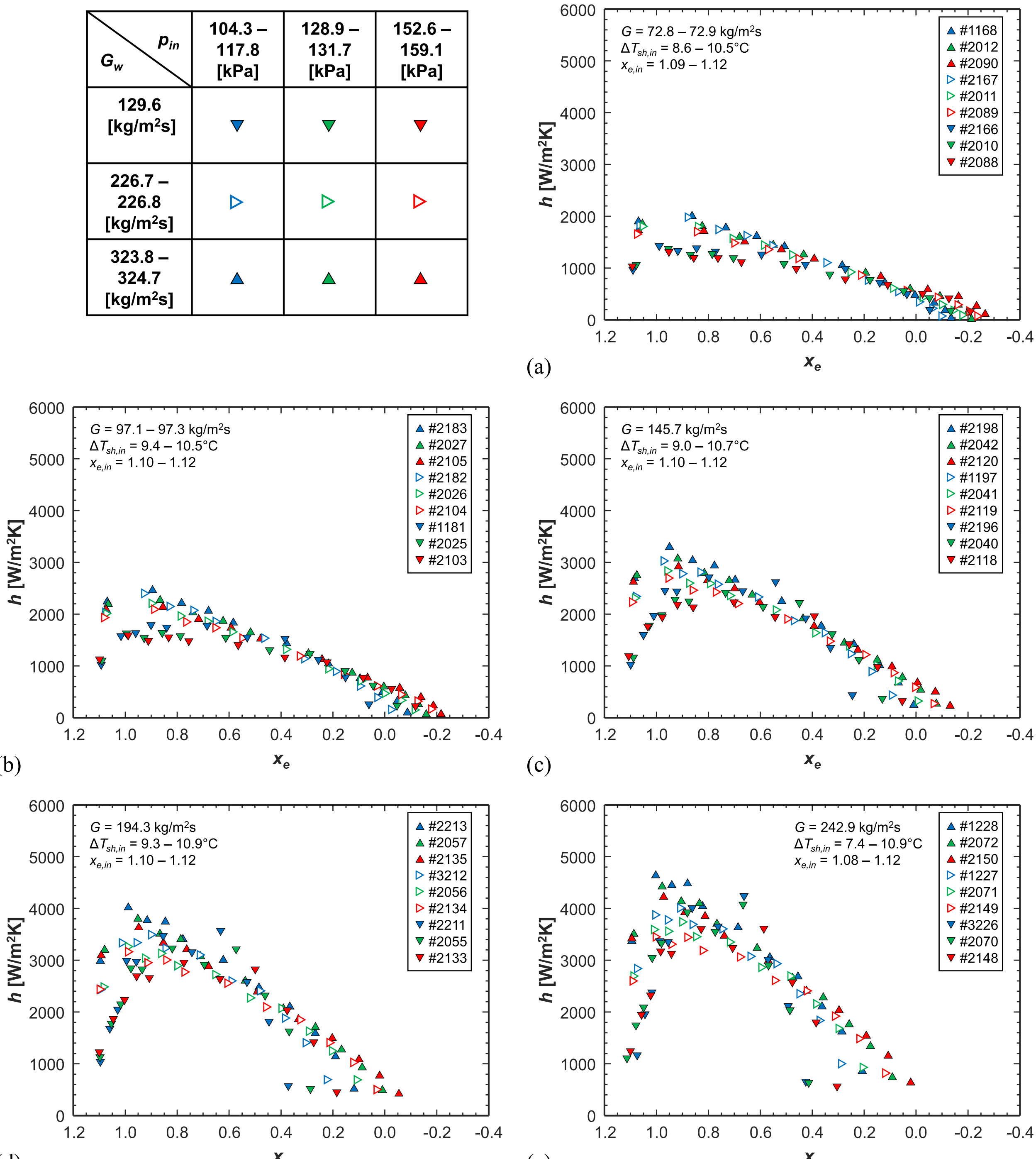

Fig. B2. Plots depicting variations in heat transfer coefficient, h, with respect to thermodynamic equilibrium quality, x_e, at different water mass velocities, G_w, and inlet pressures, p_{in}, for nPFH mass velocities of (a) $G \approx 73$ kg/m^{2}s, (b) $G \approx 97$ kg/m^{2}s, (c) $G \approx 146$ kg/m^{2}s, (d) $G \approx 194$ kg/m^{2}s, and (e) $G \approx 243$ kg/m^{2}s. Cases are shown for an inlet superheat of $\Delta T_{sh,in} \approx 10^{\circ}$C.

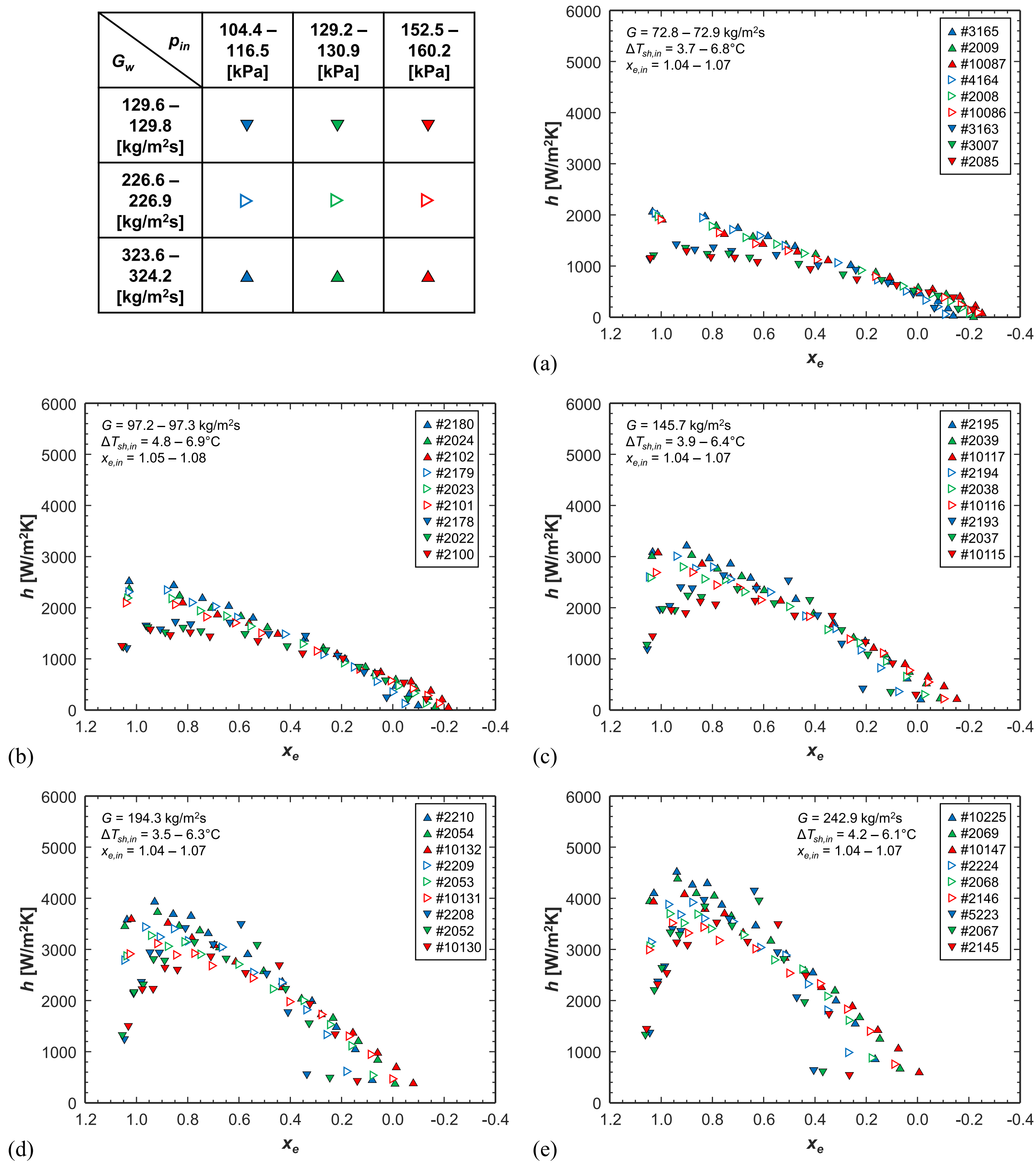

Fig. B3. Plots depicting variations in heat transfer coefficient, h, with respect to thermodynamic equilibrium quality, x_e, at different water mass velocities, G_w, and inlet pressures, p_{in}, for nPFH mass velocities of (a) $G \approx 73$ kg/m^{2}s, (b) $G \approx 97$ kg/m^{2}s, (c) $G \approx 146$ kg/m^{2}s, (d) $G \approx 194$ kg/m^{2}s, and (e) $G \approx 243$ kg/m^{2}s. Cases are shown for an inlet superheat of $\Delta T_{sh,in} \approx 5°$C.

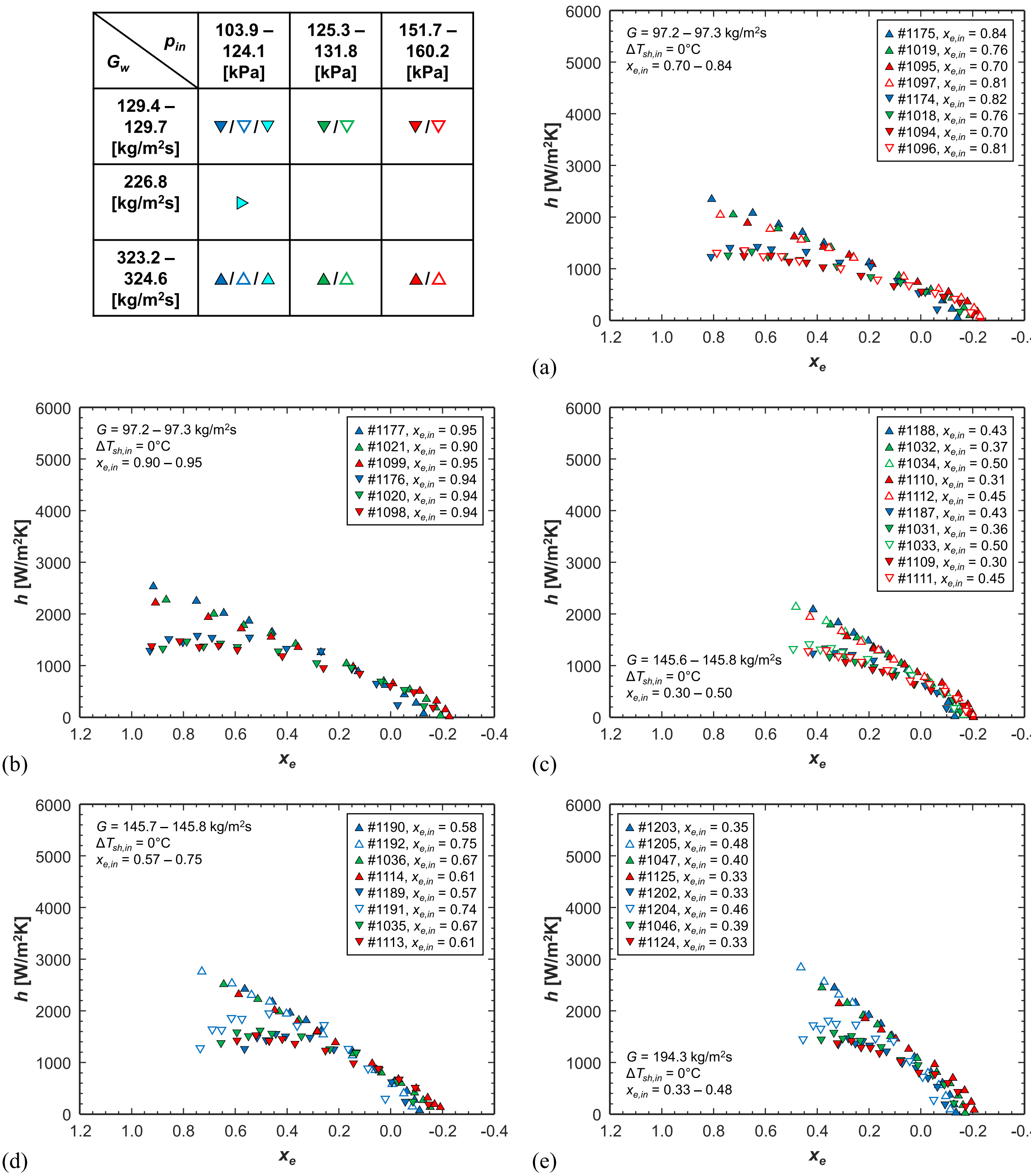

Fig. B4. Plots depicting variations of heat transfer coefficient, h, with respect to thermodynamic equilibrium quality, x_e, at different water mass velocities, G_w, inlet pressures, p_{in}, and an inlet superheat of $\Delta T_{sh,in} \approx 0^\circ$C. Plots are shown for nPFH mass velocity of $G \approx 97$ kg/m^{2}s with inlet thermodynamic equilibrium quality of (a) $x_{e,in} \approx 0.77$ and (b) $x_{e,in} \approx 0.92$, $G \approx 146$ kg/m^{2}s with (c) $x_{e,in}$, ≈ 0.40 and (d) $x_{e,in}$, ≈ 0.66, $G \approx 194$ kg/m^{2}s with (e) $x_{e,in}$, ≈ 0.40 and (f) $x_{e,in}$, ≈ 083, $G \approx 243$ kg/m^{2}s with (g) $x_{e,in}$, ≈ 0.48 and (h) $x_{e,in}$, ≈ 0.79, and $G \approx 292$ kg/m^{2}s with (i) $x_{e,in}$, ≈ 0.50 and (j) $x_{e,in}$, ≈ 0.88.

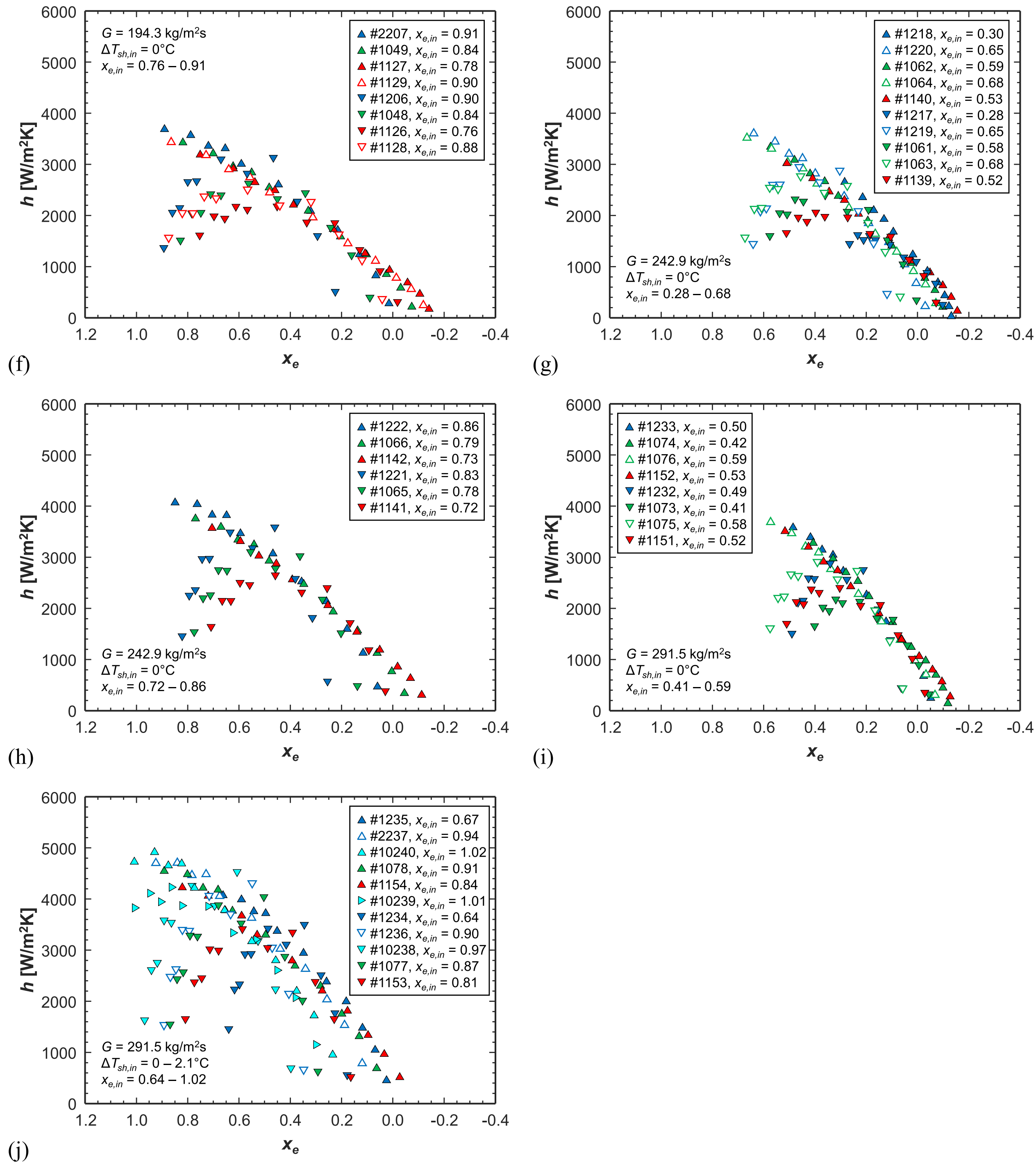

Fig. B4. (*continued*).

For $G \leq 150$ kg/m^{2}s, h is relatively constant at $G_w \approx 227$ kg/m^{2}s and $G_w \approx 324$ kg/m^{2}s, but significantly degraded at high x_e for $G_w \approx 130$ kg/m^{2}s. As x_e decreases, h converges for all G_w. For $G > 150$, h increases with G_w at high x_e, but the differences become less pronounced at $x_e \approx 0.4 – 0.8$. This is caused by h reaching a maximum at $x_e \approx 0.6$ for $G_w \approx 130$ kg/m^{2}s, even surpassing h for $G_w \approx 227$ kg/m^{2}s and $G_w \approx 324$ kg/m^{2}s, unlike at higher G_w where maximum h occurs at $x_e \approx 1.0$. At $G_w \approx 130$ kg/m^{2}s, h rapidly declines with x_e after its maximum, resulting in reduced h at low x_e compared to higher G_w. The deviations between $G_w \approx 227$ kg/m^{2}s and $G_w \approx 324$ kg/m^{2}s are significant in the upstream at high x_e, but less pronounced downstream at low x_e.

Fig. B5 presents plots of $\overline{h}_{tp}$ and $\overline{h}$ with respect to $x_{e,in}$ at different G_w. Interestingly, the deviations of h between different G_w observed in Figs. B1–B4 do not significantly impact $\overline{h}_{tp}$ or $\overline{h}$, and similar trends are observed in Fig. B5 to those in Fig. 17. Increasing $\Delta T_{sh,in}$ does not influence $\overline{h}_{tp}$, but does slightly enhance $\overline{h}$ at all G_w. Otherwise, both $\overline{h}_{tp}$ and $\overline{h}$ increase with $x_{e,in}$, due to the greater h observed at high x_e within the channel, but $\overline{h}_{tp}$ is not enhance increasing $x_{e,in}$ above 1.

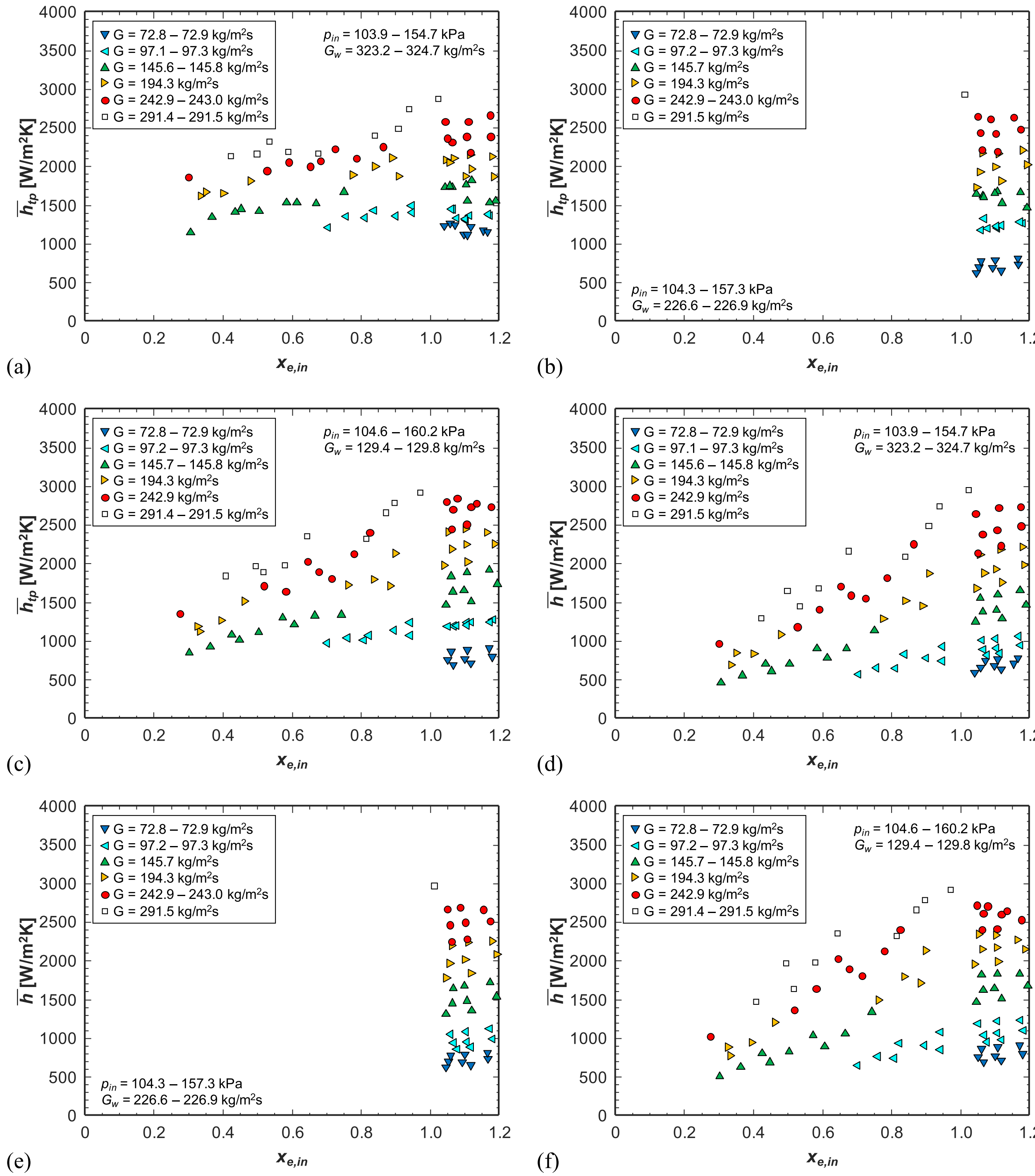

Fig. B5. Plots depicting variations of average heat transfer coefficient over the saturated two-phase length, $\overline{h}_{tp}$, with water mass velocity of (a) $G_w \approx 324$ kg/m^{2}s, (b) $G_w \approx 227$ kg/m^{2}s, and (c) $G_w \approx 130$ kg/m^{2}s, and average heat transfer coefficient over the entire channel, $\overline{h}$, with water mass velocity of (d) $G_w \approx 324$ kg/m^{2}s, (e) $G_w \approx 227$ kg/m^{2}s, and (f) $G_w \approx 130$ kg/m^{2}s with respect to inlet thermodynamic equilibrium quality, $x_{e,in}$.

The minimal influence of G_w on $\overline{h}_{tp}$ and $\overline{h}$ is attributed to the location of the maximum h. At $G_w \approx 324$ kg/m^{2}s and $G_w \approx 227$ kg/m^{2}s, the maximum h occurred at $x_e \approx 1.0$ in the upstream portion of the channel where the spacing between thermocouples is relatively small. At $G_w \approx 130$ kg/m^{2}s, the maximum h occurred further downstream, near $x_e \approx 0.6$, where the thermocouples are spaced farther apart, This results in greater weight given to the maximum h when spatially averaging h as shown in Eq. (8), compensating for the degraded h in the upstream region at low G_w and yielding similar $\overline{h}_{tp}$ and $\overline{h}$ to those observed at higher G_w.

Data availability

Future access to the data will require approval from NASA.

References

[1] Y. Chen, C.B. Sobhan, G.P. Peterson, Review of condensation heat transfer in microgravity environments, J. Thermophys. Heat Transf. 20 (2006) 353–360.
[2] National Academies of Sciences, Engineering, and Medicine, Thriving in Space: Ensuring the Future of Biological and Physical Sciences Research: A Decadal Survey for 2023-2032, National Academies Press, Washington, D.C., USA, 2023, p. 2023, https://doi.org/10.17226/26750.
[3] S.J. Darges, V.S. Devahdhanush, I. Mudawar, Assessment and development of flow boiling critical heat flux correlations for partially heated rectangular channels in different gravitational environments, Int. J. Heat Mass Transf. 196 (2022) 123291, https://doi.org/10.1016/j.ijheatmasstransfer.2022.123291.
[4] T.J. LaClair, I. Mudawar, Thermal transients in a capillary evaporator prior to the initiation of boiling, Int. J. Heat Mass Transf. 43 (21) (2000) 3937–3952, https://doi.org/10.1016/S0017-9310(00)00042-9.
[5] G. Liang, I. Mudawar, Pool boiling critical heat flux (CHF)–Part 2: assessment of models and correlations, Int. J. Heat Mass Transf. 117 (2018) 1368–1383, https://doi.org/10.1016/j.ijheatmasstransfer.2017.09.073.
[6] I. Mudawar, R.A. Houpt, Mass and momentum transport in smooth falling liquid films laminarized at relatively high Reynolds numbers, Int. J. Heat Mass Transf. 36 (14) (1993) 3437–3448, https://doi.org/10.1016/0017-9310(93)90162-Y.
[7] W.P. Klinzing, J.C. Rozzi, I. Mudawar, Film and transition boiling correlations for quenching of hot surfaces with water sprays, J. Heat Treat. 9 (2) (1992) 91–103, https://doi.org/10.1007/BF02833145.
[8] M.E. Johns, I. Mudawar, An ultra-high power two-phase jet-impingement avionic clamshell module, J. Electron. Packag. 118 (4) (1996) 264–270, https://doi.org/10.1115/1.2792162.
[9] I. Mudawar, D.E. Maddox, Enhancement of critical heat flux from high power microelectronic heat sources in a flow channel, J. Electron. Packag. 112 (3) (1990) 241–248, https://doi.org/10.1115/1.2904373.
[10] C.O. Gersey, I. Mudawar, Effects of heater length and orientation on the trigger mechanism for near-saturated flow boiling critical heat flux—II. Critical heat flux model, Int. J. Heat Mass Transf. 38 (4) (1995) 643–654, https://doi.org/10.1016/0017-9310(94)00194-Z.
[11] S. Mukherjee, I. Mudawar, Pumpless loop for narrow channel and micro-channel boiling, J. Electron. Packag. 125 (3) (2003) 431–441, https://doi.org/10.1115/1.1602708.
[12] M.K. Sung, I. Mudawar, Single-phase and two-phase heat transfer characteristics of low temperature hybrid micro-channel/micro-jet impingement cooling module, Int. J. Heat Mass Transf. 51 (15–16) (2008) 3882–3895, https://doi.org/10.1016/j.ijheatmasstransfer.2007.12.016.
[13] M.K. Sung, I. Mudawar, Single-phase and two-phase hybrid cooling schemes for high-heat-flux thermal management of defense electronics, J. Electron. Packag. 131 (2) (2009) 021013, https://doi.org/10.1115/1.3111253.
[14] F.P. Chiaramonte, J. McQuillen, H.K. Nahra, P. Manoharan, H. Vanhala, B.J. Motil, J. Kim, V. Carey, W.G. Anderson, J. Plawsky, L. Carter, A. Jackson, 2019 NASA division of space and life and phyiscal sciences research and applications fluid physics workshop report, Cleveland, OH, USA, 2020.
[15] C. Konishi, I. Mudawar, Review of flow boiling and critical heat flux in microgravity, Int. J. Heat Mass Transf. 80 (2015) 469–493, https://doi.org/10.1016/j.ijheatmasstransfer.2014.09.017.
[16] T.R. Reinarts, F.R. Best, W.S. Hill, Definition of condensation two phase flow behaviors for spacecraft design, in: Proceedings of the AIP Conference, AIP, 1992, pp. 1216–1225, https://doi.org/10.1063/1.41741.
[17] H. Lee, I. Mudawar, M.M. Hasan, Experimental and theoretical investigation of annular flow condensation in microgravity, Int. J. Heat Mass Transf. 61 (2013) 293–309, https://doi.org/10.1016/j.ijheatmasstransfer.2013.02.010.
[18] M. Azzolin, S. Bortolin, L.P. Le Nguyen, P. Lavieille, A. Glushchuk, P. Queeckers, M. Miscevic, C.S. Iorio, D. Del Col, Experimental investigation of in-tube condensation in microgravity, Int. Commun. Heat Mass Transf. 96 (2018) 69–79, https://doi.org/10.1016/j.icheatmasstransfer.2018.05.013.
[19] A. Berto, M. Azzolin, P. Lavieille, A. Glushchuk, P. Queeckers, S. Bortolin, C. S. Iorio, M. Miscevic, D. Del Col, Experimental investigation of liquid film thickness and heat transfer during condensation in microgravity, Int. J. Heat Mass Transf. 199 (2022) 123467, https://doi.org/10.1016/j.ijheatmasstransfer.2022.123467.
[20] A. Glushchuk, C. Minetti, C. Buffone, Fin condensation in variable gravity environment, Multiph. Sci. Technol. 26 (1) (2014) 63–81, https://doi.org/10.1615/MultScienTechn.v26.i1.20.
[21] A. Glushchuk, C. Minetti, H. Machrafi, C.S. Iorio, Experimental investigation of force balance at vapour condensation on a cylindrical fin, Int. J. Heat Mass Transf. 108 (2017) 2130–2142, https://doi.org/10.1016/j.ijheatmasstransfer.2017.01.067.
[22] M. Azzolin, S. Bortolin, D. Del Col, Convective condensation at low mass flux: effect of turbulence and tube orientation on the heat transfer, Int. J. Heat Mass Transf. 144 (2019) 118646, https://doi.org/10.1016/j.ijheatmasstransfer.2019.118646.
[23] S.G. Mohseni, M.A. Akhavan-Behabadi, M. Saeedinia, Flow pattern visualization and heat transfer characteristics of R-134a during condensation inside a smooth tube with different tube inclinations, Int. J. Heat Mass Transf. 60 (2013) 598–602, https://doi.org/10.1016/j.ijheatmasstransfer.2013.01.023.
[24] L.E. O'Neill, R. Balasubramaniam, H.K. Nahra, M.M. Hasan, I. Mudawar, Flow condensation heat transfer in a smooth tube at different orientations: experimental results and predictive models, Int. J. Heat Mass Transf. 140 (2019) 533–563, https://doi.org/10.1016/j.ijheatmasstransfer.2019.05.103.
[25] D. Del Col, M. Bortolato, M. Azzolin, S. Bortolin, Effect of inclination during condensation inside a square cross section minichannel, Int. J. Heat Mass Transf. 78 (2014) 760–777, https://doi.org/10.1016/j.ijheatmasstransfer.2014.06.078.
[26] D.R.E. Ewim, J.P. Meyer, S.M.A. Noori, R. Abadi, Condensation heat transfer coefficients in an inclined smooth tube at low mass fluxes, Int. J. Heat Mass Transf. 123 (2018) 455–467, https://doi.org/10.1016/j.ijheatmasstransfer.2018.02.091.
[27] S.P. Olivier, J.P. Meyer, M. De Paepe, K. De Kerpel, The influence of inclination angle on void fraction and heat transfer during condensation inside a smooth tube, Int. J. Multiph. Flow 80 (2016) 1–14, https://doi.org/10.1016/j.ijmultiphaseflow.2015.10.015.
[28] L.E. O'Neill, I. Park, C.R. Kharangate, V.S. Devahdhanush, V. Ganesan, I. Mudawar, Assessment of body force effects in flow condensation, part II: criteria for negating influence of gravity, Int. J. Heat Mass Transf. 106 (2017) 313–328, https://doi.org/10.1016/j.ijheatmasstransfer.2016.07.019.
[29] Y. Qiu, H. Lee, C.R. Kharangate, Computational investigation of annular flow condensation in microgravity with two-phase inlet conditions, Int. Commun. Heat Mass Transf. 118 (2020) 104877, https://doi.org/10.1016/j.icheatmasstransfer.2020.104877.
[30] E.Da Riva, D. Del Col, Effect of gravity during condensation of R134a in a circular minichannel, Microgravity Sci. Technol. 23 (S1) (2011) 87–97, https://doi.org/10.1007/s12217-011-9275-4.
[31] W. Li, J. Zhang, P. Mi, J. Zhao, Z. Tao, P.R.N. Childs, T.I.P. Shih, The effect of gravity on R410A condensing flow in horizontal circular tubes, Numer. Heat Transf. Part A Appl. 71 (3) (2017) 327–340, https://doi.org/10.1080/10407782.2016.1264743.
[32] A. Berto, M. Azzolin, S. Bortolin, M. Miscevic, P. Lavieille, D. Del Col, Condensation heat transfer in microgravity conditions, npj Microgravity 9 (1) (2023) 32, https://doi.org/10.1038/s41526-023-00276-1.
[33] I. Mudawar, V.S. Devahdhanush, S.J. Darges, M.M. Hasan, H.K. Nahra, R. Balasubramaniam, J.R. Mackey, Heat transfer and interfacial flow physics of microgravity flow boiling in single-side-heated rectangular channel with subcooled inlet conditions–experiments onboard the International Space Station, Int. J. Heat Mass Transf. 207 (2023) 123998, https://doi.org/10.1016/j.ijheatmasstransfer.2023.123998.
[34] I. Mudawar, V.S. Devahdhanush, S.J. Darges, M.M. Hasan, H.K. Nahra, R. Balasubramaniam, J.R. Mackey, Effects of heating configuration and operating parameters on heat transfer and interfacial physics of microgravity flow boiling with subcooled inlet conditions–experiments onboard the International Space Station, Int. J. Heat Mass Transf. 217 (2023) 124732, https://doi.org/10.1016/j.ijheatmasstransfer.2023.124732.
[35] I. Mudawar, V.S. Devahdhanush, S.J. Darges, M.M. Hasan, H.K. Nahra, R. Balasubramaniam, J.R. Mackey, Microgravity flow boiling experiments with liquid-vapor mixture inlet onboard the International Space Station, Int. J. Heat Mass Transf. 224 (2024) 125299, https://doi.org/10.1016/j.ijheatmasstransfer.2024.125299.
[36] I. Mudawar, S.J. Darges, V.S. Devahdhanush, Parametric experimental trends, interfacial behavior, correlation assessment, and interfacial lift-off model predictions of critical heat flux for microgravity flow boiling with subcooled inlet conditions–experiments onboard the International Space Stat, Int. J. Heat Mass Transf. 213 (2023) 124296, https://doi.org/10.1016/j.ijheatmasstransfer.2023.124296.
[37] I. Mudawar, S.J. Darges, V.S. Devahdhanush, Critical heat flux for flow boiling with saturated two-phase inlet in microgravity onboard the International Space Station, Int. J. Heat Mass Transf. 233 (2024) 126017, https://doi.org/10.1016/j.ijheatmasstransfer.2024.126017.
[38] I. Mudawar, S.J. Darges, V.S. Devahdhanush, M.M. Hasan, H.K. Nahra, R. Balasubramaniam, J.R. Mackey, Two-phase flow instabilities during microgravity flow boiling onboard the International Space Station, Int. J. Heat Mass Transf. 234 (2024) 126102, https://doi.org/10.1016/j.ijheatmasstransfer.2024.126102.
[39] I. Mudawar, S.J. Darges, V.S. Devahdhanush, Prediction technique for flow boiling heat transfer and critical heat flux in both microgravity and Earth gravity via artificial neural networks (ANNs), Int. J. Heat Mass Transf. 220 (2024) 124998, https://doi.org/10.1016/j.ijheatmasstransfer.2023.124998.
[40] I. Mudawar, S.J. Darges, V.S. Devahdhanush, M.M. Hasan, H.K. Nahra, R. Balasubramaniam, J.R. Mackey, Pressure drop characteristics and prediction techniques (models/correlations and artificial neural networks) for microgravity flow boiling onboard the International Space Station, Int. J. Heat Mass Transf. 240 (2025) 126593, https://doi.org/10.1016/j.ijheatmasstransfer.2024.126593.
[41] W.A. Arnold, T.G. Hartman, J. McQuillen, Chemical characterization and thermal stressing studies of perfluorohexane fluids for space-based applications, J. Spacecr. Rockets 44 (1) (2007) 94–102, https://doi.org/10.2514/1.22537.
[42] J. Lee, V.S. Devahdhanush, S.J. Darges, I. Mudawar, Effects of flow loop compressible volume position on system instabilities during flow boiling in micro-channel heat sinks, Int. J. Heat Mass Transf. 198 (2022) 123394, https://doi.org/10.1016/j.ijheatmasstransfer.2022.123394.
[43] E.W. Lemmon, I.H. Bell, M.L. Huber, M.O. McLinden, NIST Standard Reference Database 23: Reference Fluid Thermodynamic and Transport Properties-REFPROP, Version 10, NIST, Gaithersburg, MD, USA, 2018.
[44] L.E. O'Neill, R. Balasubramaniam, H.K. Nahra, M.M. Hasan, J.R. Mackey, I. Mudawar, Identification of condensation flow regime at different orientations

using temperature and pressure measurements, Int. J. Heat Mass Transf. 135 (2019) 569–590, https://doi.org/10.1016/j.ijheatmasstransfer.2019.01.133.
[45] W.H. McAdams, W.K. Woods, L.C. Heroman, Vaporization inside horizontal tubes–II benzene-oil mixtures, Trans. ASME 64 (3) (1942) 193–200. https://asmedigitalcollection.asme.org/fluidsengineering/article/64/3/193/1155080/Vaporization-Inside-Horizontal-Tubes-II-Benzene.
[46] S.M. Kim, I. Mudawar, Universal approach to predicting heat transfer coefficient for condensing mini/micro-channel flow, Int. J. Heat Mass Transf. 56 (1–2) (2013) 238–250, https://doi.org/10.1016/j.ijheatmasstransfer.2012.09.032.
[47] C.A. Dorao, M. Fernandino, Simple and general correlation for heat transfer during flow condensation inside plain pipes, Int. J. Heat Mass Transf. 122 (2018) 290–305, https://doi.org/10.1016/j.ijheatmasstransfer.2018.01.097.
[48] S.H. Hosseini, M.A. Moradkhani, M. Valizadeh, A. Zendehboudi, M. Olazar, A general heat transfer correlation for flow condensation in single port mini and macro channels using genetic programming, Int. J. Refrig. 119 (2020) 376–389, https://doi.org/10.1016/j.ijrefrig.2020.06.021.
[49] M.M. Shah, Improved general correlation for condensation in channels, Inventions 7 (4) (2022) 114, https://doi.org/10.3390/inventions7040114.
[50] M.M. Shah, Improved correlation for heat transfer during condensation in mini and macro channels, Int. J. Heat Mass Transf. 194 (2022) 123069, https://doi.org/10.1016/j.ijheatmasstransfer.2022.123069.
[51] F. Nie, H. Wang, Y. Zhao, Q. Song, S. Yan, M. Gong, A universal correlation for flow condensation heat transfer in horizontal tubes based on machine learning, Int. J. Therm. Sci. 184 (2023) 107994, https://doi.org/10.1016/j.ijthermalsci.2022.107994.
[52] M.A. Moradkhani, S.H. Hosseini, M. Song, Robust and general predictive models for condensation heat transfer inside conventional and mini/micro channel heat exchangers, Appl. Therm. Eng. 201 (2022) 117737, https://doi.org/10.1016/j.applthermaleng.2021.117737.
[53] M. Mani Marinheiro, D. Borba Marchetto, G. Furlan, A. Theodoro de Souza Netto, C. Bigonha Tibiriçá, A robust and simple correlation for internal flow condensation, Appl. Therm. Eng. 236 (2024) 121811, https://doi.org/10.1016/j.applthermaleng.2023.121811.
[54] S.M. Kim, I. Mudawar, Theoretical model for annular flow condensation in rectangular micro-channels, Int. J. Heat Mass Transf. 55 (4) (2012) 958–970, https://doi.org/10.1016/j.ijheatmasstransfer.2011.10.014.
[55] I. Mudawar, M.A. El-Masri, Momentum and heat transfer across freely-falling turbulent liquid films, Int. J. Multiph. Flow 12 (5) (1986) 771–790, https://doi.org/10.1016/0301-9322(86)90051-0.
[56] R.K. Shah, A.L. London, Rectangular ducts. Laminar Flow Forced Convection in Ducts, Elsevier, 1978, pp. 196–222, https://doi.org/10.1016/B978-0-12-020051-1.50012-7.
[57] G.B. Wallis, One-Dimensional Two-Phase Flow, Dover Publications Inc., Garden City, New York, USA, 2020.